

AD-A173 187

PLASTIC STRAIN LOCALIZATION IN SUPERALLOY SINGLE
CRYSTALS(U) UNITED TECHNOLOGIES RESEARCH CENTER EAST
HARTFORD CT D L ANTON ET AL. 31 JUL 86

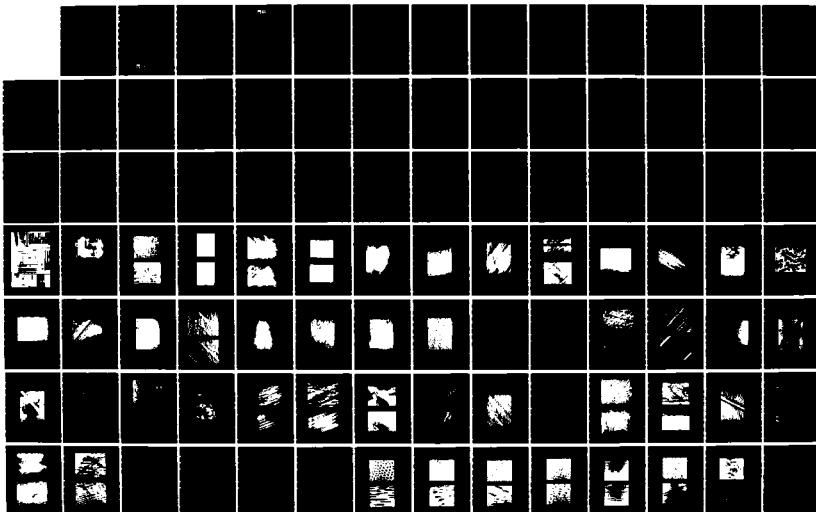
1/2

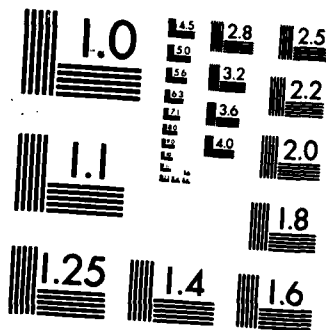
UNCLASSIFIED

UTRC/R86-916534-3 AFOSR-TR-86-8821

F/G 20/11

NL





MICROCOPY RESOLUTION TEST CHART
NATIONAL BUREAU OF STANDARDS-1963-A

2

AD-A173 187

PLASTIC STRAIN LOCALIZATION IN SUPERALLOY SINGLE CRYSTALS

Prepared by
D.L. Anton
A.F. Giamei

FINAL REPORT

Contract F49620-83-C-0104

for

Air Force Office of Scientific Research
Building 410
Bolling Air Force Base
Washington, DC 20332

JULY 31, 1986

AIR FORCE OFFICE OF SCIENTIFIC RESEARCH (AFOSR)
NOTICE TO RESEARCHERS AND TO DTIC
This report is the property of the Air Force Office of Scientific Research and its
approval does not constitute an endorsement or approval of the views or
statements contained herein. Distribution is unlimited.
MARTIN W. J. WILSON
Chief, Technical Information Division

"The views and conclusions contained in this document are those of the authors and should not be interpreted as necessarily representing the official policies or endorsements, either expressed or implied, of the Air Force Office of Scientific Research or the U.S. Government."

DTIC FILE COPY



**UNITED
TECHNOLOGIES
RESEARCH
CENTER**

East Hartford, Connecticut 06108

DTIC
ELECTE
OCT 20 1986

B

REPORT DOCUMENTATION PAGE

| | | | | | | |
|---|-------|--|---|---|--------------------------------|-------------------------|
| 1a. REPORT SECURITY CLASSIFICATION Unclassified | | | 1b. RESTRICTIVE MARKINGS | | | |
| 2a. SECURITY CLASSIFICATION AUTHORITY | | | 3. DISTRIBUTION / AVAILABILITY OF REPORT Unlimited | | | |
| 2b. DECLASSIFICATION / DOWNGRADING SCHEDULE | | | 5. MONITORING ORGANIZATION REPORT NUMBER(S) AFOSR-TR-86-0821 | | | |
| 4. PERFORMING ORGANIZATION REPORT NUMBER(S) R86-916534-3 | | | 5. MONITORING ORGANIZATION REPORT NUMBER(S) | | | |
| 6a. NAME OF PERFORMING ORGANIZATION United Technologies Research Center | | 6b. OFFICE SYMBOL (if applicable) | | 7a. NAME OF MONITORING ORGANIZATION See 8a | | |
| 6c. ADDRESS (City, State, and ZIP Code) Silver Lane East Hartford, CT 06108 | | | 7b. ADDRESS (City, State, and ZIP Code) See 8c | | | |
| 8a. NAME OF FUNDING / SPONSORING ORGANIZATION Air Force Office of Scientific Research | | 8b. OFFICE SYMBOL (if applicable) | | 9. PROCUREMENT INSTRUMENT IDENTIFICATION NUMBER F49620-83-C-0104 | | |
| 8c. ADDRESS (City, State, and ZIP Code) Bolling Air Force Base Washington, DC 20332 | | | 10. SOURCE OF FUNDING NUMBERS | | | |
| | | | PROGRAM ELEMENT NO. 61102F | PROJECT NO. 2306 | TASK NO. A1 | WORK UNIT ACCESSION NO. |
| 11. TITLE (Include Security Classification) PLASTIC STRAIN LOCALIZATION IN SUPERALLOY SINGLE CRYSTALS | | | | | | |
| 12. PERSONAL AUTHOR(S) D. L. Anton and A. F. Giamei | | | | | | |
| 13a. TYPE OF REPORT Final | | 13b. TIME COVERED FROM 5/83 TO 6/86 | | 14. DATE OF REPORT (Year, Month, Day) 1986 July 31 | | 15. PAGE COUNT 96 |
| 16. SUPPLEMENTARY NOTATION | | | | | | |
| 17. COSATI CODES | | | 18. SUBJECT TERMS (Continue on reverse if necessary and identify by block number) | | | |
| FIELD | GROUP | SUB-GROUP | | | | |
| 11.06 | | | | | | |
| 19. ABSTRACT (Continue on reverse if necessary and identify by block number) Nickel-base superalloys are notorious for their inhomogeneous deformation and poor fatigue behavior. Previous studies of surface slip behavior in superalloys were mostly carried out at low magnification and concluded that the slip was "planar" or, equivalently, "coarse", independent of alloy composition. In this research, single crystal nickel alloys of various gamma prime volume fraction and misfit were deformed under either monotonic or cyclic loading conditions and examined for slip distribution at very high magnification. The conclusion of this research was that the degree of slip localization in superalloys is decreased moderately by misfit and significantly by larger volume fractions of the strengthening gamma prime phase. This difference in behavior is reflected in the location of initiation sites. The alloys with more localized slip showed surface initiation, while those with more nearly homogeneous deformation indicated internal sites such as pores for initiation. Attempts to understand the origin of such pores by changes in solidification or heat treatment parameters led to the conclusions that it was possible to influence pore size or the volume fraction porosity, but that some pores were always present. As a result, no enhancement of fatigue life was obtained, consistent with theory. | | | | | | |
| 20. DISTRIBUTION / AVAILABILITY OF ABSTRACT <input checked="" type="checkbox"/> UNCLASSIFIED/UNLIMITED <input type="checkbox"/> SAME AS RPT. <input type="checkbox"/> DTIC USERS | | | | 21. ABSTRACT SECURITY CLASSIFICATION Unclassified | | |
| 22a. NAME OF RESPONSIBLE INDIVIDUAL Dr. A. Rosenstein | | | 22b. TELEPHONE (Include Area Code) | | 22c. OFFICE SYMBOL AFOSR/NE | |



**UNITED
TECHNOLOGIES
RESEARCH
CENTER**

East Hartford, Connecticut 06108

R86-916534-3

Plastic Strain Localization in
Superalloy Single Crystals

Final Report
F49620-83-C-0104

DTIC
ELECTE
S **D**
OCT 20 1986
B

REPORTED BY

D. L. Anton
D. L. Anton

A. F. Giamei
A. F. Giamei

APPROVED BY

M. A. DeCrescente
M. A. DeCrescente
Manager of Mfg. Tech.
and Process Research

DATE July 31, 1986

NO. OF PAGES _____

COPY NO. _____

ABSTRACT

It is well known that Ni-base superalloys deform in an inhomogeneous manner at both room and elevated temperatures. Local plastic deformation stems from the microscopic shearing of the γ' precipitates, the predominant strengthening phase, and leads to channels of relatively "soft" material. This localized "soft" material is caused by the decreased order in the γ' precipitates. Nonuniform deformation can also be caused by ceramic inclusions, large carbides, eutectic phases or porosity (all of which are commonly found in complex chemistry superalloys). This phenomenon of localized softening is not restricted to Ni-base superalloys, but occurs in most planar slip alloys containing coherent precipitates. In Ni-base superalloys, localized softening accounts for their renowned low fatigue endurance limit to yield strength ratio. Low to intermediate temperature failures generally result from this type of deformation.

Two separate experimental plans were executed to study the localization of plastic strain in superalloy single crystals. Slip bands as they manifest themselves through surface slip traces were examined in three different alloys having various γ' volume fractions and γ/γ' misfits with reference made to similar studies carried out on other alloys. Tests were conducted under both cyclic and monotonic loading conditions with observations periodically made by surface replication. The study of porosity, how pores can be modified through crystal growth variations and the degree to which high cycle fatigue lives can be modified through pore size and distribution control was performed.

The conclusions of this research are that the degree of slip localization in planes and bands is a first order function of γ' volume fraction and is influenced to a much lesser extent by γ/γ' misfit (as had been previously reported in the literature). In low volume fraction alloys, slip was shown to be highly localized on slip lines which rapidly grew into large slip offsets. Conversely, very broad slip bands resulted from both cyclic and monotonic loading of high volume fraction alloys. These changes in slip nature were correlated to fatigue crack initiation sites. High volume γ' fraction alloys typically fail at internal porosity while low volume fraction alloys initiate cracks from surface slip offsets.

Crystal growth rate variations were shown to have a large influence on the volume fraction of microporosity present, but only a limited effect on pore size. High cycle fatigue results revealed that no enhancement of fatigue lives could be gained through reduction of pore volume fraction or pore size. In no case could porosity be completely eliminated and since the stress concentration in the vicinity of an embedded spherical pore is independent of its radius, cracks initiated in failed test specimens at approximately the same cycle lives.



| | |
|---|-------------------------|
| <input type="checkbox"/> Unavailable <input type="checkbox"/> Just in time | |
| By _____ | |
| Distribution _____ | |
| Availability Codes | |
| Dist | Availability Special |
| A-1 | |

Plastic Strain Localization in Superalloy Single Crystals

TABLE OF CONTENTS

| | | |
|------|---|----|
| I. | INTRODUCTION | 1 |
| II. | INTERPRETATION OF SURFACE SLIP | 2 |
| III. | SURFACE SLIP MEASUREMENTS | 4 |
| A. | Experimental Procedures | 4 |
| 1. | Single Crystal Growth and Preparation | 4 |
| 2. | Compression Testing | 4 |
| 3. | Fatigue Testing | 5 |
| B. | Results | 5 |
| 1. | Compression Testing of Alloy 143 | 5 |
| a. | Undeformed | 5 |
| b. | SOL <011> Stress Axis | 5 |
| c. | SHT <011> Stress Axis | 7 |
| d. | SOL <001> Stress Axis | 7 |
| e. | SHT <001> Stress Axis | 7 |
| 2. | Compression Testing of U-700 | 8 |
| 3. | Compression Testing of 143L | 10 |
| 4. | Compression Testing of 143L at Elevated Temperatures | 11 |
| 5. | Fatigue Testing of 143 | 11 |
| 6. | Fatigue Testing of U-700 | 12 |
| 7. | Fatigue Testing of 143L | 13 |
| C. | Discussion | 13 |
| 1. | High Volume Fraction-High Misfit Alloys | 14 |
| 2. | Low Volume Fraction-Low Misfit Alloys | 15 |
| 3. | Low Volume Fraction-High Misfit | 16 |
| IV. | POROSITY IN SINGLE CRYSTALS | 18 |
| A. | Background | 18 |
| B. | Experimental Methods | 19 |
| C. | Results | 19 |
| 1. | Microscopy | 19 |
| 2. | Quantitative Metallography | 20 |
| 3. | HCF Results | 21 |
| D. | Discussion | 21 |

TABLE OF CONTENTS (cont'd)

| | |
|---------------------------|----|
| V. PUBLICATIONS | 25 |
| VI. REFERENCES | 26 |
| TABLES I - V | 28 |
| FIGURES 1 - 64 | |

I. INTRODUCTION

It is well known that Ni-base superalloys deform in an inhomogeneous manner at both room and elevated temperatures (Refs. 1-6). Local plastic deformation stems from the microscopic shearing of the γ' precipitates (Refs. 1-5), the predominant strengthening phase, and leads to channels of relatively "soft" material. This localized "soft" material is caused by the decreased order in the γ' precipitates. Non-uniform deformation can also be caused by ceramic inclusions, large carbides, eutectic phases or porosity (all of which are commonly found in complex chemistry superalloys). This phenomenon of localized softening is not restricted to Ni-base superalloys, but occurs in most planar slip alloys containing coherent precipitates (Refs. 7-11). In Ni-base superalloys, localized softening accounts for their renowned low fatigue endurance limit to yield strength ratio. Low to intermediate temperature failures generally result from this type of deformation.

The research conducted under this contract includes a comprehensive study of the slip distribution and strain localization which occurs in modern high temperature superalloy single crystals. Similar slip phenomena also occur in directionally solidified and polycrystalline superalloys. Nevertheless, a study of the degree and nature of strain localization in these latter materials would be encumbered by the complex stress and strain states imposed on the individual grains by their neighbors. The availability of precise stress and strain state information in a monocrystalline alloy will be exploited here to determine how strain localization influences failure.

Most research done in the study of superalloy deformation processes can be divided into two categories. Either an atomistic approach has been taken where the emphasis was on the manner deformation occurs in a minute area of material (such as takes place in dislocation dynamics theories) or fractographic and phenomenological studies have been carried out in which large scale macroscopic processes were observed with little attention paid to microstructural considerations. The approach taken here is to combine these two methods into a coherent study of how the atomistic models of plastic strain localization lead to the phenomenological results of failure by crack initiation, void nucleation and cleavage.

The objectives of this research effort were to understand the localization of plastic strain in single crystal superalloys which leads to fatigue failures. Such single crystals fail at ambient and intermediate temperatures by either internal porosity or surface slip initiation by an intrusion-extrusion mechanism. This program classified how different alloys initiate cracks via intrusion-extrusion and how porosity could be modified and controlled by casting parameter variations.

II. INTERPRETATION OF SURFACE SLIP

The characterization of slip bands and shear deformation has been the subject of many studies in the past. The vast majority of these inquiries have used optical techniques to study slip band density and spacing. Very little attention has been paid to the detailed surface morphology of these slip bands. For a given mode of slip deformation, having slip dislocations with the Burgers vector, \bar{b} , one can readily describe, mathematically, the resulting slip band character at the surface of a specimen in general terms.

In order to describe the surface of a uniaxially stressed specimen, we define the right-handed rectangular coordinate system x,y,z such that x is normal to the specimen surface and z is parallel to the stress axis. The unit vectors \bar{i} , \bar{j} and \bar{k} and direction cosines l_1 , l_2 and l_3 have their usual meaning.

The slip offset at a surface where one dislocation has emerged is depicted in Fig. 1. The resulting surface offsets are described by three orthogonal vectors $\bar{\alpha}_0$, $\bar{\beta}_0$ and $\bar{\gamma}_0$ which have the relation

$$\bar{b} = \bar{\alpha}_0 + \bar{\beta}_0 + \bar{\gamma}_0 = |\bar{b}| l_1 \bar{i} + |\bar{b}| l_2 \bar{j} + |\bar{b}| l_3 \bar{k} \quad (1a)$$

We can see that $\bar{\alpha}_0$ is perpendicular to the specimen surface and positive outward and $\bar{\gamma}_0$ is parallel to the stress axis (i.e. $\bar{\alpha}_0$ parallel to \bar{i} , $\bar{\beta}_0$ parallel to \bar{j} and $\bar{\gamma}_0$ parallel to \bar{k}). Therefore it follows that

$$\begin{aligned} |\bar{\alpha}_0| &= |\bar{b}| l_3 \\ |\bar{\beta}_0| &= |\bar{b}| l_2 \\ |\bar{\gamma}_0| &= |\bar{b}| l_1 \end{aligned} \quad (1b)$$

from simple trigonometry. These relationships will become useful when the time comes to do actual measurements. For the case where a number of identical dislocations have passed on the same slip plane, one can define a vector \bar{B} which is the sum of the dislocation Burgers vectors which have passed on that plane and can be given as

$$\bar{B} = \sum_n \bar{b} = \bar{\alpha} + \bar{\beta} + \bar{\gamma} = n\bar{\alpha}_0 + n\bar{\beta}_0 + n\bar{\gamma}_0 \quad (2)$$

Here the vectors $\bar{\alpha}$, $\bar{\beta}$ and $\bar{\gamma}$ are defined as the total surface offset which is a measurable quantity after an induced deformation and are simply given here as the sum of n dislocations which have passed on the slip plane in question.

The description of a slip band is somewhat more difficult since it is composed of a number of discrete slip lines and the distinction between the two must be kept in mind. If we traverse a slip band along the stress axis and measure the values of B at each individual slip line, one may obtain something similar to the hypothetical Fig. 2 where B is now equal to $|\bar{B}|$. For the case of discrete slip lines one can define a

term Ξ such that

$$\Xi = \sum_{z_0}^{z_d} B(z) \quad (3)$$

where Ξ now describes amount of slip contained in a slip band and the distance $z_d - z_0 = d$ is the width of the slip band in the direction of the stress axis. By plotting this term as a function of z , one can graphically illustrate the slip profile of our hypothetical slip band, as shown in Fig. 3. If our term B included only the $\bar{\alpha}$ vectors, Fig. 3 would indeed be a true profile of the slip band.

For very fine slip line spacings it would be possible to consider both B and Ξ as continuous functions thereby modifying equation (3) to

$$\Xi = \int_{z_0}^{z_d} B(z) dz \quad (4)$$

One step further in this line of reasoning would be to define yet another term to describe the quantity of slip in a number of slip bands. This can be done with the term X (defined as being per unit length) where

$$X = \sum_{z=0}^1 \Xi(z) \quad (5)$$

By use of the assumption that all slip bands contain the same degree of slip offset, Ξ , Eq. (5) can be rewritten as

$$X = N \Xi \quad (6)$$

where N is the number of slip bands per unit length. By measuring the slip band density, as has been done many times in other studies of slip deformation, a measure of X/Ξ was actually being made.

To put Eqs. (1-6) in perspective, they are summarized in Table I with their description and the degree of resolution required for their study. It can be seen that slip has been quantized from its smallest dimension, the Burger's vector, \bar{b} , with dimensions of atomic size to an aggregate of slip bands which is on the scale of a test specimen. The study of these various parameters is limited in a physical manner by the experimental technique used to observe them. For instance, X can be measured using very low magnification or by eye, the study of Ξ requires optical microscopic techniques, individual slip lines may be observed using SEM or TEM replicas to study B and the study of individual slip offsets at the surface would be very difficult and has not been accomplished to the author's knowledge.

III. SURFACE SLIP MEASUREMENTS

A. Experimental Procedures

1. Single Crystal Growth and Preparation

Three alloy chemistries were chosen for study with their compositions given in Table II. Single crystals were grown in a high gradient radiation cooling furnace using $\langle 001 \rangle$ oriented seeds in a modified Bridgman arrangement. Crystal orientations were verified using Laue back-reflection techniques. The crystals were homogenized and heat treated according to the schedule given in Table III. Two heat treatment types were given to alloy 143 test specimens. These are denoted as SOL for solution heat treated and SHT for standard heat treated.

2. Compression Testing

Compression specimens, right rectangular parallelepipeds, $0.8 \times 0.8 \times 1.0$ cm, were EDM cut from large crystals. Specimens of the 143 alloy were oriented in both the $[001]$ and $[011]$ orientations and the other alloys in the $[001]$ orientation only. The $[001]$ specimens were aligned such that the axes perpendicular to the specimen faces were $\langle 001 \rangle$ directions. The $[011]$ oriented specimens had one face perpendicular to $\{111\}$. Electropolishing of two specimen sides of the $\langle 001 \rangle$ aligned specimen was accomplished using a methanol and perchloric acid solution with these sides designated "0°" and "90°" having the $[100]$ and $[010]$ normals assigned, respectively. Only the $\{111\}$ surface of the $[011]$ aligned specimen was electrolytically prepared.

Compression testing was conducted in air at room temperature utilizing a servo-hydraulic testing machine. A compression rate of 0.025 cm/min (0.01 in/min) was used with repeated unloading at 0.25, 0.5, 0.75, 1.0, 2.5 and 5.0% plastic strain. During these unloadings, plastic replicas were stripped from the electropolished surfaces to preserve an image of the deformed surface. This nondestructive test procedure allowed for repeated observations using a minimal number of specimens.

Compression at elevated temperatures, 466°C (870°F), was conducted in a high purity all metal testing furnace specifically designed for use in servo-hydraulic testing machines. This furnace is shown in Fig. 4. This system includes a high vacuum capability of 10^{-6} torr at temperatures as well as a Ti-gettered argon atmosphere which has been measured at an oxygen partial pressure of better than 10^{-10} ppm by use of a fast ion conductor Ca-stabilized zirconia cell. It has been found that by using purified Ar, a much lower oxygen partial pressure can be maintained in the furnace than under the available vacuum system. Specimens were methodically cleaned ultrasonically in trichloro-ethylene followed by a rinsing in pure ethanol. These stringent measures were found to be required to clean films that adhere to the electropolished surfaces during storage and test setup.

After test completion the replicas were prepared using standard TEM techniques. A Pt/Pd alloy was shadowed along the stress axis to maximize fine detail resolution and to give a crystallographic reference frame for each micrograph.

3. Fatigue Testing

Square cross section fatigue specimens 0.64 cm square by 2.54 cm long in the gage with threaded ends were machined from the oriented crystals described previously. The flats of the square gage section were oriented perpendicular to the $\langle 001 \rangle$ directions. Two adjacent sides were electropolished to obtain a micro-smooth starting surface.

Fatigue testing was carried out at room temperature utilizing a ramp wave under constant total strain amplitude control keeping the strain rate constant at 0.005 sec^{-1} . Strain amplitudes of 0.4, 0.5, 0.7 and 0.8% were used in testing alloy 143 while an amplitude of 0.7% was used for the other alloys tested. The fatigue tests were interrupted after 1, 5, 10, 25, 50, 100, 200, 500, 1000, 2000 cycles and plastic replicas cast of the electropolished surfaces as described for the compression tests.

B. Results

1. Compression Testing of Alloy 143

Both optical and TEM evaluation of replicas were conducted along with a SEM examination after final specimen testing. Analysis of the replicas were conducted in order of their strain amplitude so that development of slip lines and bands could be followed. The SEM micrographs of the final specimen surface were reviewed so that correlation between optical and TEM replicas could be made.

a. Undeformed

Before deformation, each of the electropolished specimen faces was replicated to record the pretest surface condition. One such surface is shown in Fig. 5. One readily notes that the electropolishing procedure used here results in a slight mosaic pattern on the surface in many regions (see Fig. 5a). This pattern cannot be readily associated with any structure within the material and is therefore considered an artifact resulting from a breakdown of the surface film which forms during electropolishing. This surface pattern, while deleterious to the overall resolution of slip lines, did not hinder our analysis. The surface pattern is seen to have an approximate spacing of 40 nm which is in the range of 100 to 200 atom spacings with an amplitude of roughly 10-20 nm or 30-60 atom spacings. Other regions of the same sample are observed to have a relatively smooth appearance with much lighter undulations as seen in Fig. 5b.

Thin foil TEM micrographs of the solutioned (SOL) and standard heat treatment (SHT) microstructures are given in Fig. 6. In the solutioned condition the average γ' size is $0.1 \mu\text{m}$ while the SHT γ' has an average particle size of $0.3 \mu\text{m}$. Interface dislocations are quite prevalent in the SHT micrograph while the SOL heat treated precipitates are fully coherent.

b. SOL $\langle 011 \rangle$ Stress Axis

After 0.25% plastic compression strain a number of fine slip bands were observed optically as shown in Fig. 7 on both the (100) and (110) planes. Some of these slip planes are seen to stop in mid-crystal suggesting that some slip does not occur throughout the crystal and that dislocations do not pass through the whole crystal.

Examination of TEM replicas of these surfaces given in Fig. 8 show the slip bands to be very uniform with respect to the degree of slip which occurs through them. Very fine slip lines are interspersed in the larger slip bands. These fine slip lines in Fig. 8b have a spacing of ~ 65 nm. Also in Fig. 8b the presence of a pretest fiducial mark (F in Fig. 8b) shows the magnitude of the displacement vector parallel to the specimen surface, β . Close examination shows that this displacement vector is continuous throughout the slip band marked A in Fig. 8b to within 20 nm, nearly the resolution of the replica. This is somewhat of a surprising result. No apparent differences were observed in slip bands on $\{100\}$ and $\{110\}$ planes.

Optical examination of replicas after 0.5% plastic strain reveal wider slip bands which protrude much more from the surface than the above-mentioned slip bands (see Fig. 9) as well as having a much higher density. The (100) surface (Fig. 9a) displays extruded slip bands (material has been expelled from the specimen) which would be expected if the two operable slip planes were acting in concert. A regular spacing of slip was observed in the (110) plane with two active slip planes readily observed. Mobile dislocations on each of these planes have components of their Burger's vectors both into and out of the specimen surface.

Examination of these replicas using TEM shows the slip bands to be quite broad and not readily observed at the standard magnification of 5.4K used here since the slip band is larger than the field of view. As before, the homogeneity of slip through the slip band is remarkable. Very fine individual slip lines are resolvable within each slip band having a spacing of approximately 65 nm. Figure 10 also contains a narrow slip band which is just developing 5.5 μm away from the broad slip band previously described. At this point in its development, it is composed of only five slip lines. Close examination of the slip lines at the very edge of these slip bands reveals that they appear and disappear as one follows their length. This would be caused by a number of dislocation loops on one plane which have intersected the specimen surface in certain areas and not in others or possibly a single loop with a highly convoluted shape.

As strain was increased, the previously observed trend towards higher slip band density, broader slip bands and a greater intensity of slip within each slip band continued. At 1% plastic strain, the previously uniform slip bands have become somewhat more inhomogeneous as shown in Fig. 11. Here a single slip band covers the entire field of view. Within this slip band, however, regions of more intense slip have occurred and are so denoted by arrows.

After 2% plastic deformation essentially the entire specimen is uniformly covered with slip bands as shown in Fig. 12 for the (110) crystal face. Many secondary slip planes are seen to intersect with no observable effect on one another. This suggests that very little debris or dislocation-dislocation interaction occurs near the surface. Individual slip bands jog as they intersect other slip bands, but this is simply the result of slip which occurred previously. Again, the slip occurring within individual slip bands is very uniform with little evidence of individual slip in Fig. 12.

In order to verify the replica images, a SEM examination of the electropolished surface was conducted after compression testing was completed to 5% strain. Two such micrographs are given in Fig. 13a and b for the (100) and (110) specimen surfaces respectively.

Figure 13a shows a number of slip bands on the (100) surface. No sign of the fine slip lines can be observed. A surface roughness, associated with electropolishing, is clearly visible. Higher magnification of this sample revealed little more detail due to the smoothness of the surface resulting in poor secondary electron contrast.

The (110) surface shown in Fig. 13a displays a striking similarity to Fig. 12 where intersecting slip is clearly visible. The SEM micrograph, while at a substantially reduced magnification, clearly reveals the three dimensional aspects of slip analysis with more clarity than does the TEM replica technique. Again, extruded segments of the crystal are plainly visible in this compression specimen.

This SEM analysis has shown many of the same features that were evident in the TEM replica micrographs but with much less detail. It also helps to visualize on a larger scale how deformation is occurring.

c. SHT $\langle 011 \rangle$ Stress Axis

There was essentially no difference in the nature of surface slip in the fully heat treated alloy from the as-solutioned alloy. An example of the (100) surface is given in Fig. 14. At the 0.75% plastic strain level fine slip lines are clearly seen evenly distributed within the broad slip bands. This is the same type of structure previously reported for the solutioned microstructure. Of interest are the fine slip bands above the line of contrast marked A. The overall contrast is lighter here than the base intensity which can be seen between lines B and C. The region above line A is therefore tilted away from the shadowing direction. This would also explain the appearance of these fine slip lines. The cause of this type of slip structure will be dealt with in the discussion portion of this report.

d. SOL $\langle 001 \rangle$ Stress Axis

Comparison was made between $\langle 001 \rangle$ and $\langle 011 \rangle$ oriented crystals in the solutioned condition. Relatively poorer results were obtained from the $\langle 001 \rangle$ oriented crystals with respect to replica integrity. Few replicas of acceptable quality were obtained, so only subjective analysis could be conducted. Figure 15 shows typical slip after compressive deformation to 0.75% plastic strain. This slip band is not as uniform in deformation as was observed for $\langle 011 \rangle$ oriented crystals. Fine slip lines are present within each of the individual small slip bands which is similar to the results found previously.

In order to resolve the individual slip lines within a slip band, higher magnification micrographs were taken after 5% compressive plastic strain. Figure 16 illustrates a fine slip band (between lines marked A and B) composed of fine slip lines. The high magnification of this micrograph shows the slip offsets to be on the order of 50 nm apart with their height undeterminable.

e. SHT $\langle 001 \rangle$ Stress Axis

The $\langle 001 \rangle$ oriented crystal in the standard heat treated condition behaved similarly to the $\langle 001 \rangle$ solutioned specimen, again with little perceptible difference in slip character with γ' precipitate size. An experiment was conducted using a thin foil specimen cut from the electropolished surface after compression testing to 5% plastic strain. This specimen was chemically polished back towards the already electropolished surface thus preserving any slip offsets at the specimen

surface. Using a STEM it was hoped that both a thin foil analysis using transmitted electrons as well as surface detail using secondary electron contrast could be obtained simultaneously thereby revealing the dislocation substructures which yield surface slip lines and bands. The scanning electron mode did not yield sufficient clarity and contrast with these specimens, however. Transmission microscopy was useful in showing the dislocation shearing of γ' particles as in Fig. 17. Here two slip planes are clearly active as was expected from both slip band analysis and a Schmid factor analysis. The large irregular γ' did not act as a great enough barrier to dislocations that it forced them to bow around the precipitates or climb over them, at least at room temperature. Many γ/γ' interface dislocations are also observed in between the large γ' precipitates. These misfit dislocations which are formed between the γ and γ' phase make up the difference in lattice spacing which has been measured at $-.78\%$ (Ref. 12).

2. Compression Testing of U-700

Replicas of undeformed U-700 crystals are given in Fig. 18. A dispersion of fine γ' precipitates is clearly discernible after electropolishing. This allows for a clear frame of reference with respect to crystallographic direction and how the surface slip traces interact with the precipitate particles.

It appears in Fig. 18 that areas exist which are free of precipitates. This is clearly an artifact of polishing parallel to $\{001\}$ planes. Since the particles are aligned on these planes, the polish plane will intersect regions of γ matrix between the rows of γ' giving the illusion of precipitate free regions.

After a plastic compression strain of 0.25%, very fine and discrete slip lines were observed throughout the sample surface. Figure 19 shows three of these slip lines on the 90° side. The replica film failed along these very sharp slip lines causing the large white bands where the replica has separated.

Fine slip lines were also observed after 0.5% plastic strain. Figure 20 shows a number of these slip lines intersecting the γ' precipitate dispersion on the 90° side. Close examination of these slip lines, as in Fig. 21, reveals a fine structure associated with them. Slip band 1 of Fig. 20 is clearly composed of a number of very closely spaced slip lines as is the slip band of Fig. 21a. Each of the slip lines in Fig. 21a have identical active Burger's vectors giving the false impression that the γ' particles are smeared. In actuality, slip band 1 is $0.11\ \mu\text{m}$ wide and composed of roughly four individual slip lines, of which the two to the right have undergone much larger strains and in most instances obscure each other. These slip lines are $46.2\ \text{nm}$ apart. Slip offsets this close together are not readily separable and their heights are not determinable.

A number of scratches traverse slip band 1 and are offset by $0.28\ \mu\text{m}$ along the slip band length. This quantity is defined as $\Xi_\zeta = \sum B_\zeta$ (where Ξ_ζ is the component of the total slip band Burger's vector Ξ in the direction of the slip line length ζ ; see Ref. 13 for the definition of Ξ) and can be translated to the passage of ~ 1120 or ~ 1580 individual dislocations of Burger's vector 2.5\AA depending on the direction of the Burger's vector. With an optical measuring accuracy of $\pm 0.1\ \text{mm}$ at a magnification of 25,000, an error in dislocation count of ± 100 dislocations is expected. Since there appears to be a component of the Burger's vector out of the polish plane, we can assume that 1580 dislocations traversed the four slip lines identified. For a polished (100) surface this assumes slip of $[110](111)$ type dislocations exclusively. The sense

of the applied stress was $[001]$ thereby leading to the conclusion that these dislocations must be edge in character for maximum mobility. This is in keeping with the acceptance of edge type dislocations having much higher mobility than screws in an ordered FCC lattice.

Slip lines 2 and 3 of Fig. 20 are very distinct and were formed on single planes as far as can be discerned with the resolution of these replicas (see Fig. 21b). Again, by observing the slip offset of surface scratches, Fig. 21b, slip lines 2 and 3 are composed of slip by ~ 1150 and ~ 5970 individual $[\bar{1}10](111)$ dislocations, respectively.

The slip bands can take on a different appearance on the 0° side of the specimen. Shown in Fig. 22 are a number of slip bands after 0.75% plastic strain. Notice that the pronounced dark band in Fig. 20 is absent. Since this band is the result of protruding material, it would indicate that slip is totally in the plane of polish on this side.

Slip line 1 of Fig. 23 was formed by the passage of ~ 1880 dislocations. This replica was taken after 1% plastic compressive strain on the 90° surface. This set of slip bands appears in different contrast with those of Fig. 20. These are composed of an essentially solid white band. This is a result of the replicating material stepping down as one proceeds along the shadowing direction. Furthermore, many white holes are on the left side of each slip line indicating that the material on the right slipped down and to the right. The white holes are created where the slip line cut an individual γ' particle. The number of dislocations forming the slip lines is of the same order at $\epsilon_p = 1\%$ as at $\epsilon_p = 0.5\%$. By observation there appears to be more slip lines at 1% strain but this is purely subjective. Through this strain however, no evidence of cross slip was encountered and the slip lines remain very finely defined.

Up until this point, slip occurred in a very simple fashion with all of the deformation concentrated on single slip planes in spite of the fact that the crystal is in a multiple slip orientation. At 1.5% plastic strain, slip becomes much more complex with large areas of cross slip occurring. A typical surface replica is given in Fig. 24 from the 90° surface. For notational purposes the groups of slip lines in Fig. 24 are denoted as bands 1, 2, and 3 as shown. From the way in which the slip lines are offset, the number order of these lines is the order in which they become active. It is especially noteworthy that lines 2 abruptly end at lines 1 probably in a pileup or alternatively as the result of cross slip. These slip lines have a much larger accumulated Burger's vector than those observed previously. For example, a segment of slip line set 1, magnified in Fig. 25, shows offsets of 220, 440, 3330, 370 and 670 \bar{b} reading from right to left. This can be translated into a map of the slip region as given in Fig. 26 where the abscissa is distance perpendicular to the slip lines and the ordinate is the accumulated Burger's vector of each slip line. In this case, slip appears completely parallel to the polish plane and these dislocations can be deduced as $[\bar{1}01](111)$ type.

The dislocation of region 2 probably cross slipped off of 1 due to a buildup of debris resulting in hardening. The darkest of these bands (in the center of 2) has a \bar{b} nearly perpendicular to the polish plane resulting in the dark contrast associated with ledges. The γ' precipitates are also not sheared to the sides very much. From the above observations, the active slip planes and Burger's vectors can be determined and are shown in Fig. 27. Now the amount of slip on the type 2 slip lines can be measured since the angle of the Burger's vector with the surface normal is known to be 45° . This yields an approximate \bar{b} for the largest slip line of group 2 in Fig. 24 of 315 \bar{b} . This is on the same order as the magnitude of slip in the region 1 slip lines.

Regions in which either cross slip or duplex slip occur are especially interesting because of their complex nature and the insight they lend to the interaction of slip bands. Figure 28 illustrates two such instances on the 90° surface. These high magnification micrographs show instances of cross slip (Fig. 28a) and duplex slip (Fig. 28b). The two primary slip lines in Fig. 28a have fine slip occurring to their right, apparently resulting from cross slipping screw dislocations off the primary slip plane. Cross slipping should be relatively easy in the cube orientation used here, since all of the slip planes are stressed equally. The cross slip lines are not continuous across the lighter of the two slip lines but are offset by $0.11\ \mu\text{m}$, evidence that slip on this latter plane occurred after the cross slip events. It is believed that this region experienced cross slip because the fine slip lines originate at the heavy slip line. Duplex slip can be discounted since no barrier exists to dislocation motion at the slip band and the cross slip events occurred randomly.

The duplex slip shown in Fig. 28b is quite discernible from cross slip in that the primary slip lines are offset by the component of the Burger's vector parallel to the secondary slip lines. In Fig. 28b the primary slip band 1 has been offset by the duplex slip band 2 by $625\ \text{nm}$. Both slip bands 1 and 2 are complex, (i.e., made of a number of slip lines) with slip band 1 composed of four slip lines of equal height spaced $30\ \text{nm}$ apart.

After 2.5% plastic strain, the slip bands take on a much different character as revealed by replication. Figure 29 shows two areas of the 90° surface, one with only primary slip active (Fig. 29a) and Fig. 29b illustrating a cross slip region. The large dark bands are indicative of high slip steps. Calculations, taking into account the slip height of the surface offsets in Fig. 29b, revealed that the two largest offsets were formed by between 2000 and 3000 dislocations with their Burger's vectors highly inclined to the polished surface normal. The magnitude of these offsets are on the order of those observed previously (see Figs. 20 and 21 for plastic strain of 0.5%) for much lower strains.

The cross slip mechanism is well defined in Fig. 29b where the slip steps in light contrast terminate on both sides at slip steps having the darker contrast. Some of the light contrast steps are quite high indicating that cross slip had occurred numerous times on one plane resulting in large localized slip offsets.

3. Compression Testing of 143L

The microstructure of the 143L alloy prior to deformation is shown in Fig. 30. One unusual feature of this microstructure is the asymmetric coarsening of the γ' into elongated rods. All areas of the specimen did not appear asymmetrically coarsened as that shown in this figure, but the γ' in all cases showed some evidence of elongation. The average γ' size was measured to be $0.4\ \mu\text{m}$ on the cube edges. The average γ' volume fraction as measured from the replica micrographs is 53%.

Very few slip bands were observed after only 0.25% plastic strain. One typical slip band is shown in Fig. 31. This slip band is $2.8\ \mu\text{m}$ wide and is seen to be composed of many very fine slip lines. In one area 38 slip lines were counted in this slip band.

The slip bands were not noted to expand upon straining to 0.5% plastic strain and were measured to be approximately $3\mu\text{m}$ wide. The severity of the individual slip offsets has increased somewhat, however. Figure 32 shows this clearly. Typical slip offsets, perpendicular to the specimen surface, were measured to be 25 nm with the largest being 75 nm.

Conjugate slip was first evident in the specimen plastically deformed to 0.75%. Slip remained fine as noted above through 1% compressive strain. Increasing strain appears to be accommodated in existing slip lines since neither slip band widening nor a greater number of slip bands were evident.

Figure 33 depicts the first observation of cross slip at 1.5% strain. Typical slip heights have reached 55 nm thus indicating that slip line coarsening is continuing.

4. Compression Testing of 143L at Elevated Temperatures

Replication of compression specimen surfaces which were tested at elevated temperatures was not successful. Using the high purity furnace described above still allowed sufficient oxygen partial pressure to cause surface replicas to be obscured by an oxide film. Visual inspection of specimens after testing did not show any evidence of oxidation; however, the resolving power of the replicating technique is so high that the thinnest oxide film seriously decreases the resolution of this technique. Figure 34 shows that the γ' precipitates readily apparent in the previous micrographs are obscured by the patchy oxide film. Many attempts were made to minimize this oxide layer, some of which have been discussed in the experimental methods section above, but to no avail.

5. Fatigue Testing of 143

Testing conducted at a strain amplitude of $\pm 0.7\%$ will be discussed in detail here initially. Variances in strain amplitude from this base line will be noted as required.

At low numbers of fatigue cycles ($N < 10$) few slip lines were observed on the specimen surface and most of these appeared as widely spaced events. Figure 35 is typical of the surface after one fully reversed cycle. Each of the three slip bands shown here already exhibits signs of spreading. Slip-band 1, for instance, is composed of one highly strained slip line at the center and two or three very light slip lines on either side. Slip bands 2 and 3 are composed similarly.

After 50 cycles, the number of slip bands has increased substantially to the point where the entire specimen surface is covered by slip of varying degree. Figure 36 shows this dramatically. Remembering that slip lines of light and dark contrast represent slip of opposite Burger's vectors, one sees that there is a definite undulating pattern in the surface slip morphology. The surface has, for instance, a number of slip steps up followed by a number of slip steps down. A higher magnification image of these slip lines is given in Fig. 36b, where light contrast lines at the lower left are step-down slip lines (since the shadowing direction is from left to right) and the dark contrast lines are step-up slip lines. Thus a trough, or more commonly referred to as an intrusion, developed in the region defined as A in Fig. 36b. This pattern is repeated roughly on a 1-4 μm scale. These surface undulations are the beginning of intrusions and extrusions which have been cited extensively in the literature as fatigue crack initiation sites in FCC solid solutions.

No visible differences in slip morphology could be discerned from 50 to 200 cycles. Figure 37 can be compared to Fig. 36, which shows no measurable increase in intrusion aspect ratio where slip has been uniformly dispersed throughout the length of the gage section.

Failure occurred after 1593 cycles with the fatigue crack initiation site identified as a surface slip line on one of the specimen sides that was not electropolished. An SEM analysis showed the crack to initially follow a (111) plane away from the initiation site with no inclusions or pores visible (see Fig. 38). Replicas of surface slip revealed identical features to those observed in Figs. 36 and 37. An extensive study was made of the surface in order to locate surface related fatigue crack initiation regions where small microcracks, not leading to failure, may have developed. No such initiation sites were observed. It appears that the initiation process is localized to one specific region.

6. Fatigue Testing of U-700

Relatively few slip lines of a very discrete nature were visible after 10 fully reversed strain cycles. One typical slip band after 10 cycles is given in Fig. 39a. Three very severe slip steps are evident with two fainter lines above them. Within a number of slip bands, individual slip lines were noted which were composed of opposite Burger's vectors. This results in the very beginnings of intrusions and extrusions as noted in Fig. 39b. Here the two slip lines denoted as A and B result in a narrow intrusion 83 nm wide and 35 nm in depth. Similar intrusions and extrusions were visible after one fully reversed cycle.

The slip bands widened as cycling continued. Figure 40 shows a very coarse slip band with a large number of fine slip bands in its immediate vicinity. The fine slip lines are of the opposite nature to the coarse lines as indicated by their relative intensities.

A lower magnification photomicrograph shows another intrusion after 100 cycles in Fig. 41a. A magnified view is given in Fig. 41b where two intrusions separated by an extrusion are clearly visible. Conjugate slip was first observed at this point in the cyclic testing.

Three hundred cycles have resulted in slip steps which approach the resolving limit of the replicating technique utilized here. This results in the appearance of features in the slip lines which have not previously been seen. Figure 42 illustrates such a case in which two conjugate slip planes intersect. The waviness of the one slip line is due to its traverse over the protruding γ' particles.

Failure was initiated at surface slip traces after 6945 cycles. The initiation site is given in the SEM micrograph of Fig. 43. Cracks were seen to cover the surface of the gage section, all starting from surface slip traces. The fracture surface contained many faceted regions at the surface, indicative of surface related crack initiation. Multiple initiation led to crack linking resulting in a circumferential crack leading to failure.

A typical replica of the surface is given in Fig. 44 in which highly localized slip is shown. This particular instance illustrates an extrusion, in which a narrow sliver of material is protruding from the surface. The slip band is quite narrow being only 1 μm wide. No evidence of cracking originating at slip lines on this electro-polished surface was found.

7. Fatigue Testing of 143L

After one fully reversed strain cycle to a total strain amplitude of 0.7%, slip bands were found which were composed of many very fine and closely spaced slip lines. Each of the slip lines in a particular band were composed of identical character offsets which could only be formed by identical Burger's vectors (see Fig. 45). Conjugate slip is also evident. Typical slip offsets of 20 nm are shown in this figure.

The slip bands did not possess features such as width or slip line density that could be thought of as distinguishable for this mechanical history. Two such slip bands are depicted in Fig. 46. In these two instances both very dense slip line density bands as well as bands composed of only a few slip lines are found after 10 strain cycles. Cross slip as well as conjugate slip are well established. Slip bands, regardless of size and extent, remain composed of similar character slip lines. Two adjacent slip bands denoted as A and B in Fig. 46a are of opposite nature.

A subgrain boundary is visible in Fig. 46b in the lower left-hand portion of the micrograph. This boundary is distinguishable by the elongated and irregular γ' precipitation. The fine slip lines to the right of this boundary are seen to stop at the boundary or to extend only a short distance into the adjacent subgrain.

No coarse slip lines were found in cycling through 1000 cycles as shown in Fig. 47. These two micrographs taken after 50 and 1000 cycles illustrate the small degree of change that occurs in the slip band and slip line morphologies. None of the slip lines measured in this cycle interval were higher than 90 nm with typical slip lines only 35 to 50 nm in size through failure which occurred at 1642 cycles.

C. Discussion

Our discussion of strain localization in superalloys as observed through surface replication techniques will be divided based on the two characteristics of the alloy considered. These two characteristics are the volume fraction of γ' and the γ/γ' misfit as measured at ambient temperatures. Early superalloys such as U-700 usually are considered to have a relatively low volume fraction of γ' typically in the range of 30 to 40%. Modern alloys which were developed for higher temperature strength such as Mar M-200, Mar M-246, P&W 1480 and 143 have γ' volume fractions approaching 70%. The γ/γ' misfit of superalloys has undergone considerable change during the evolution of these alloys. Based on the work of Mackin and Kancheev (Ref. 13) it has been commonly assumed that low misfit superalloys are required to maintain high creep strengths. Therefore, most of the commercially utilized alloys have very low misfit strains. Most recently it has been demonstrated that some high negative misfit alloys maintain creep strengths superior to commercial alloys thus opening the way to stronger alloys at higher temperatures.

The alloys to be discussed here can be divided into four groups; low volume fraction-low misfit such as U-700, low volume fraction-high misfit such as 143L, high volume fraction-high misfit such as 143, and high volume fraction-low misfit such as Mar M-200. The first three alloys were tested in the present study and will be thoroughly discussed while the latter alloy will be referred to as required.

1. High Volume Fraction-High Misfit Alloys

The most striking feature which has been observed here, in all of the specimens tested, is the extreme uniformity of slip deformation throughout an individual slip band. Figure 48 graphically displays how these large slip bands are composed of many individual slip lines with a uniform spacing of approximately 50 nm. Each of these slip lines is composed of an integral number of Burger's vectors corresponding to the number of dislocations that have passed on each individual slip plane.

The compression testing experiments on 143 were done in such a way so as to determine both the effects of orientation of the crystal to the applied load and the γ' size on the slip character. It is concluded that crystal orientation has little effect on the nature of slip in these alloys, at least for the selected orientations. Both the $\langle 001 \rangle$ and $\langle 011 \rangle$ oriented crystals displayed dispersed slip with no apparent change in slip height or slip band spreading. In the two orientations so studied, only one slip plane was activated. These crystal orientations were chosen because they should have multiple slip planes in operation. Care was taken to assure proper specimen alignment, but this could only be assured to within 2° . Since it is highly unlikely that the aim orientation was obtained exactly, any slight deviation may activate one slip plane preferentially. Similarly, γ' size, as changed in the solutioned and standard heat treated alloys, did not affect the nature of local plastic strains to any great degree.

The following question needs to be resolved: by what mechanism do the slip lines become so regularly spaced and of nearly the same B value? This can be done with reference to Figs. 5b and 16: the thin foil micrographs of the as heat treated and deformed microstructures. The noteworthy difference here is that after deformation many more interface dislocations are present surrounding the γ' precipitates. These additional dislocations are formed during the deformation process when many dislocations are being generated at sources within the crystal. When the γ' precipitates are coarsening during their heat treatment they are initially dislocation free. However, due to their large negative misfit, dislocations need to be present to accommodate the mismatch in lattice spacings. It has been shown that these dislocations must come from sources other than the interfaces themselves. It is also apparent that strains continue to exist after aging due to the rectangular shape of the precipitates. As more dislocations are generated during mechanical deformation they are now available to interfaces to further relieve these strains.

One can now envision a mechanism that will lead to local strain hardening on individual atomic planes as shown in Fig. 49. At the onset of deformation a source becomes active and generates glide dislocations on a primary slip plane. The ensuing dislocations will cut through the γ' precipitates (Fig. 49a). Some will be trapped at the interfaces to take up the mismatch strain while the others that shear the precipitates will form debris while also cutting the present network of interface dislocations. A number of dislocations will follow this path forming a slip line at the surface of the crystal. When the buildup of debris and the saturation of interface

dislocations occurs, this slip plane now becomes a path of high resistance, Fig. 49b. Due to a dislocation pileup at one of the γ' precipitates, a cross-slip event will occur (Fig. 49c). The dislocations are now able to resume primary glide, having avoided the high debris region, and will form new fine slip lines which are approximately the width of the debris channel formed on the previous slip plane. This process will continue with the slip band spreading and being composed of more and more evenly spaced fine slip lines of nearly the same slip height (Fig. 49d).

As one will notice this process is independent of the source distance from the specimen surface assuming that the spread of the slip band is governed solely by the buildup of debris on the individual slip planes. This may have implications as to the nature and severity of planar slip in this type of alloy. Similar alloys with lower misfit or no misfit will interact with glide dislocations differently. Fewer interface dislocations will interact at a slower rate with glide dislocations allowing the fine slip lines to become deeper before they are forced to cross-slip to avoid the high debris channel. A no misfit alloy such as Mar-M200 will always contain forest dislocations which will eventually form debris that will force the cross-slip mechanism.

Superalloys are noted for their planar slip as cited in the introduction. One of the reasons for this is their very low stacking fault energy, SFE, caused by their high alloy content. This does not allow for a high degree of cross-slip of glide dislocation segments yielding planar slip. By raising the SFE of the γ matrix, easier cross-slip will be allowed. According to the model postulated here, this should act to allow the slip bands to spread more easily, in that the back stresses (caused by the debris buildup) necessary to cause cross-slip will be reduced.

2. Low Volume Fraction-Low Misfit Alloys

The results of the compression loading of single crystal U-700 are very different from those of alloy 143. In the latter case, slip occurred over very broad regions; that is, the slip was dispersed. In this instance the slip lines were very discrete with many dislocations passing on a single slip plane. This is referred to as localized slip.

Many references (Refs. 7,15-17) are made in the literature to the low relative fatigue strength ratio (defined as σ_f/σ_y where σ_f is the maximum cyclic stress required to fail a specimen in a given number of cycles and σ_y is the yield stress) of coherently precipitating alloys versus dispersion strengthened or solid solution strengthened alloys. Ni-base superalloys provide an excellent example of this class of coherently precipitating alloys. The classical explanation for the low fatigue strength ratio is that due to the coherent nature of the particles. For each particle on the slip plane, a dislocation cutting a precipitate weakens it slightly by reducing its effective cross-sectional area and bringing about a region of decreased order. This makes it easier for the next dislocation to shear the precipitate field and so on yielding "weakened" planes in which fatigue cracks can initiate and propagate.

It is obvious that in going from alloy U-700 to alloy 143 a change in slip mechanism has been made. In order to understand this mechanism change, one must first recognize the differences in the two alloy types. U-700 was first developed as a high strength superalloy in the 1950's. At this time, alloy development favored zero misfit alloys (where the γ matrix and γ' precipitates have the same lattice parameter) and alloys having γ' volume fractions of 30-40%. (For the time being, grain boundary strengthening additions will be neglected since they play no role in the

single crystal form of these alloys.) On the other hand, alloy 143 is an experimental alloy developed in the early 1980's specifically for single crystal applications with particularly interesting properties in the single crystal form. It has a large negative misfit, $\delta = -0.78\%$ (Ref. 12) and like other contemporary high strength superalloys a larger γ' volume fraction of 65-70%.

U-700 is relatively weak in comparison to 143 due to its lower γ' volume fraction and also fewer and less effective solid solution strengthening elements. The mechanism of shear deformation in these lean alloys was reviewed by Gleiter and Hornbogen (Ref. 19). Here it was shown that shearing of the γ' precipitates by paired $a/2 \langle 110 \rangle \{111\}$ type dislocations leads to the creation of ledges on the precipitates. These ledges would repel further dislocation motion on the same plane due to increased misfit stress fields. It was thus deduced that higher misfit precipitate alloys would have a propensity to have "...an increased number of slip lines with decreased height...". This is exactly what has been demonstrated here. The low misfit alloy which is expected to have low repulsive stress fields in the vicinity of shear ledges should result in very localized slip, while an alloy with high misfit strains will have high ledge stress fields thereby forcing dislocations to cross-slip on to adjacent slip planes to move. It will be demonstrated that while the results are as predicted, the cause is more attributable to γ' volume fraction than misfit. Furthermore, this mechanism was devised for coherent precipitates. Alloys such as 143 contain semi-coherent particles which add the interaction of glissile and misfit dislocations as a further slip dispersal mechanism.

3. Low Volume Fraction-High Misfit

The mechanisms described above fit the experimental evidence quite well. The two alloys discussed so far have had quite different volume fractions of γ' , and it might be expected that precipitate volume fraction would play a crucial role in deformation. An alloy was devised, based on the 143 alloy but having a lower γ' volume fraction equivalent to that of U-700 while maintaining the high misfit caused by a high Mo content (analogous to the Re alloying effects). This was done by adding the atomic percent of Al and Ti (the γ' forming elements) in U-700 and making the 143 Al and Ta atomic percent add up to this value in the same ratio. This led to the alloy 143L used here.

Compression tests indicate that this new alloy is somewhat in between U-700 and 143. Where U-700 has very intense slip bands after only 0.25% plastic strain and 143 reveals very dispersed slip to the point where individual slip lines are not distinguishable, 143L displays slip bands composed of finely spaced yet discrete slip lines.

Another alloy in which the surface slip has been studied through TEM replication is the binary Ni-Al system (Ref. 20). The γ' volume fraction and γ/γ' misfit are known for this system, so interpretation of the data is straightforward. In Ref. 20, a lean alloy was studied with only 25% γ' but having a large positive misfit of 0.50%. Under fatigue loading, discrete slip lines were quite pronounced with crack initiation occurring in these slip lines.

High volume fraction γ' alloys with low misfit have not been studied in this effort because of time and monetary constraints. Typical of these types of alloys are the common commercial alloys Mar M-200, Mar M-246, Rene 95 and P&W 1480. There is no high resolution TEM replica work available on any of these alloys. Optical examinations have been made of slip traces in Mar M-200, however (Refs. 21,22). What is typically referred to as coarse planar slip at a magnification of 100X was observed. It has been shown here that in 143 low magnification replicas display what would also be considered coarse planar slip (see Fig. 9). Upon high magnification observation, however, these slip bands show more the character of diffuse slip. Figure 10 illustrates this for the same specimen surface as shown in Fig. 9. The choice of magnification and resolving power would lead one to quite different conclusions in this case.

A TEM examination of slip in Mar M-200 at various temperatures was conducted (Ref. 23) and showed at room temperature that slip was localized to bands approximately $0.6 \mu\text{m}$ wide. This is approximately the slip band width achieved in the 143 specimens during fatigue where the slip band widths were measured to be in the range of 0.5 to $6.5 \mu\text{m}$ during the course of cycling. From this evidence it can be concluded that Mar M-200 type alloys display slip somewhat coarser than 143, but not nearly so coarse as U-700.

At this time a semi-quantitative graphical representation of plastic strain localization in superalloys can be made as functions of both misfit, $|\beta|$ and γ' volume fraction, f , (see Fig. 50). A number of features are shown here which summarize the work reported thus far. Slip can be loosely categorized into three modes, coarse, fine and dispersed. Coarse slip, typical of that found in U-700 and other lean alloys, is characterized by narrow slip bands and sharp offsets composed of few slip lines which have been formed by the passage of many dislocations. In cases when the dislocations are forced to cross slip onto many adjacent slip planes dispersed slip occurs. Here, very few if any dislocations pass on exactly the same slip plane. The slip bands are thus quite wide with evidence of slip lines within. In between these two extreme cases is what is referred to here as fine slip. Some of the features of both the above-mentioned types are present in this case. Broad slip bands composed of many fine and discrete slip lines characterize this form of strain localization. Our experiments, and those noted in the literature cover a wide range of misfit, γ' volume fraction and γ' size. Figure 50 depicts the placement of these alloys on a misfit-volume fraction-slip map to the best of our knowledge at this time.

The effect of misfit on slip character is seen to be a second order effect with respect to volume fraction. The U-700, Waspaloy (Ref. 5), and binary alloy noted above all maintained very coarse slip. 143L displayed fine slip while Mar M-200 (with limited data) showed similar slip band widths and thus also fine slip behavior. Dispersed slip was typical of 143 which displayed a slip character much different than other superalloys because of its anomalously high misfit and volume fraction combination.

This figure also has significance to the fatigue data generated here and from many other sources. All of the alloys below the fine-dispersed boundary have been shown to initiate failures at surface slip lines, while those alloys above this boundary fail at asperities such as pores or cracked carbides. Single crystal Mar M-200 has displayed failure at both surfaces and asperities (Ref. 22), depending on temperature and loading frequency substantiating its positioning on the fine-dispersed boundary.

IV. POROSITY IN SINGLE CRYSTALS

A. Background

Fatigue studies reported on columnar grain and single crystal Mar-M200 identified both cracked carbides and casting porosity as failure initiation sites (Refs. 23-25). From these results, it was concluded that in uncoated, elevated temperature fatigue testing of directionally solidified superalloys, microstructural inhomogeneities such as pores and carbides result in internal fatigue initiation.

Recent development of commercial superalloy single crystal chemistries has led to low carbon contents which minimize carbide precipitation (Refs. 25,26). With this development, porosity remains the only internal fatigue crack initiation site in these alloys. Therefore, in order to increase the fatigue lives of such alloys, it has become apparent that porosity must be minimized or at least controlled. To accomplish this, a better understanding of the origins of porosity in cast single crystals is necessary.

A recent study on the low cycle fatigue properties of superalloy single crystals at elevated temperatures has shown that fatigue failures originate at internal porosity (Ref. 27). Relative fatigue life was found to be independent of several γ' microstructural variations. These fatigue lives were comparable to those reported elsewhere for other superalloy single crystals (Ref. 24,28). The evidence indicates that other single crystal alloys originate fatigue cracks by a similar mechanism.

Porosity is inherent in most castings and is due, in part, to shrinkage associated with the molar volume decrease which occurs during solidification. Superalloy single crystals are grown in investment molds by drawing the melt vertically through relatively high thermal gradients of approximately 30-70°C/cm (Ref. 25). During the withdrawal process, trapped regions of liquid within the interdendritic regions can form. When these trapped pools solidify and shrink, they can no longer be supplied with liquid to take up the volume change and a small pore is developed. Shrinkage pores of this type are a common defect in directionally solidified superalloys (Ref. 29). These pores, which form upon casting, are typically 10-20 μm in diameter and depend on the thermal gradient, withdrawal rate and shrinkage factor of the alloy. The low solubility of gas in Ni alloys and vacuum melting practices minimize the amount of gas porosity present.

The post-solidification heat treatment of single crystals begins with homogenization; i.e., heating above the γ' solvus for a period of time sufficient to allow diffusional minimization of the composition gradients formed during solidification. The time-temperature schedule is based on the degree of homogeneity desired and the diffusivities of the alloying elements. During this high temperature homogenization, porosity was found to change in size, volume fraction or size distribution through diffusivity of vacancies through the lattice (Ref. 30).

Since many fatigue failures of superalloy single crystals at elevated temperatures are initiated by localized strains in the vicinity of pores it was believed that this form of strain localization should also be studied. To study subsurface fatigue crack initiation, the most fruitful approach is to alter the initiation site in some manner. The porosity noted above can be changed in size by altering the solidifica-

tion rate. By increasing the solidification rate, the microstructure can be scaled down thereby reducing the pore size while maintaining dendritic solidification. Also of interest is the degree of microporosity present as cellular solidification conditions are approached.

B. Experimental Methods

A model nickel-base superalloy, alloy 143, used in this study was chosen because of its ease of growth, its similarity to single crystal alloys used commercially and its relatively simple microstructure. The composition of the alloy studied is 5.8 Al, 14.3 Mo, 6.0 Ta and bal. Ni in weight percentage. The alloy was fabricated from commercially pure elemental additions, with particular attention paid to minimizing the carbon content.

Seeded single crystals, 15.9 mm in diameter, were grown in the $\langle 001 \rangle$ direction under vacuum using a liquid tin cooling bath as described in Ref. 31. This resulted in an approximate gradient of $200^\circ\text{C}/\text{cm}$ at 1350°C , the liquidus temperature of alloy 143. The withdrawal rate used during crystal growth, R , was varied from 1.27 cm/hr to 254 cm/hr as given in Table IV.

The crystals were sectioned at a constant metallostatic head pressure of $8.73 \times 10^3 \text{ N/m}^2$ or 0.09 atm. Specimens from each crystal were metallographically prepared for quantitative analysis in the as-cast condition and after a homogenization heat treatment of 1315°C for 24 hrs. Metallographic polishing gave excellent results which left pores in high contrast to the background matrix while leaving no signs of smearing. Quantitative metallography was performed on specimens grown at each rate and heat treatment. Areas measured were approximately 0.5 cm^2 with a minimum detectable pore diameter estimated at $2 \mu\text{m}$. Subsequent etching and optical metallography revealed microstructures associated with variations in growth rate and heat treatment.

High cycle fatigue tests were conducted on the above single crystal specimens. Testing was carried out in a servo-hydraulic testing machine under sinusoidal loading in load control with a maximum stress of 700 MPa and an R ratio ($\sigma_{\text{min}}/\sigma_{\text{max}}$) of 0.1. All testing was conducted at ambient conditions utilizing a load frequency of 10 Hz. The cycle life of each crystal was monitored and fracture surfaces examined both optically and using a SEM to identify initiation sites.

C. Results

1. Microscopy

Figures 48-53 illustrate both the transverse and longitudinal microstructures resulting from each of the growth rates used in this study. Growth at 1.27 cph, Fig. 48, resulted in a "hazy" dendrite pattern showing the first signs of secondary arm branching in the transverse view with no secondaries visible in the longitudinal view. The primary dendrite arm spacing was measured at $260 \mu\text{m}$. At 2.54 cph the transverse view is beginning to show signs of tertiary dendrite arm growth with the dendrites being more clearly delineated than previously shown, Fig. 49, and having a spacing of $242 \mu\text{m}$. A number of interdendritic precipitates are clearly seen along with some porosity. The transverse view shows a very faint secondary dendrite arm pattern also with interdendritic precipitates.

The crystal grown at 12.7 cph is shown in Fig. 50. The primary dendrite spacing, $197\ \mu\text{m}$, is considerably smaller than in previously observed specimens. Scaled down with the dendrite size are also the interdendritic porosity and precipitation. The secondary dendrite arms are fully developed in both transverse and longitudinal views. The dendrite arm spacing was further reduced to $\lambda = 178\ \mu\text{m}$ for the crystal grown at 25.4 cph which otherwise resembles the previously mentioned specimen.

The two fastest growth rates of 127 and 254 cph resulted in fine dendrite arm spacings of 133 and $124\ \mu\text{m}$, respectively, with the latter exhibiting extensive secondary and tertiary dendrite formation. Pores were difficult to observe in the etched state due to their relatively small size.

After homogenization at 1315°C for 24 hrs all traces of chemical inhomogeneity were lost, but heavy etching revealed a complex subcell structure in all of the crystals. Examples of these cells are given in Fig. 54 for the specimens grown at 1.27 and 127 cph. In Fig. 54a two distinct categories of subcell could be identified. Larger regions of the crystal, typically 0.3 mm in diameter, were bounded by deeply etched boundaries while within these regions, a shallow etched boundary network averaging 40 to $80\ \mu\text{m}$ in diameter existed. All of the pores observed here lie at the deeper etched boundaries.

Growth at 127 cph resulted in subcells all having boundary etching of approximately the same magnitude, but a vestige of the larger cells could still be discerned. The larger cells here are bounded by a more continuous boundary in which the smaller subcells are contained. These cell sizes are comparable to those observed in the other specimens. The porosity was found consistently at triple or quadruple points of the larger cells with the largest pores existing at the intersection of a number of cell and subcell boundaries.

2. Quantitative Metallography

The results of the quantitative metallographic analysis are given in Table IV where V_v is the volume percent porosity, \bar{L} is the average linear intercept of the pores, σ_L is the standard deviation of \bar{L} and \bar{r} is the average pore radius calculated as $\bar{r} = 3/4 \bar{L}$. The standard error about the mean shown for the average pore radius is given for 3σ confidence. Figure 55 illustrates graphically how the volume percent of porosity changes with growth rate.

In the cast condition the volume percent porosity increases rapidly from growth rates of 1.27 to 2.54 cph with a gradual decrease occurring at faster growth rates. After homogenization a gradual increase in porosity was observed between 1.27 and 2.54 cph growth rate. A plateau was achieved between growth rates of 2.54 and 127 cph where scatter in the data was greater than experienced before. At a 250 cph growth rate the volume of porosity increased substantially from $\sim 0.10\%$ to 0.35% .

The average pore radius data for the as-cast specimen, given in Fig. 56, shows a slight decrease in pore size with increasing growth rate with an average pore radius of $\sim 6.3\ \mu\text{m}$ in crystals grown at 1.27 cph decreasing to $\sim 4\ \mu\text{m}$ at rates of 127 and 250 cph. Homogenization resulted in all pores having radii of $\sim 6\ \mu\text{m}$.

3. HCF Results

The results of high cycle fatigue testing are given in Table V along with the number of cycles to failure and initiation sites as observed by optical and scanning electron microscopy. For the crystals grown at rates ranging from 2.54 through 25.4 cph, their fatigue lives are seen to be equivalent. All but one specimen initiated failure at internal porosity. One such pore is shown in Fig. 57 which initiated failure in specimen UR-9-2. The typical initial crack growth region perpendicular to the stress axis is visible adjacent to the pore in the center of this specimen.

Surface slip was found to be the initiation site of one failure, UR-9-1, which was grown at 25.4 cph. This did not result in an extended fatigue life as may have been expected. This specimen failed at nearly the identical cycle life as UR-9-2 which was cut from the same single crystal. Figure 58 shows the fracture surface of this specimen. No easily identifiable initiation site could be determined. It is thought that initiation was caused by a number of large intrusions which can be optically identified due to cracking of the oxide scale in their vicinity.

Crystals grown at rates greater than 25.4 cph all had cycle lives much shorter (two to three orders of magnitude) than those discussed above. Failure in all of these specimens was seen to be due to grain boundaries which were not detected in either optical or X-ray examinations. These boundaries were quite extensive, running across the entire specimen and in some instances along the length of the gage section. The fracture surface of specimen UR-11-1 is shown in Fig. 59. The grain boundary nature of this fracture is clearly shown with the gently undulating surface which is not characteristic of crystallographic cleavage.

D. Discussion

The metallographic results presented here illustrate the substantial changes in the as-solidified microstructures that were obtained by varying the growth rate. The effect of decreasing the dendrite spacing with increased cooling rate is well documented. In this case, the thermal gradient, G , is known to be independent of growth rate, R (over the range investigated) such that the cooling rate, \dot{T} normally given by $\dot{T} = GR$ can be considered to be proportional to R : $\dot{T} \propto R$. Since porosity is formed within the interdendritic region during the final stages of solidification, the manner in which the growth rate affects this area is of interest.

Classical solidification theory shows that either of three modes of solidification can be obtained by varying the solidification rate, R , or the temperature gradient, G , as shown in Fig. 60. It can be seen that by holding the temperature gradient constant, any of the three solidification modes can be achieved if the proper growth rate is maintained. The line A-B represents the range of growth rates that were maintained during this study with the slowest rate of 1.27 cph resulting in cellular growth with very little intercellular segregation. As the rate was increased, the solidification interface became more dendritic in nature as shown in Fig. 60.

The primary dendrite spacing also varied with solidification rate. Figure 61 shows this change graphically. The modifications in dendrite arm spacing were not reflected in the cell and subcell sizes detected after homogenization which remained constant in the ranges of 100-300 μm and 10-70 μm , respectively.

In the as-cast condition, the volume fraction of observed porosity and the average pore radius decreased in a log-linear fashion with increasing growth rate with the exception of the $R = 1.27$ cph specimen, which will be discussed later. (The decrease in size of these two features is directly related to the scaling characteristics observed in alloy solidification.) From the linear regions of Figs. 55 and 56, the rate of change of volume fraction and mean radius are given as:

$$\frac{d V_v}{d \ln R} = -0.03$$

$$\frac{d \bar{r}}{d \ln R} = -0.196 \mu\text{m}$$

After homogenization the mean pore radius was found to be independent of growth rate and approximately equal to the pore size for the crystal grown at 1.27 cph. This would indicate that a quasi-equilibrium pore size of radius $\bar{r}_0 \approx 6 \mu\text{m}$ is obtained irregardless of growth rate.

The volume fraction measurements for the homogenized crystals varied and were not conclusive. It appears, however, that the pore volume fraction decreases at low growth rates (i.e., $R < 2.54$ cph) and increases rapidly above 127 cph. This increase in pore volume fraction after homogenization can come only from the coalescence of many small pores. These pores were not observed in the as-cast crystal due to their small size which must have been below the resolution limit of $\sim 2 \mu\text{m}$. The formation of these small pores is the direct consequence of the well-known "scaling laws" associated with dendritic solidification (Ref. 32).

The drop in pore volume fraction both in the as-cast and homogenized crystals is due to the change in solidification mode from dendritic to cellular on decreasing the solidification rate. Porosity forms during the withdrawal process when trapped regions of liquid within the interdendritic areas occur. As these trapped pools solidify and shrink, they can no longer be fed with additional liquid to take up the volume change and a small pore is developed. In cellular growth, little chance is given for pools of trapped liquid to form due to the regular nature of the solid-liquid interface. As the solidification rate is decreased in order to achieve cellular solidification, porosity is eliminated. The same would be true of plane front growth.

It has been shown in Ref. 30 that pore growth occurs during the homogenization process as a consequence of the leveling of chemical gradients which leads to a Kirkendall vacancy generation process. These chemical gradients are also minimized leading to low porosity levels after homogenization as well.

In the above cited reference, where a thermal gradient of $\sim 70^\circ\text{C}/\text{cm}$ was utilized with $R = 30$ cph, a mean pore radius of $8.0 \mu\text{m}$ and a pore volume fraction of 0.082% were obtained. After homogenization, $\bar{r} = 11.84 \mu\text{m}$ and $V_p = 0.213$ were achieved. With reference to the data produced here, the as-cast pore volume fractions were equivalent, while the mean radius was substantially larger for the low gradient crystal. After homogenization, both the mean radius and volume fraction were lower for the crystals grown under the high gradient.

Dendritic structures become finer as the growth rate increases for a given undercooling in the case of an undercooled melt (Ref. 32) and as the cooling rate increases for a situation such as directional solidification (Ref. 33). They are refined in such a manner that their shape remains constant, at least in the case of succinonitrile (a transparent organic material) and in the case of face-centered-cubic materials such as the nickel-base superalloys. These circumstances fall under what have been termed the "scaling laws" of dendritic solidification. The mathematical relationships between the secondary arm spacing and solidification variables such as local undercooling or local solidification time (inversely related to cooling rate) have been well established. There are several experimental measurements which confirm the theoretical models. The theoretical and experimental situation relative to primary dendrite spacing is not as well established. Nonetheless, it can be stated that the primary spacing also decreases as the cooling rate increases for the case of directional solidification, although with a slightly different power law (Ref. 31).

In addition to dendrites, it has been observed that other microstructural features become finer as the growth rate increases. In the case of superalloys it is clear that the carbide features become finer along with the dendrites at higher cooling rates (proportional to the growth rate at constant thermal gradient). In addition, in alloys where any eutectic is present in the microstructure, this feature also scales up and down along with the dendrites (Ref. 32). Finally, based on detailed analyses of porosity in this and related work, it is clear that microporosity which is due to isolation of liquid pools between dendrite arms and subsequent shrinkage and void formation due to the volume change upon solidification (as opposed to gas porosity which is generally not a problem in directionally cast superalloys) scales with the dendritic features. The carbides, eutectic pools and shrinkage pores all form in association with the partitioning and microsegregation patterns which are typical of dendritic growth. It is therefore logical that all of these features should scale together.

It becomes clear from Table V that the upper limit for growing these crystals in the gradient used here is between 25 and 125 cph. In this range high angle boundaries emerge which are very deleterious to the fatigue as well as the creep properties. The presence of these boundaries reduces the fatigue lives by 2 to 4 orders of magnitude. Thus the presence of these boundaries must be avoided.

A very pronounced subgrain structure was revealed in Fig. 57 where it was noted that two distinct subgrain types were noted. These subgrains did not appear to change in size with differing growth rates, thus it is difficult to explain the manner in which grain boundaries were formed in the fatigue specimens. These defects went undetected despite both optical (macro-etched) and single point Laue X-ray analysis.

For those specimens grown at the slower rates, porosity is still the dominant fatigue failure initiation site. By changing the crystal growth rates, the size and volume fraction of the pores present was affected, but porosity could not be totally eliminated in any instances. Since the theoretical stress concentration factor for any spherical void is independent of its radius, all pores are equally likely to initiate fatigue cracks. In order to increase the fatigue lives of these crystals, one must remove porosity totally. The crystal grown at 2.54 cph was shown to contain a very low volume fraction of porosity and the inference is made above that by obtaining plane front solidification, pore free crystals can be obtained. The fatigue data would indicate that absolute pore free crystals need to be produced in order that enhanced fatigue life can be realized. Practically speaking, this can only be achieved through

R86-916534-3

hot isostatic pressing, HIP, which will eliminate all nonsurface connected pores if the correct procedures are used. This process has been shown to enhance the fatigue lives of cast equiaxed superalloys by a factor of 3 to 10 times (Refs. 34,35).

V. PUBLICATIONS

Previous Publications

"Rhenium Effect on Creep Behavior of Ni-Base Superalloys", L. S. Lin, A. F. Giamei and R. E. Doiron: 38th Ann. Proc. EMSA, 1980, pp 330-331.

"Rhenium Additions to a Ni-Base Superalloy: Effects on Microstructure", A. F. Giamei and D. L. Anton: Met. Trans., 16A, 1985, pp 1997-2005.

"Workability of High Strength Superalloys", A. F. Giamei, D. L. Anton and R. E. Doiron: in Super Plastic Forming of Structural Alloys, N. E. Paton and C. H. Hamilton eds., TMS-AIME, Warrendale, PA, 1982, pp 225-239.

"Porosity Distribution and Growth During Homogenization in Single Crystals of a Nickel-Base Superalloy", D. L. Anton and A. F. Giamei: Mat. Sci. & Eng., 76, 1985, pp 173-180.

"Effects of Rapid Solidification on Nickel Alloy Properties: A Review", A. F. Giamei and J. Larson: Mechanical Behavior of Rapidly Solidified Materials, S. M. L. Sastry and B. A. MacDonald, eds., TMS-AIME, Warrendale, PA, 1986, pp 103-117.

"On the Role of Molybdenum in Rapidly Solidified Ni-Base Alloys", A. F. Giamei: Rapidly Solidified Crystalline Alloys, S. K. Das, B. H. Kear and C. M. Adam, eds., TMS-AIME, Warrendale, PA, 1985, pp 203-217.

" γ / γ' : The Key to Superalloy Behavior", A. F. Giamei, D. D. Pearson and D. L. Anton: Mat. Res. Soc. Symp. Proc., V. 39, Pittsburgh, PA, 1985.

In Preparation for Publication

"Rhenium Additions to a Ni-Base Superalloy: Mechanical Properties", A. F. Giamei and D. L. Anton: Met. Trans.

"Plastic Strain Localization In Superalloys", D. L. Anton and A. F. Giamei: Acta Met.

"The Effects of Single Crystal Growth Rates on Porosity in Superalloys", D. L. Anton and A. F. Giamei: Mat. Sci. & Eng.

VI. REFERENCES

1. Stoltz, R. and A. Pineau: *Mat. Sci. Eng.*, 34, 275 (1978).
2. Kear, B. H. and B. J. Pearcey: *Trans. TMS-AIME*, 239, 1209 (1967).
3. Leverant, G. R. and B. H. Kear: *Met. Trans.*, 1, 491 (1970).
4. Gell, M. and G. R. Leverant: *Trans. TMS-AIME*, 242, 1869 (1968).
5. Merrick, H. F.: *Met. Trans.*, 5, 891 (1974).
6. Beardmore, P., R. G. Davies and T. L. Johnston: *Trans. TMS-AIME*, 245, 1537 (1969).
7. Abel, A. and R. K. Ham: *Acta Met.*, 14, 1493 (1966).
8. Bhat, S. P. and C. Laird: *Acta Met.*, 27 (1973).
9. Wilhelm, M., M. Nageswararao and R. Meyer: Fatigue Mechanisms, J. Fong ed., ASTM STP 675, p 214 (1979).
10. Laird, C., V. J. Langelo, M. Holbsak, N. C. Yang and R. de la Veaux: *Mater. Sci.*, 32, 137 (1978).
11. Vogel, W., M. Wilhelm and V. Gerold: *Proc. 5th Int. Conf. on the Strength of Metals and Alloys*, P. Hassen et al. eds., Achen, W. Germany, p 1175 (1979).
12. Pearson, D. D., B. H. Kear and F. D. Lemkey: Creep and Fracture of Engineering Materials, B. Wilshire and D. R. Owen, eds., Pineridge Press, Swansea, U.K., p 213 (1981).
13. Mackin, I. L. and O. D. Kancheev: *Met. Sci. and Heat Treat.*, Nos. 1&2, (1967).
14. Carry, C. and J. L. Strudel, *Acta Met.*, 25, 767 (1977).
15. McEvily, A. J., J. B. Clark, E. C. Utley and W. H. Hernstein: *Trans. TMS-AIME*, 221, 1093 (1963).
16. Clark, J. B. and A. J. McEvily: *Acta Met.*, 12, 1359 (1964).
17. Krause, A. R. and Laird: *Mater. Sci. Eng.*, 2, 331 (1967).
18. Wells, C. H. and C. P. Sullivan: *Trans. TMS-AIME*, 57, 841 (1964).
19. Gleiter, H. and E. Hornbogen: *Mater. Sci. Eng.*, 2, 285 (1967/68).

20. Anton, D. L. and M. E. Fine: *Mater. Sci. Eng.*, 58, 135 (1983).
21. Leverant, G. R. and B. H. Kear: *Met. Trans.*, 1, 491 (1970).
22. Gell, M. and G. R. Leverant: Fatigue at Elevated Temperatures, ASTM-STP 520, A. E. Carden et al. eds., p 37 (1972).
23. Gell, M. and G. R. Leverant: Fracture 1969, P. L. Pratt et al. eds., Chapman and Hall, London, U.K., p 565 (1969).
24. Leverant, G. R. and M. Gell: *Trans. TMS-AIME*, 245, 1167 (1969).
25. Gell, M., D. N. Duhi and A. F. Giamei: Superalloys 1980, ASM, Metals Park, OH (1980).
26. Harris, K., G. L. Erickson and R. E. Schever: Cannon-Muskegon Corp., Muskegon, MI, unpublished research, 1982.
27. Anton, D. L.: *Acta Met.*, 32, 1669 (1984).
28. Khan, T., P. Caron and T. G. Nakagawa: *J. Metal.*, 38, 16 (1986).
29. Sullivan, C. P., A. F. Giamei and F. L. VerSnyder: *Fifth Int. Conf. on Electroslag and Other Special Melting Tech.*, ASM, Metals Park, OH (1974).
30. Anton, D. L. and A. F. Giamei: *Mater. Sci. Eng.*, 76, 173 (1985).
31. Giamei, A. F. and F. L. VerSnyder: Grain Boundaries in Engineering Materials, J. L. Walter et al. eds., Claitor's Pub., Baton Rouge, LA (1975).
32. Glicksman, M. E. and P. W. Voorhees: *Met. Trans.*, 15A, 955 (1984).
33. Kattamis, T. Z., J. C. Coughlin and M. C. Flemings: *Trans. TMS-AIME*, 239, 1504 (1967).
34. Schneider, K., G. Gnirb and G. McColvin: High Temperature Alloys for Gas Turbines 1982, R. Brunestand et al. eds., Reidel Publ. Co., London, U.K., p 319 (1982).
35. Anton, D. L. and L. F. Favrow: Low Cycle Fatigue; Trends for the Future, ASTM-STP, in press, 1986.

Table I
Summary of Surface Slip Equations

| <u>Eqn. No.</u> | <u>Equation</u> | <u>Description</u> | <u>Resolution Required</u> |
|-----------------|---|-----------------------|----------------------------|
| 1 | $b = \bar{\alpha}_0 + \bar{\beta}_0 + \bar{\gamma}_0$ | for dislocations | $\sim 10^{-10}$ m |
| 2 | $\bar{B} = \bar{\alpha} + \bar{\beta} + \bar{\gamma}$ | for slip lines | $\sim 10^{-8}$ m |
| 3 | $\bar{\epsilon} = \sum_z B(z)$ | for slip bands | $\sim 10^{-6}$ m |
| 5 | $X = \sum_z \bar{\epsilon}(z)$ | for macro deformation | $\sim 10^{-4}$ m |

Table II
Single Crystal Alloy Chemistries

| <u>Alloy</u> | <u>Chemistry (a/o)</u> |
|--------------|---|
| U-700 | 15.55Cr, 16.92Co, 2.92Mo, 8.59Al, 3.94Ti, 3.59C, 0.15B, bal. Ni |
| 143 | 9.00Mo, 2.00Ta, 13.00Al, bal. Ni |
| 143-L | 9.00Mo, 1.67Ta, 10.86Al, bal. Ni |

Table III

Homogenization Heat Treatment Schedules
for Three Single Crystal Alloys

| | | |
|-------|-----|---|
| U-700 | SOL | 1050°C/4 hr/AC + 1150°C/24 hr/AC |
| | SHT | 1000°C/8 hr/AC |
| 143 | SOL | 1093°C/4 hr/AC + 1204°C/4 hr/AC + 1315°C/24 hr/AC |
| | SHT | 1080°C/4 hr/AC + 870°C/24 hr/AC |
| 143L | SOL | 1215°C/24 hr/AC |
| | SHT | 1080°C/4 hr/AC + 870°C/24 hr/AC |

Note: AC = air cooled
SOL = solution heat treatment
STD = standard heat treatment

Table IV
Quantitative Metallographic Data on Porosity in Cast and Homogenized S/C 143

| Spec. | As-Cast | | | | | Homogenized | | | | | | |
|-------|----------------------------|----------------------------|-----------|----------------|----------|-------------|----------------|-----------|----------------|----------|------|----------------|
| | $\overline{R}(\text{cph})$ | $\overline{R}(\text{iph})$ | $V_v(\%)$ | \overline{L} | σ | N | \overline{r} | $V_v(\%)$ | \overline{L} | σ | N | \overline{r} |
| UR-14 | 1.27 | 0.5 | 0.049 | 8.422 | 7.412 | 1012 | 6.32±0.70 | 0.024 | 6.728 | 6.325 | 436 | 5.05±0.91 |
| UR-6 | 2.54 | 1.0 | 0.174 | 7.203 | 5.364 | 1387 | 5.40±0.43 | 0.068 | 9.669 | 3.531 | 1142 | 7.25±0.31 |
| UR-7 | 12.7 | 5.0 | 0.134 | 7.427 | 4.450 | 1948 | 5.57±0.30 | 0.039 | 7.960 | 4.766 | 784 | 5.97±0.51 |
| UR-9 | 25.4 | 10.0 | 0.036 | 8.263 | 5.966 | 738 | 6.20±0.66 | 0.167 | 8.354 | 5.967 | 2710 | 6.27±0.34 |
| UR-11 | 127.0 | 50.0 | 0.068 | 5.015 | 2.571 | 5743 | 3.76±0.10 | 0.087 | 9.324 | 8.739 | 832 | 6.99±0.91 |
| UR-13 | 254.0 | 100.0 | 0.029 | 5.768 | 3.159 | 1807 | 4.33±0.22 | 0.346 | 8.105 | 5.616 | 512 | 6.08±0.74 |

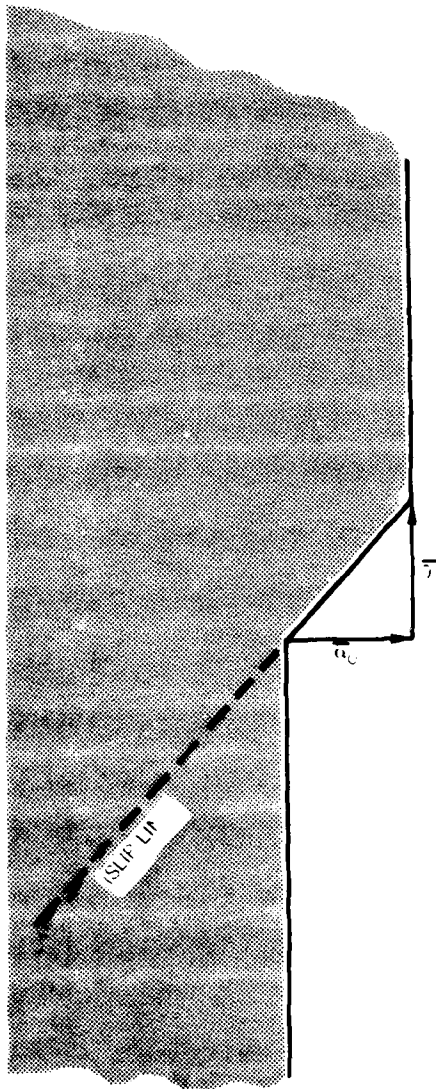
Table V

Fatigue Testing Results for Single Crystal Alloy
143 Grown at Various Rates

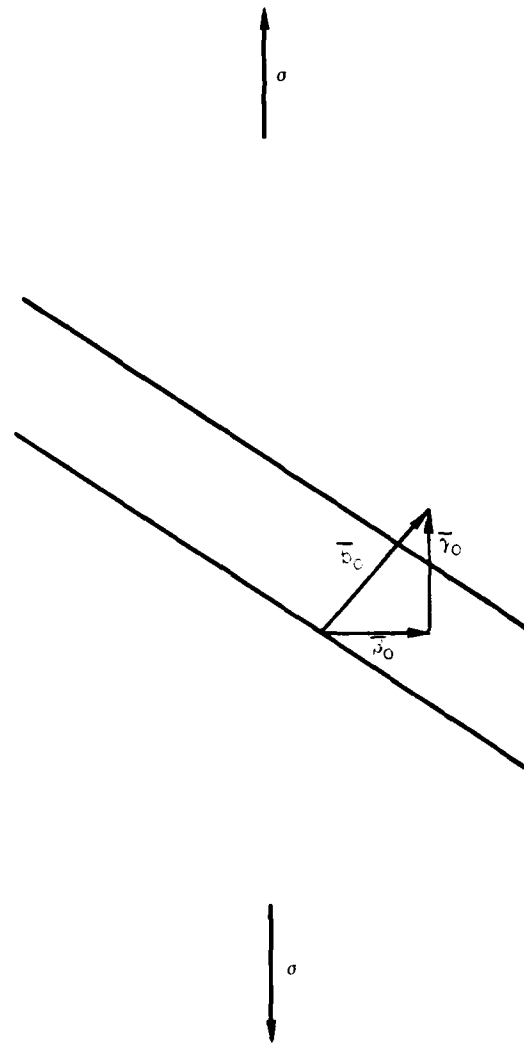
T = 871°C (1600°F)
Max. Stress ≈ 700 MPa
R = 0.1

| <u>Spec. No.</u> | <u>R (cph)</u> | <u>N</u> | <u>Initiation Site</u> |
|------------------|----------------|-----------|------------------------|
| UR-6-2 | 2.54 | 1.98 x 10 | pore |
| UR-7-1 | 12.7 | 1.20 x 10 | pore |
| UR-7-2 | | 7.30 x 10 | pore |
| UR-9-1 | 25.4 | 1.40 x 10 | surface |
| UR-9-2 | | 1.40 x 10 | pore |
| UR-11-1 | 127 | 5.10 x 10 | grain boundary |
| UR-11-2 | | 5.00 x 10 | grain boundary |
| UR-13-1 | 254 | 5.28 x 10 | grain boundary |
| UR-13-2 | | 4.50 x 10 | grain boundary |

SLIP TRACE AT SPECIMEN SURFACE AFTER PASSAGE OF ONE DISLOCATION SHOWING ORIENTATION OF VECTORS α_0 , β_0 AND γ_0 WITH SLIP VECTOR b_0



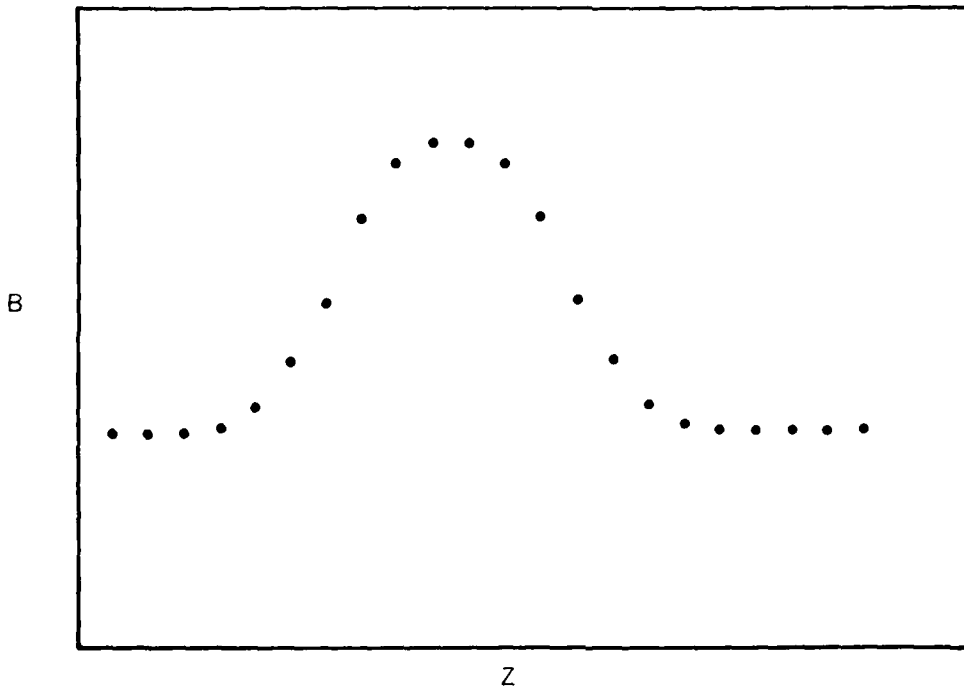
(a) SIDE VIEW OF SLIP BAND



(b) FRONT VIEW OF SLIP BAND

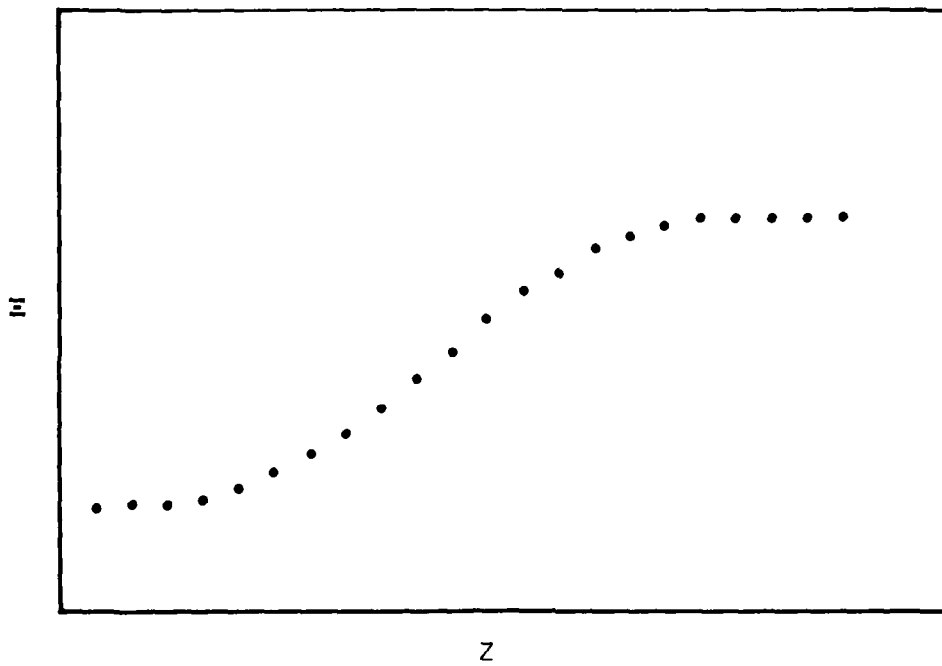
DEGREE OF SLIP IN A SLIP BAND ALONG THE STRESS AXIS

FIG. 2

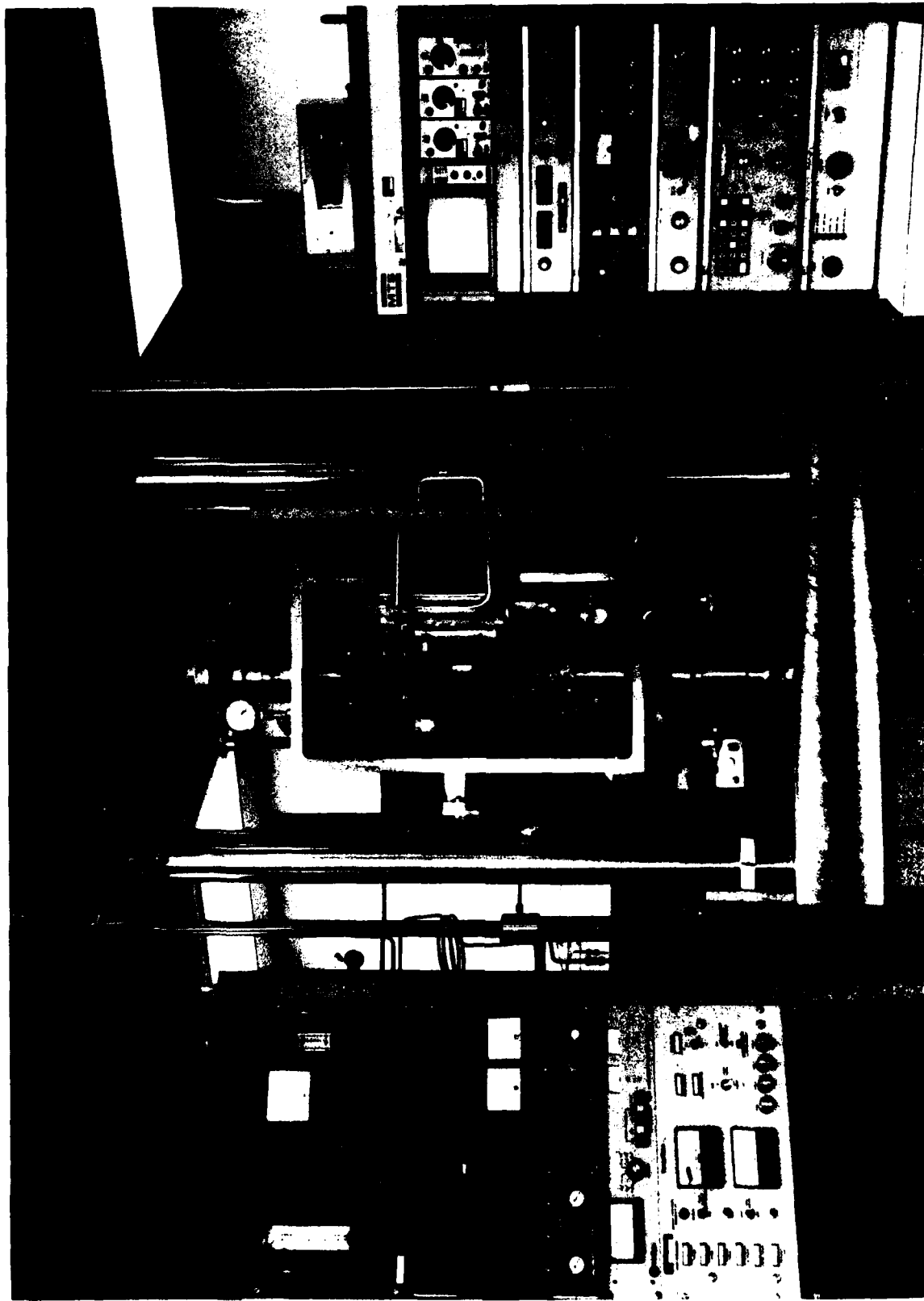


SUMMATION OF SLIP IN THE SLIP BAND DEPICTED IN FIG. 2

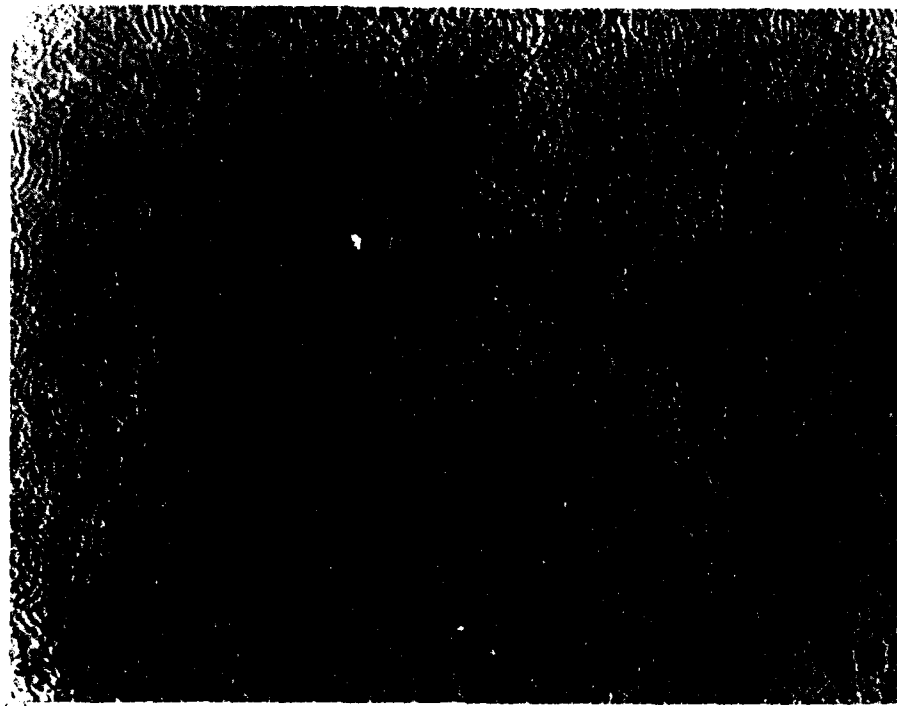
FIG. 3



SERVO HYDRAULIC TEST SYSTEM WITH VACUUM CHAMBER OPEN

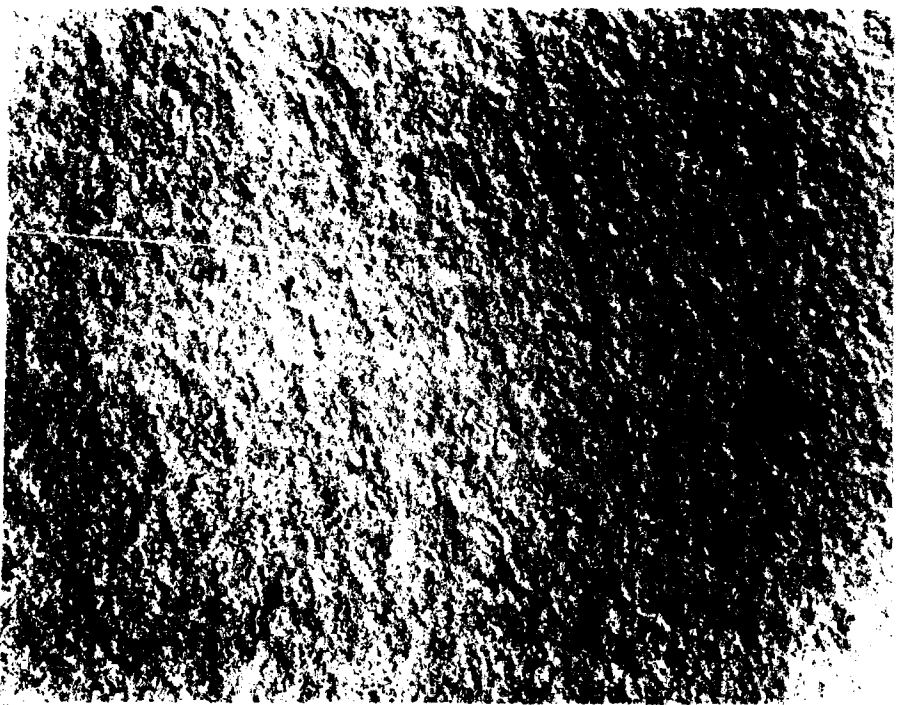


REPLICAS OF ELECTROPOLISHED 143 SURFACE TOPOLOGY BEFORE TESTING



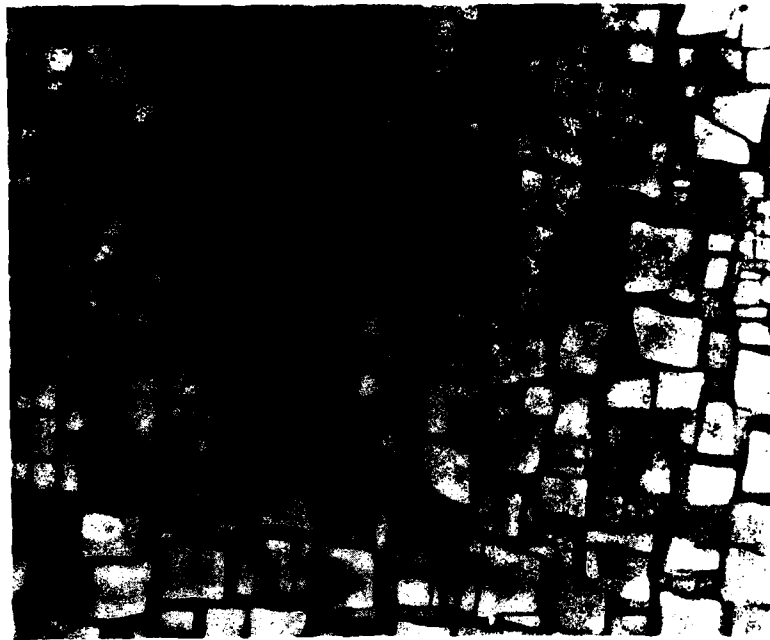
(a)

42 μ m



(b)

TEM THIN FOIL MICROGRAPHS OF SOLUTIONED AND AGED MICROSTRUCTURES
BEFORE DEFORMATION



(a) SOL

0.5 μ m



(b) SHT

OPTICAL MICROGRAPH OF SOL [011] 143 REPLICA AFTER COMPRESSIVE PLASTIC STRAIN OF 0.25%

STRESS AXIS
↕



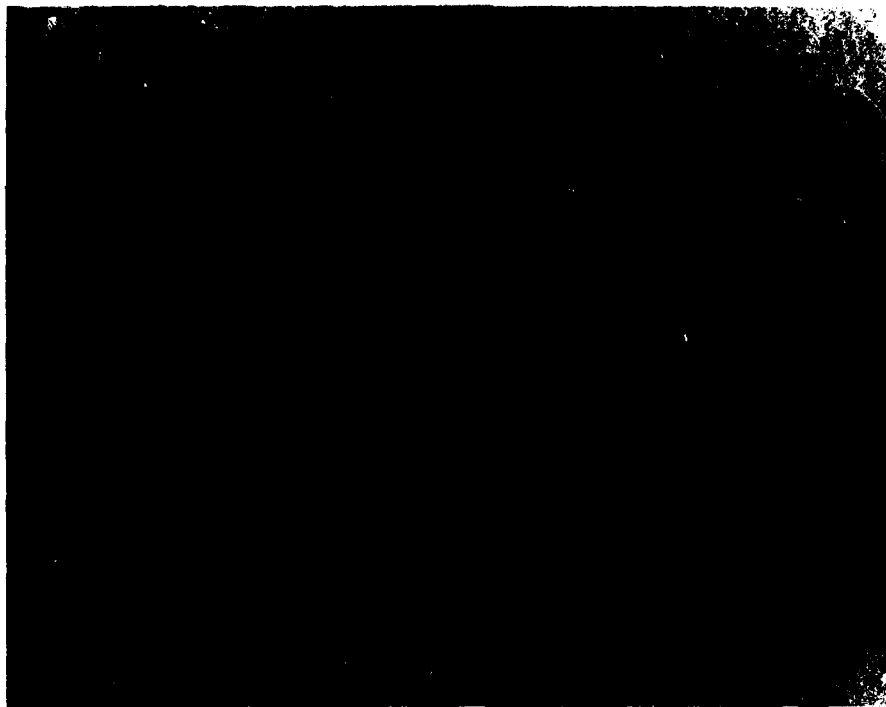
(a) {100} SURFACE

50μm



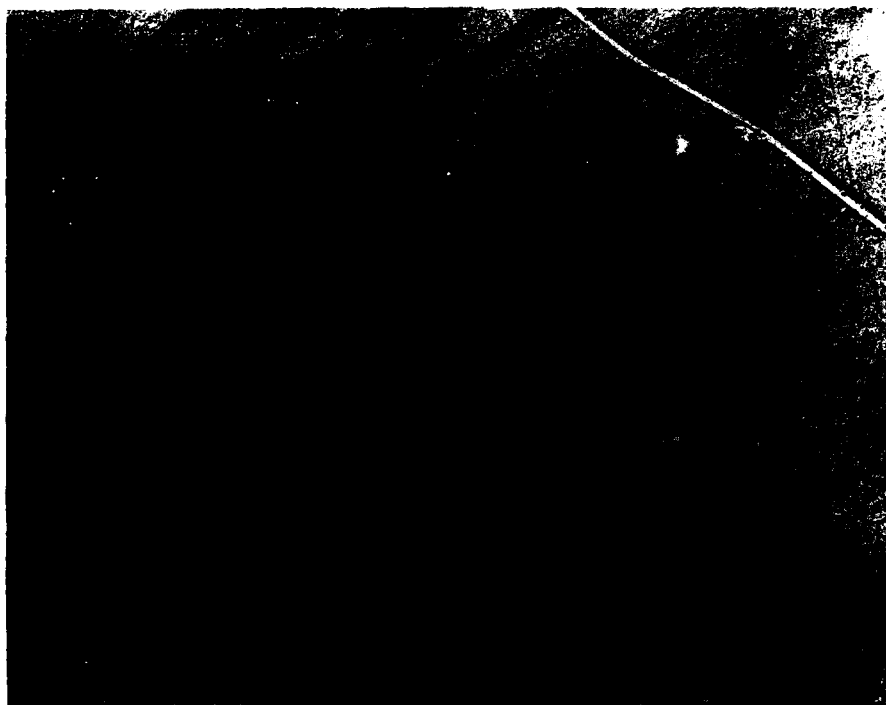
(b) {110} SURFACE

TEM MICROGRAPHS OF SOL [011] 143 REPLICA AFTER COMPRESSIVE PLASTIC STRAIN OF 0.25%



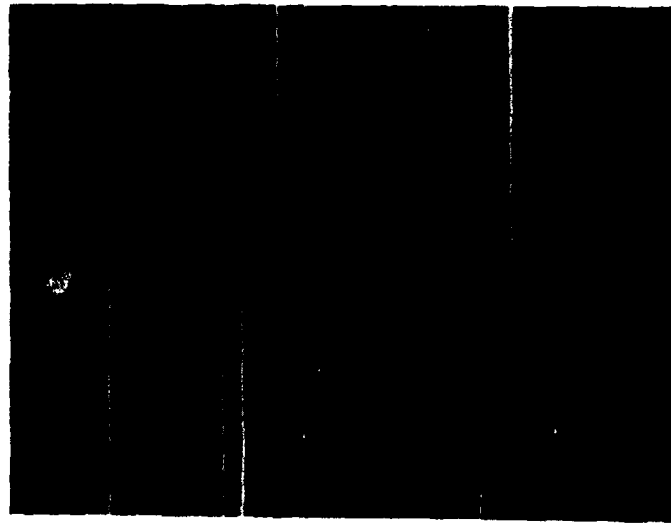
(a) {100} SURFACE

1.85μm



(b) {110} SURFACE

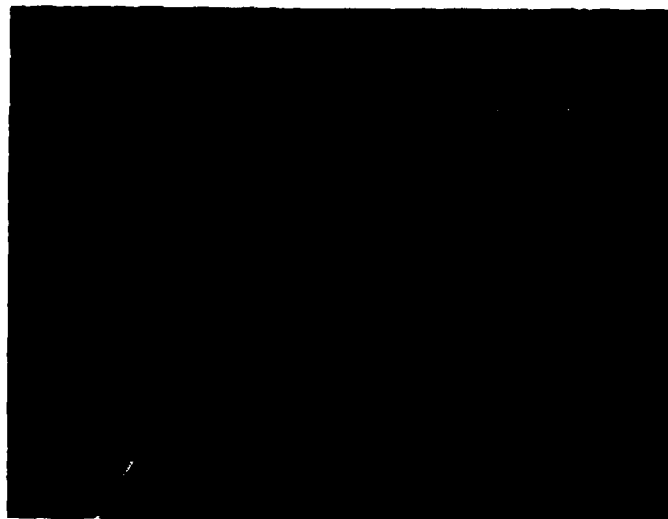
OPTICAL MICROGRAPHS OF SOL [011] 143 REPLICA AFTER COMPRESSIVE PLASTIC STRAIN OF 0.5%



(a) {100} SURFACE

STRESS
←→
AXIS

50μm

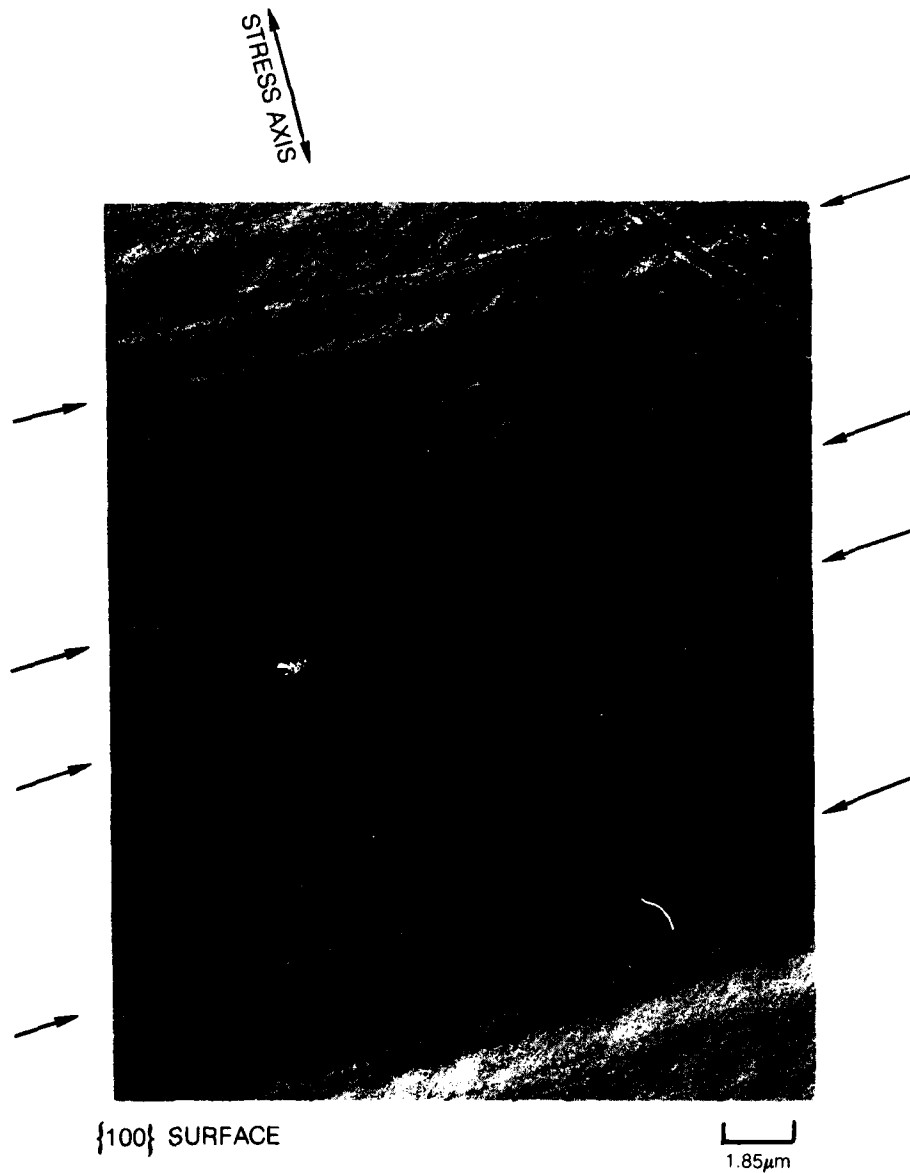


(b) {110} SURFACE

TEM MICROGRAPH OF SOL [011] 143 REPLICA AFTER COMPRESSIVE PLASTIC STRAIN OF 0.5%

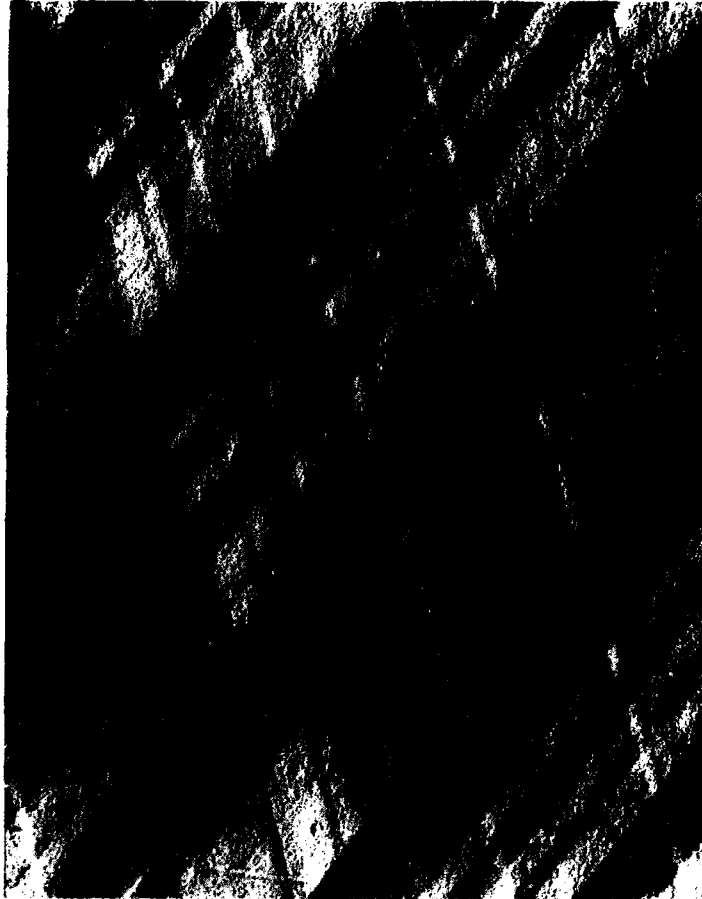


TEM MICROGRAPH OF SOL [011] 143 REPLICA AFTER COMPRESSION PLASTIC STRAIN OF 1%



TEM MICROGRAPH OF SOL [011] 143 REPLICA AFTER COMPRESSIVE PLASTIC STRAIN OF 2%

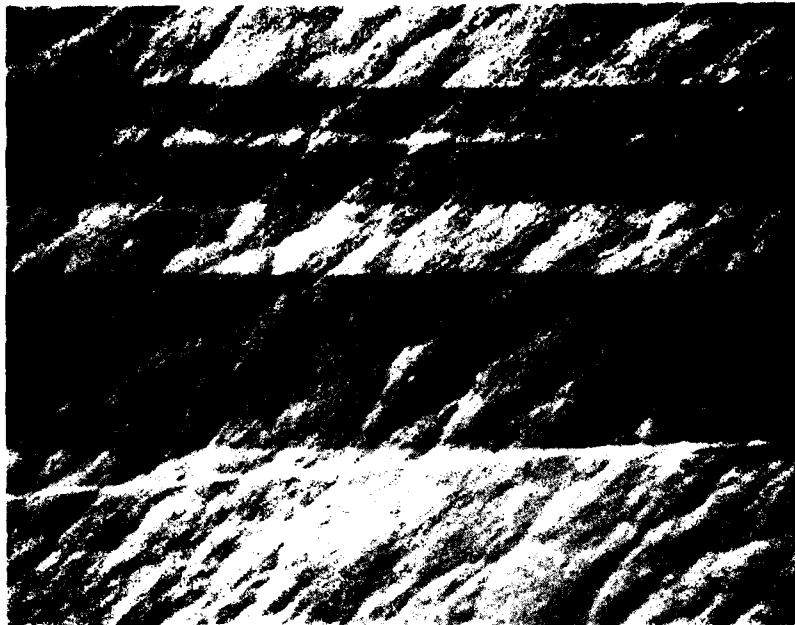
← STRESS AXIS →



{110} SURFACE

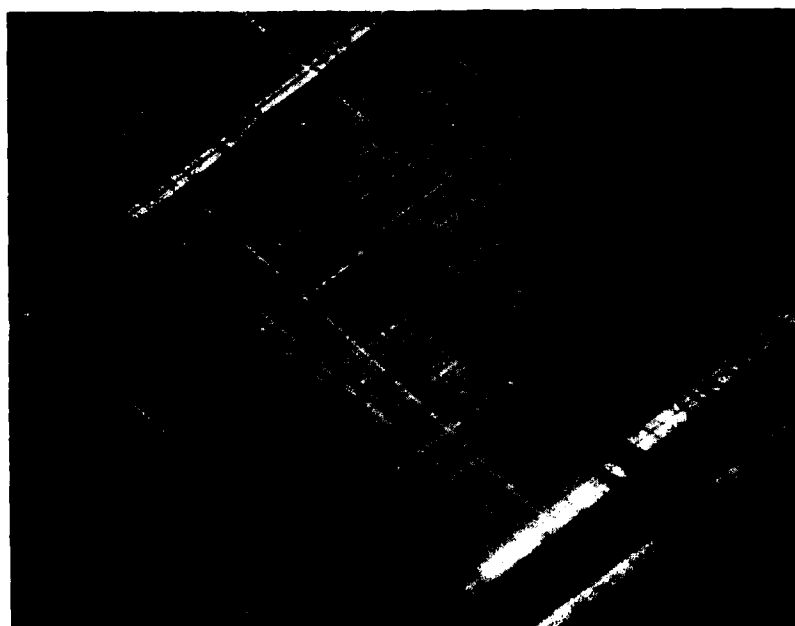
1.85μm

**SEM MICROGRAPH OF SOL [011] 143 ELECTROPLATED SURFACES AFTER
COMPRESSIVE PLASTIC STRAIN OF 5%**



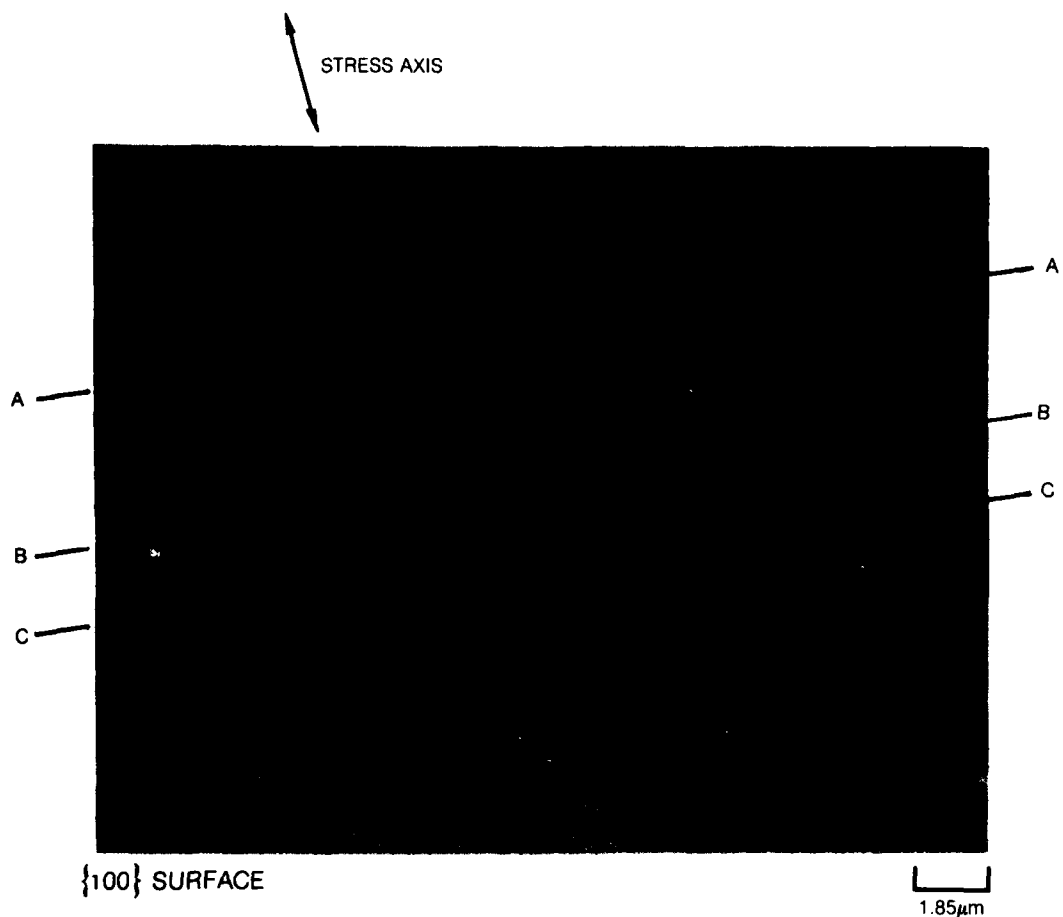
(a) $\{100\}$ SURFACE

5 μ m

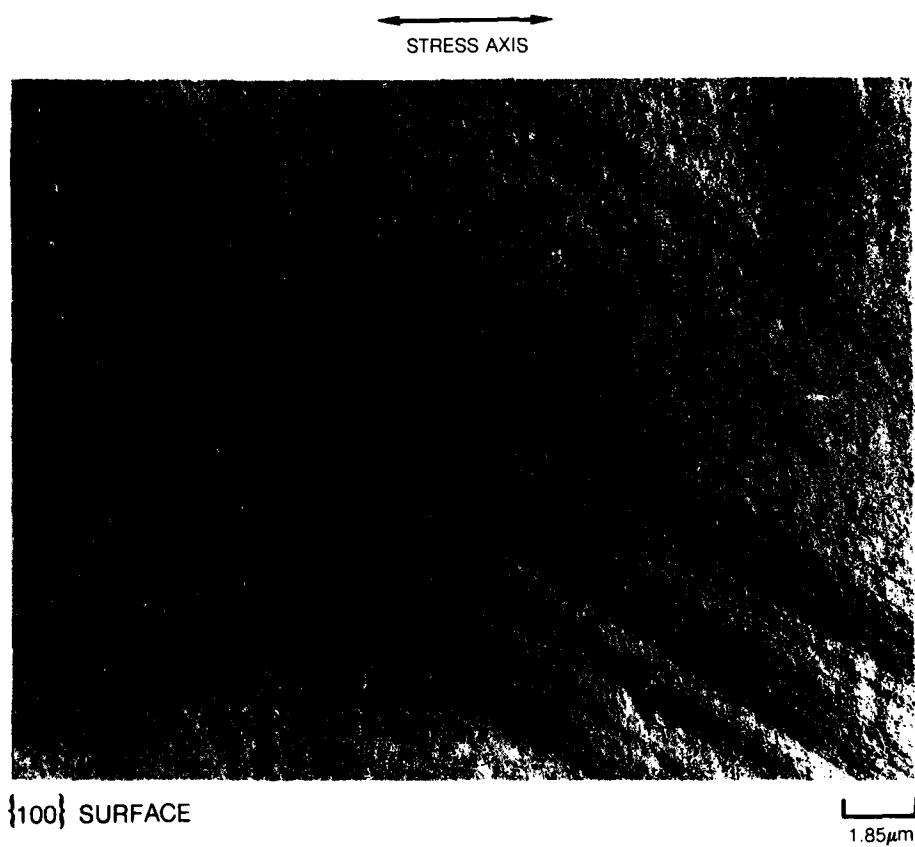


(b) $\{110\}$ SURFACE

TEM MICROGRAPH OF SHT [011] 143 REPLICA AFTER COMPRESSIVE PLASTIC STRAIN OF 0.75%



TEM MICROGRAPH OF SOL [001] 143 REPLICA AFTER COMPRESSIVE PLASTIC STRAIN OF 0.75%



TEM MICROGRAPH OF SOL [011] 143 REPLICA AFTER COMPRESSIVE PLASTIC STRAIN OF 5%

↑
↓
STRESS AXIS



{100} SURFACE

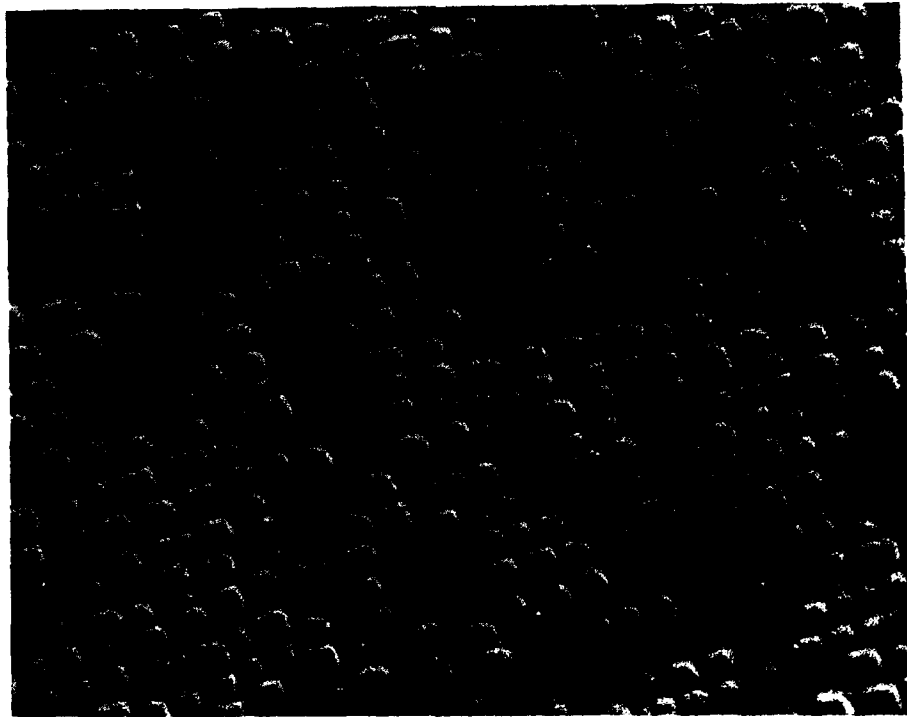
┌───┐
0.04μm

TEM MICROGRAPH OF SHT [001] THIN FOIL AFTER COMPRESSIVE PLASTIC STRAIN OF 5%

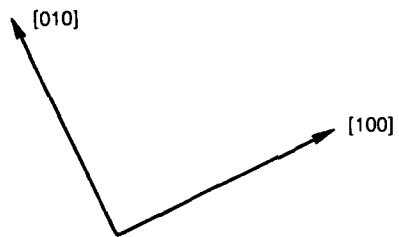


0.02 μ m

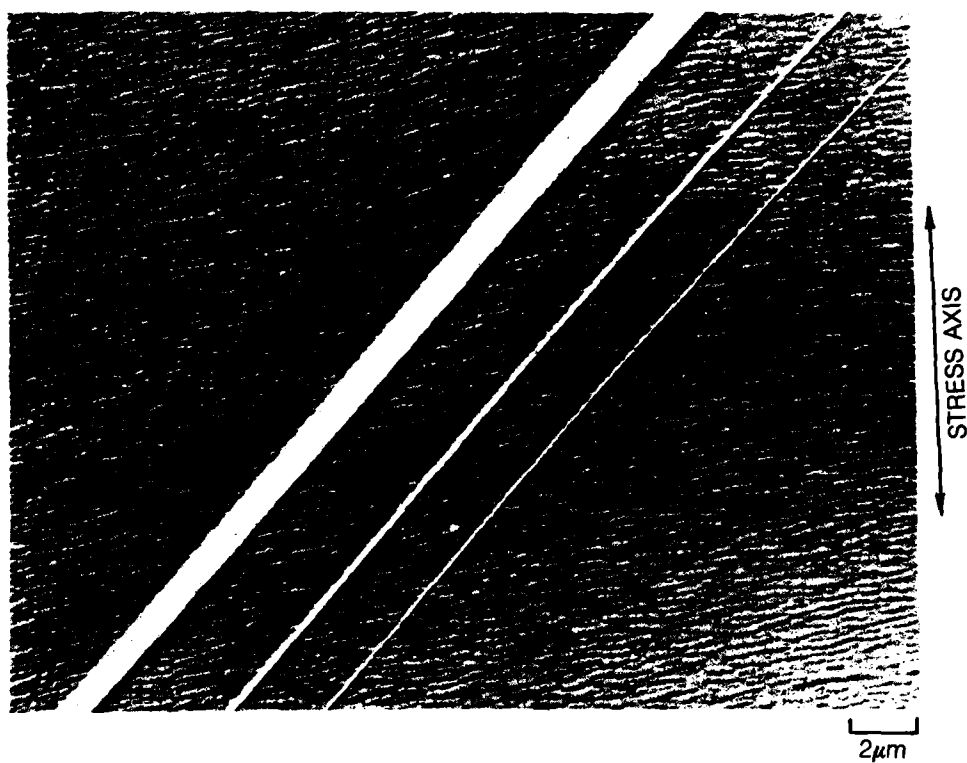
REPLICA OF UNDEFORMED U-700



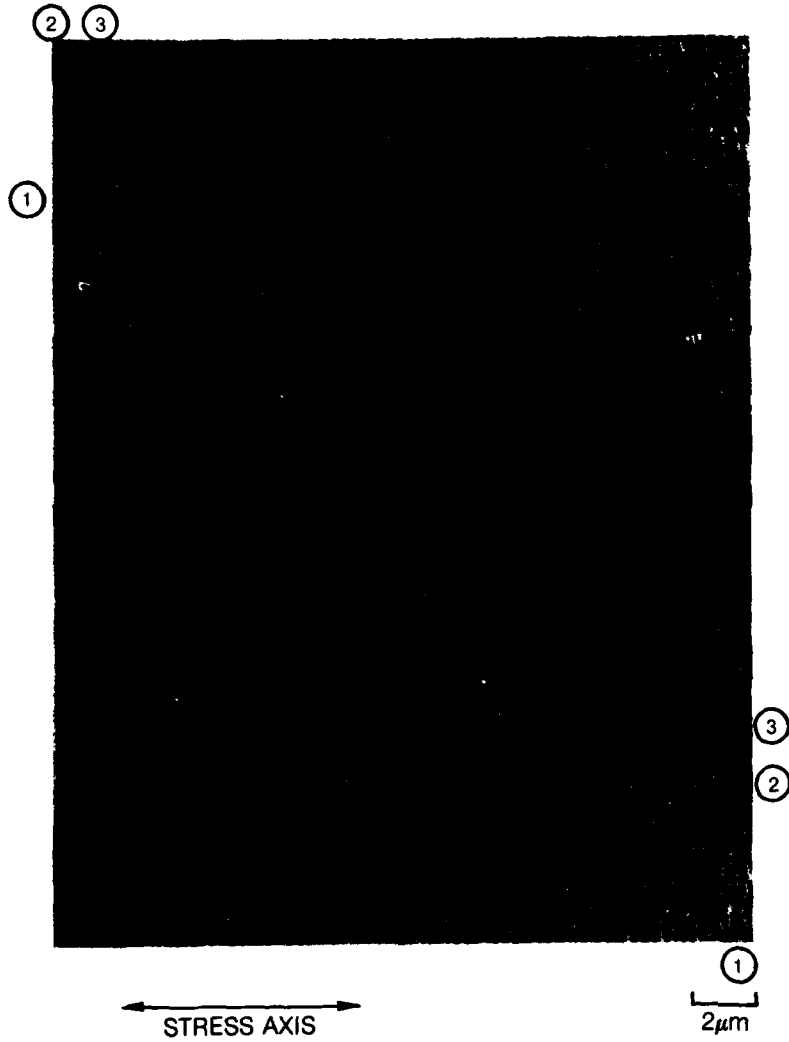
0.5μm



**SURFACE REPLICA OF U-700 COMPRESSION SPECIMEN AFTER $\epsilon_p = 0.25\%$
REVEALING TEARING AT SURFACE SLIP OFFSETS**

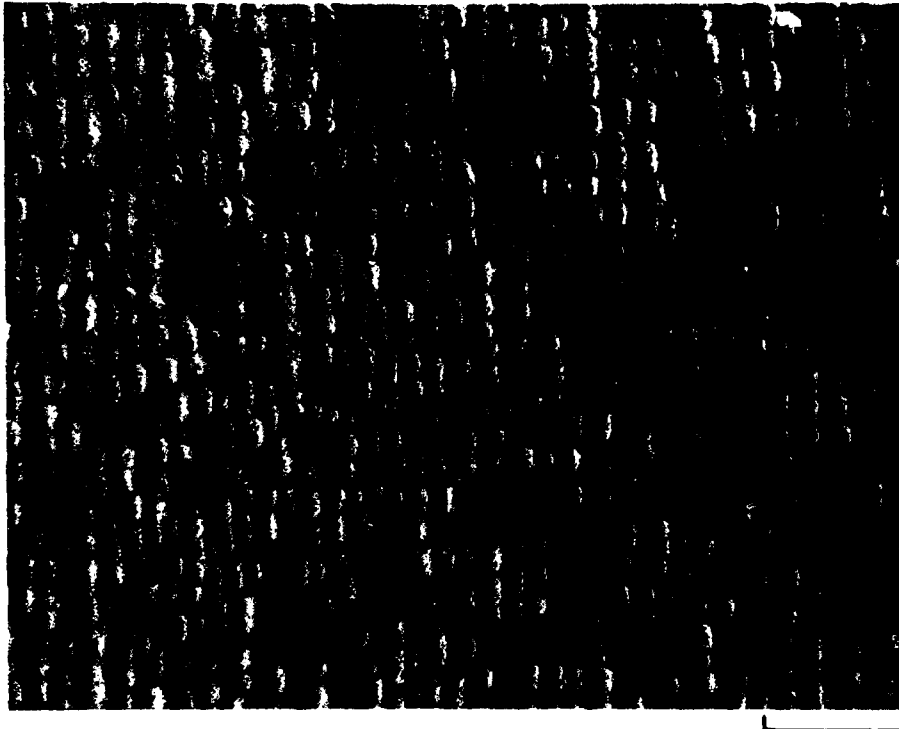


SURFACE REPLICA OF U-700 COMPRESSION SPECIMEN AFTER $\epsilon_p = 0.5\%$

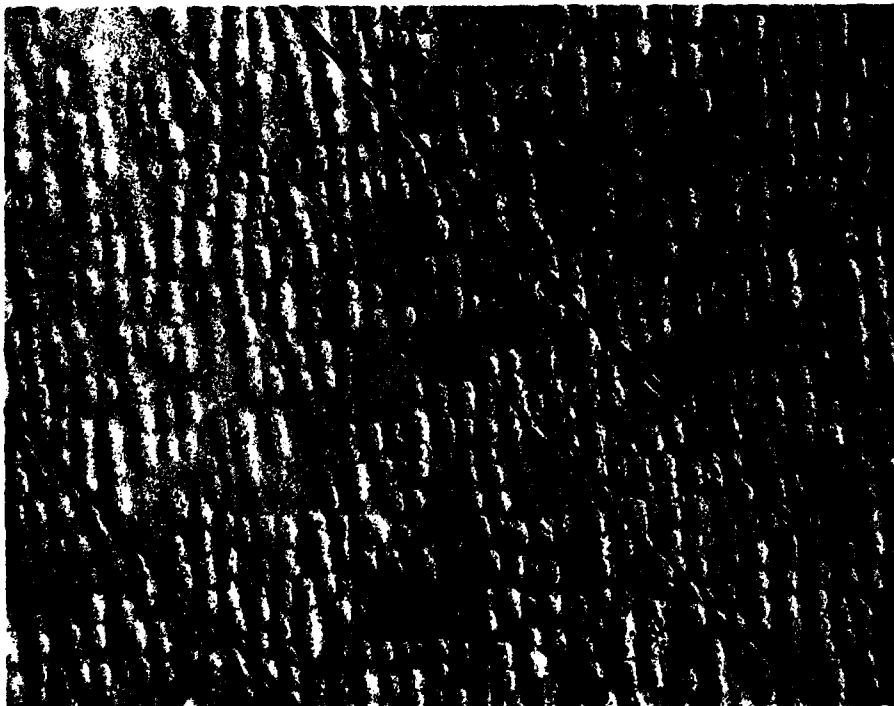


SURFACE REPLICAS OF U-700 COMPRESSION SPECIMEN AFTER $\epsilon_p = 0.5\%$

(a) MAGNIFIED PORTION OF SLIP LINE 1, FIG. 20

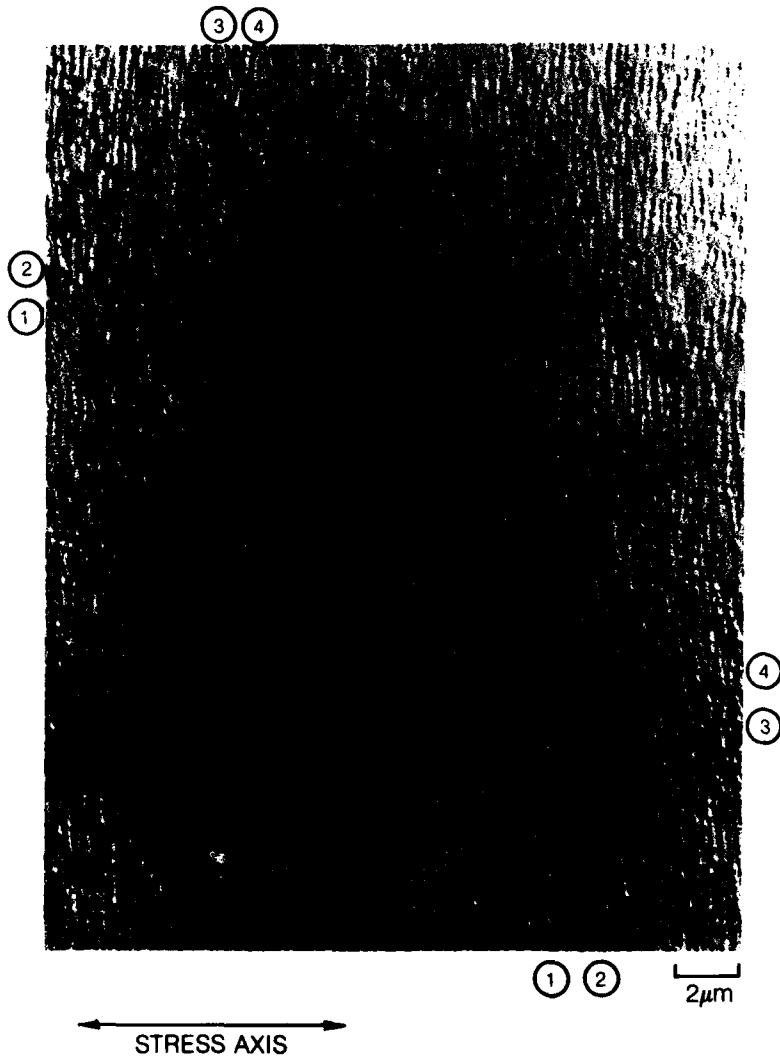


(b) MAGNIFIED PORTION OF SLIP LINES 2 AND 3, FIG. 20

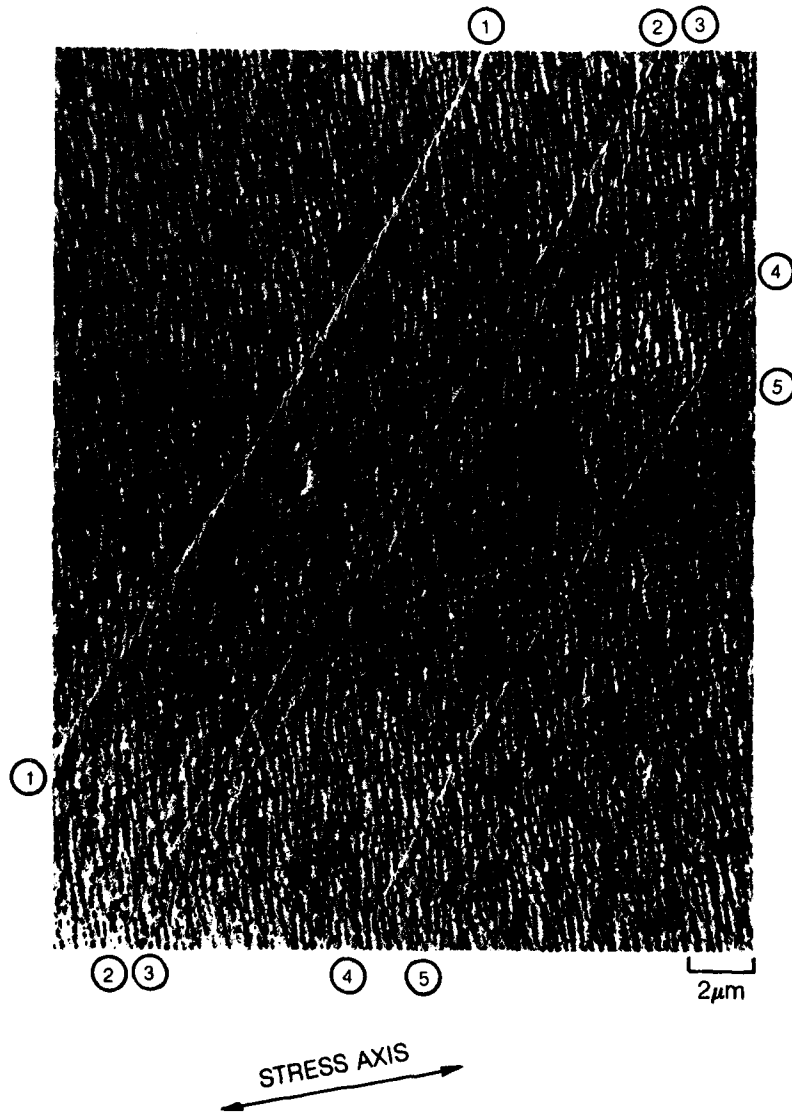


←→
STRESS AXIS

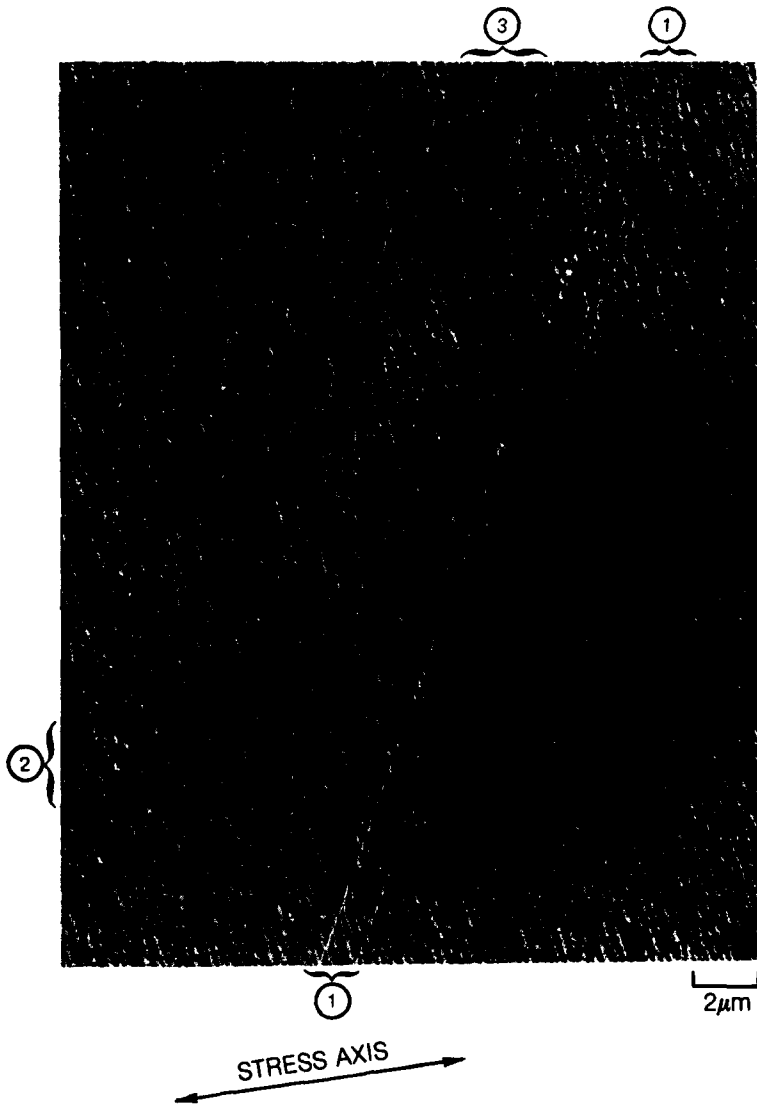
SURFACE REPLICA OF U-700 AFTER $\epsilon_p = 0.75\%$ REVEALING SPREADING OF PLANAR SLIP



SURFACE REPLICA OF U-700 AFTER $\epsilon_p = 1.0\%$



SURFACE REPLICAS OF U-700 AFTER $\epsilon_p = 1.5\%$ SHOWING MULTIPLE CROSS-SLIP EVENTS BETWEEN TWO ACTIVE SLIP PLANES

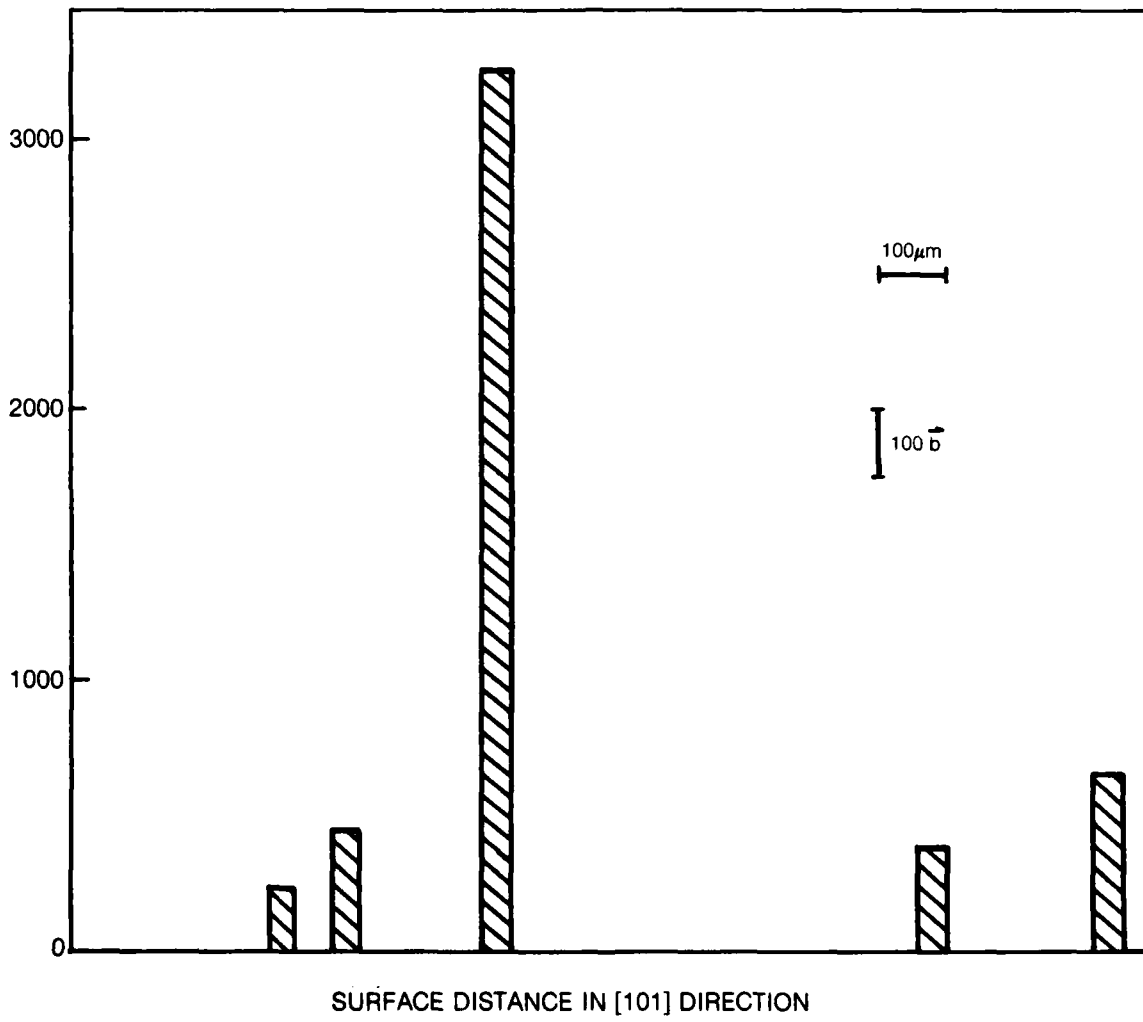


SURFACE REPLICAS OF U-700 AFTER $\epsilon_p = 1.5\%$ MAGNIFIED VIEW OF SLIP BANDS IN FIG. 7

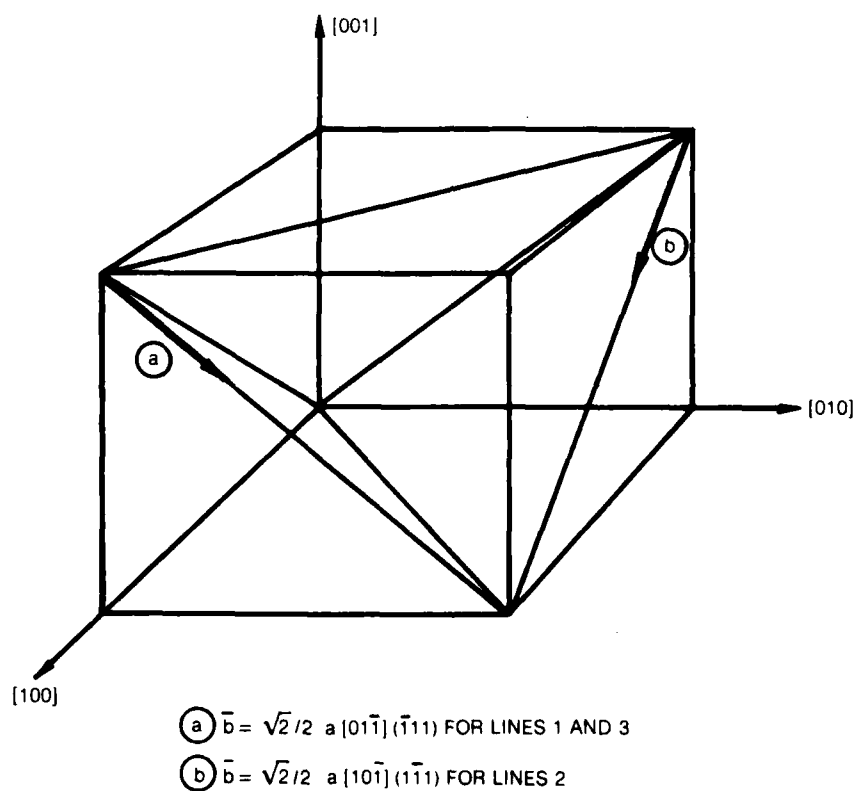


0.8 μ m

LOCAL STRAIN MAP OF SLIP DEPICTED IN FIG. 8 SHOWING MAGNITUDE IN BURGERS VECTORS VERSUS DISTANCE

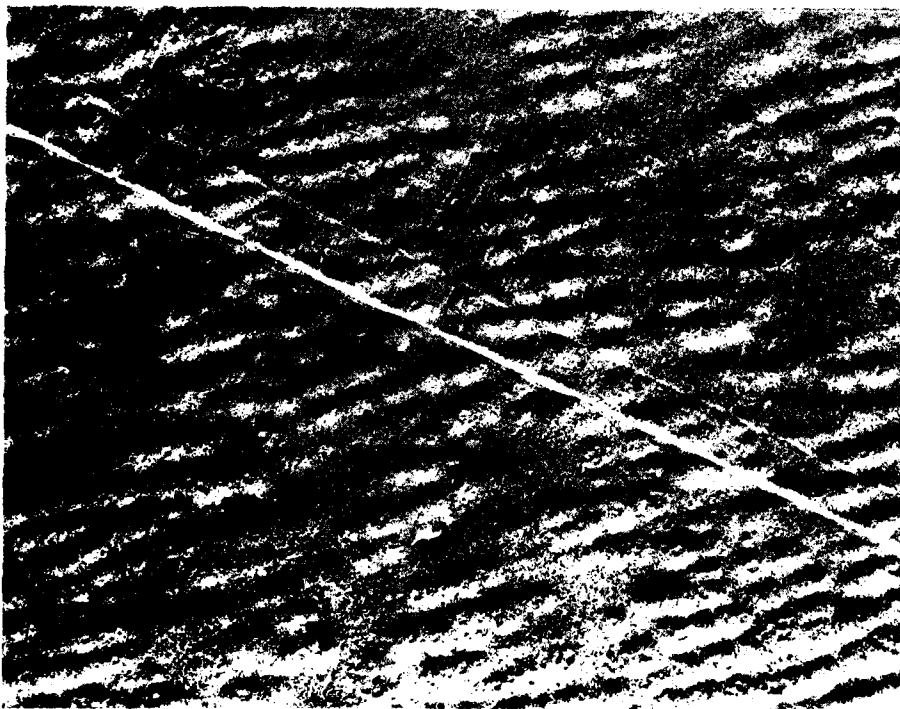


REPRESENTATION OF ACTIVE BURGER'S VECTORS FOR SLIP AND CROSS SLIP
SHOWN IN FIG. 24

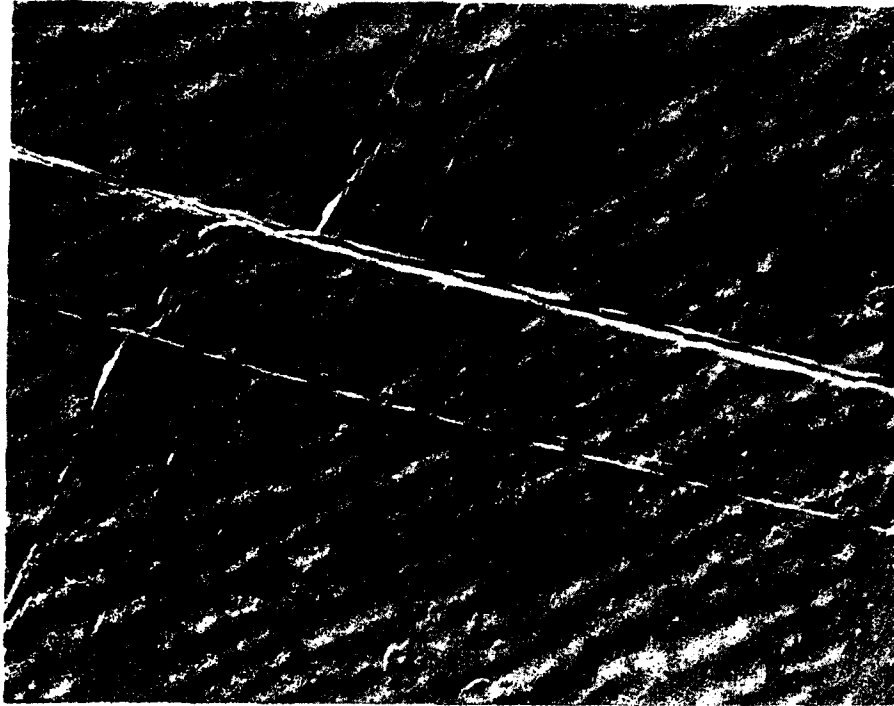


SURFACE REPLICA OF U-700 COMPRESSION SPECIMEN AFTER $\epsilon_p = 1.5\%$

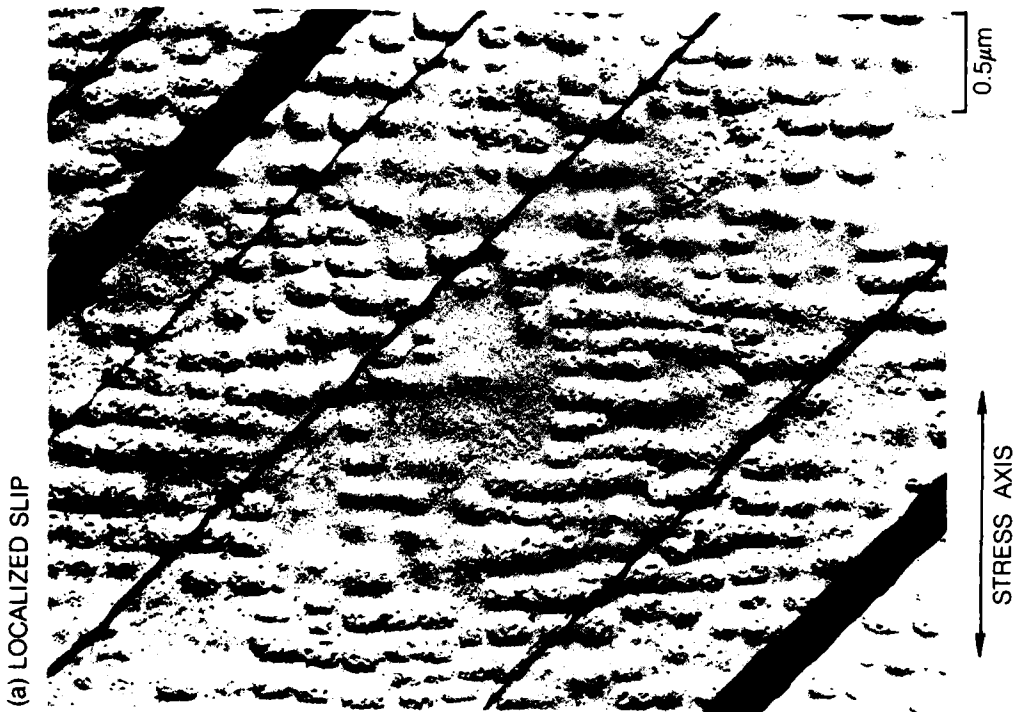
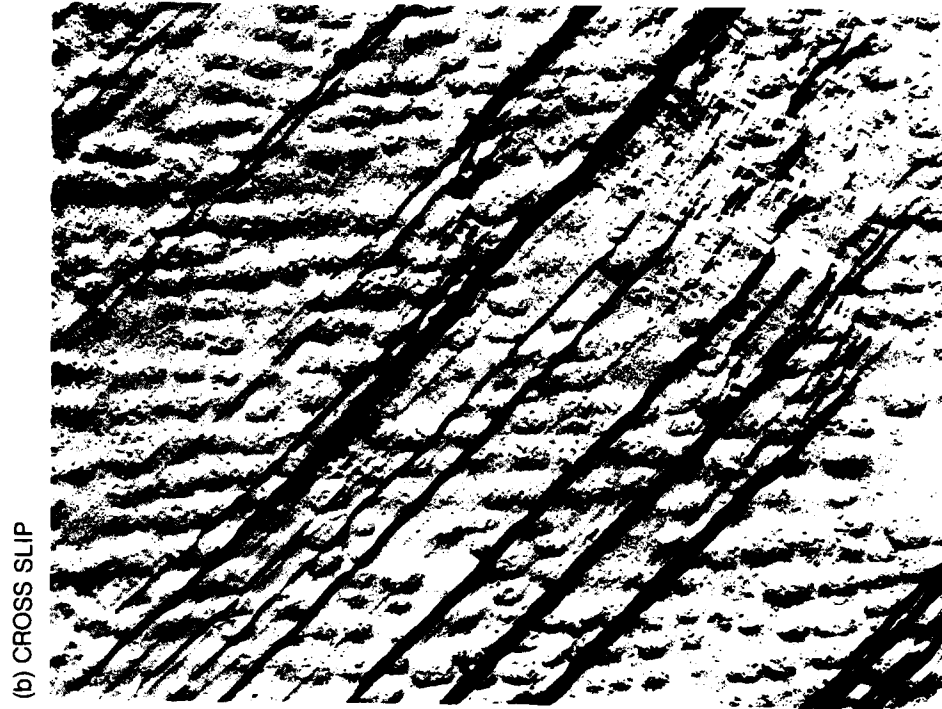
(a) CROSS SLIP



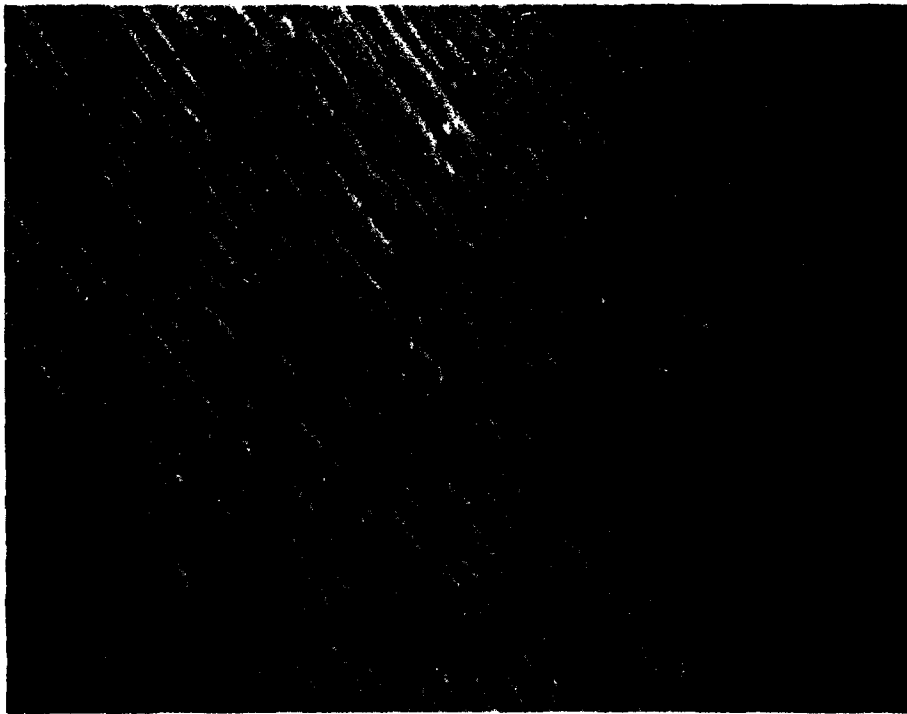
(b) DUPLEX SLIP



SURFACE REPLICA OF U-700 COMPRESSION SPECIMEN AFTER $\epsilon_p = 2.5\%$

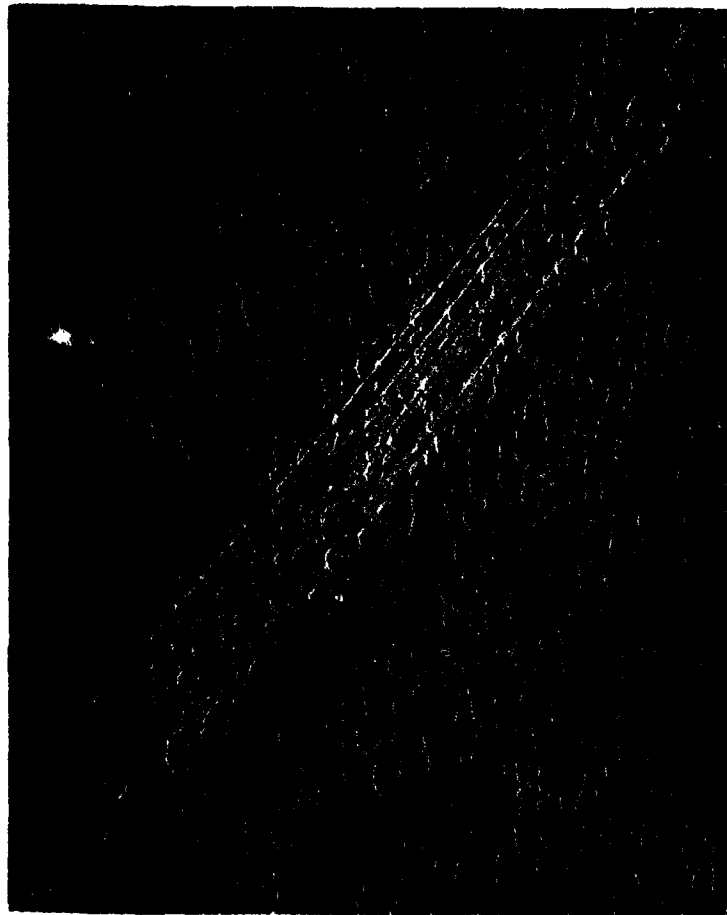


SURFACE REPLICA OF 143L PRIOR TO DEFORMATION



┌
└ 1.85μm

SURFACE REPLICA OF 143L AT 0.25% PLASTIC COMPRESSIVE STRAIN



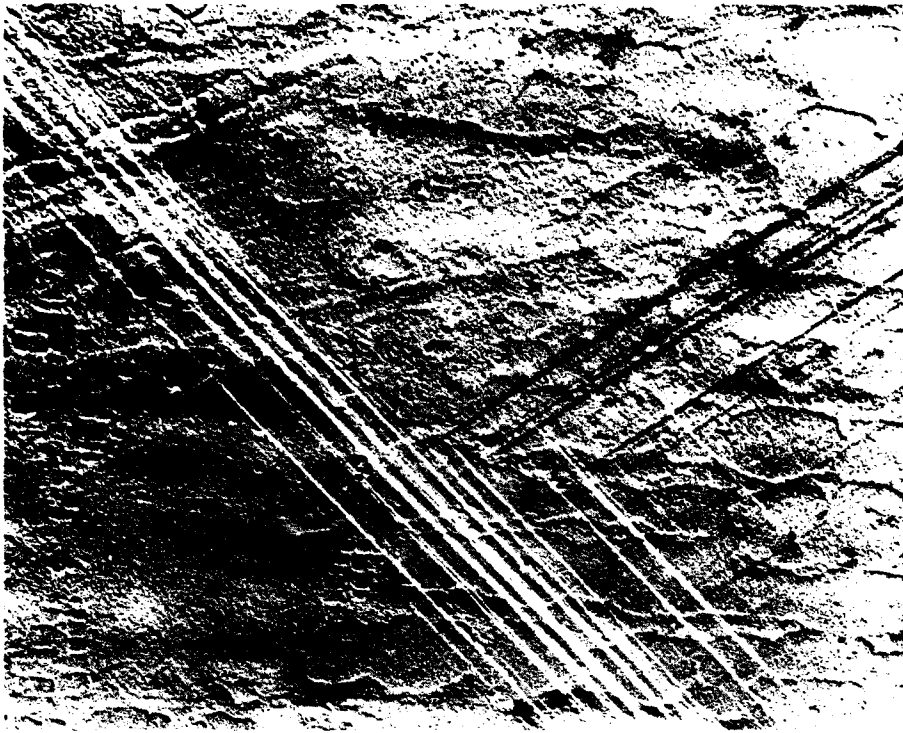
1.5 μ m

SURFACE REPLICA OF 143L AT 0.5% PLASTIC COMPRESSIVE STRAIN

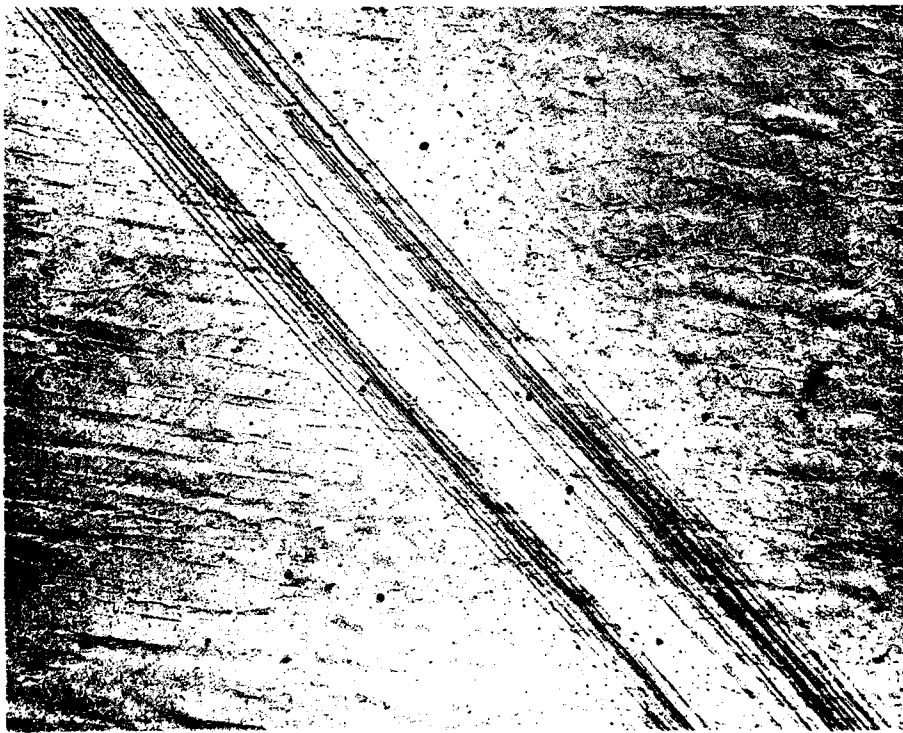


1.5 μ m

SURFACE REPLICA OF 143L AT 1.5% PLASTIC COMPRESSIVE STRAIN

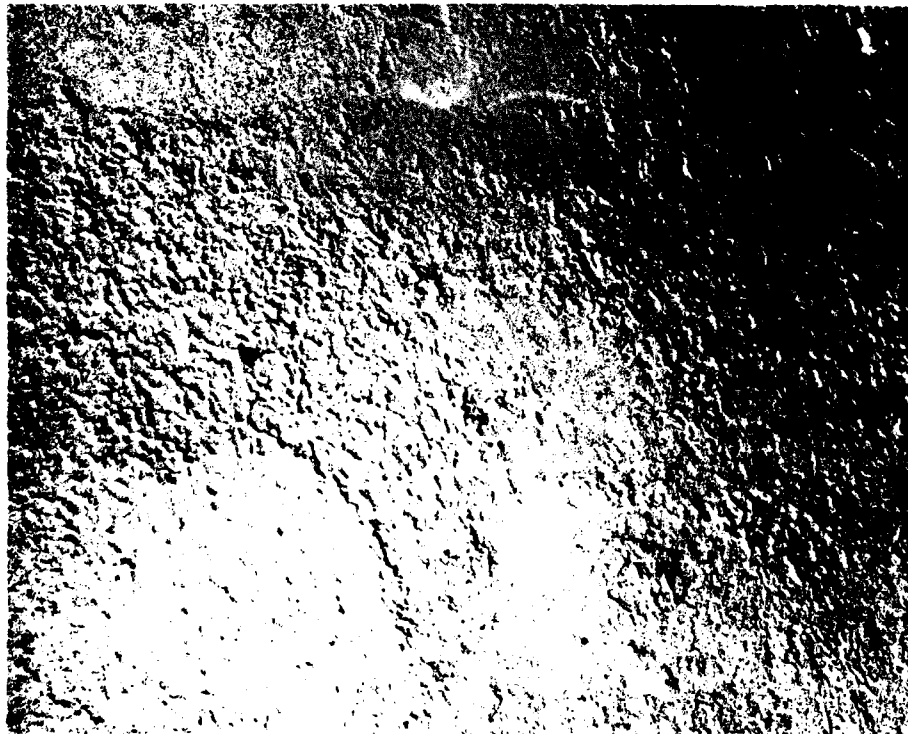


(b)

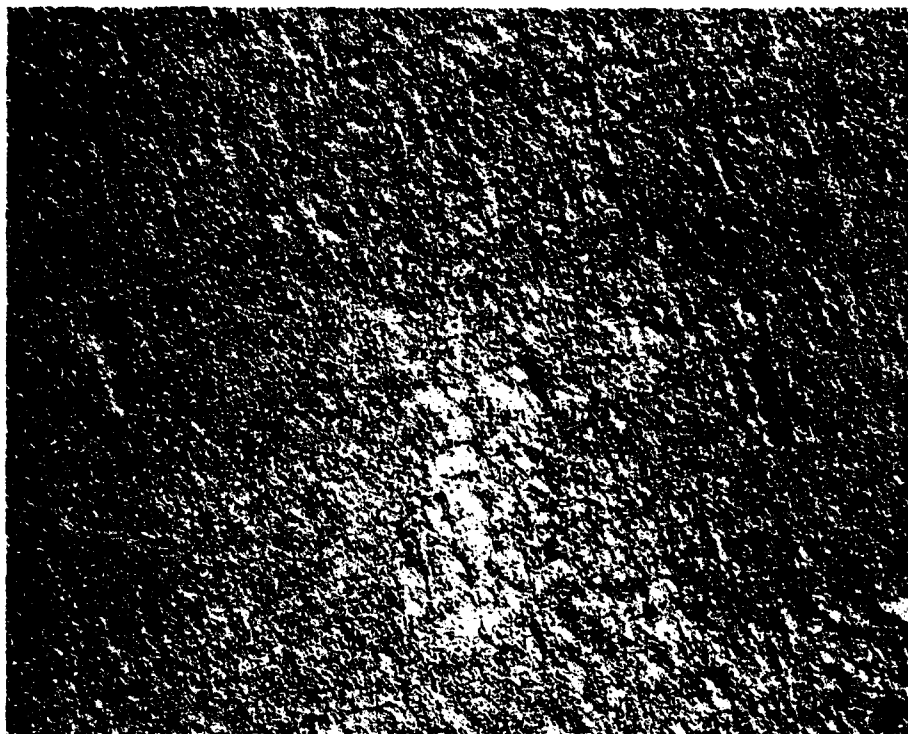


(a)

SURFACE REPLICA OF 143L AT 5% PLASTIC COMPRESSION STRAIN AT 871°C

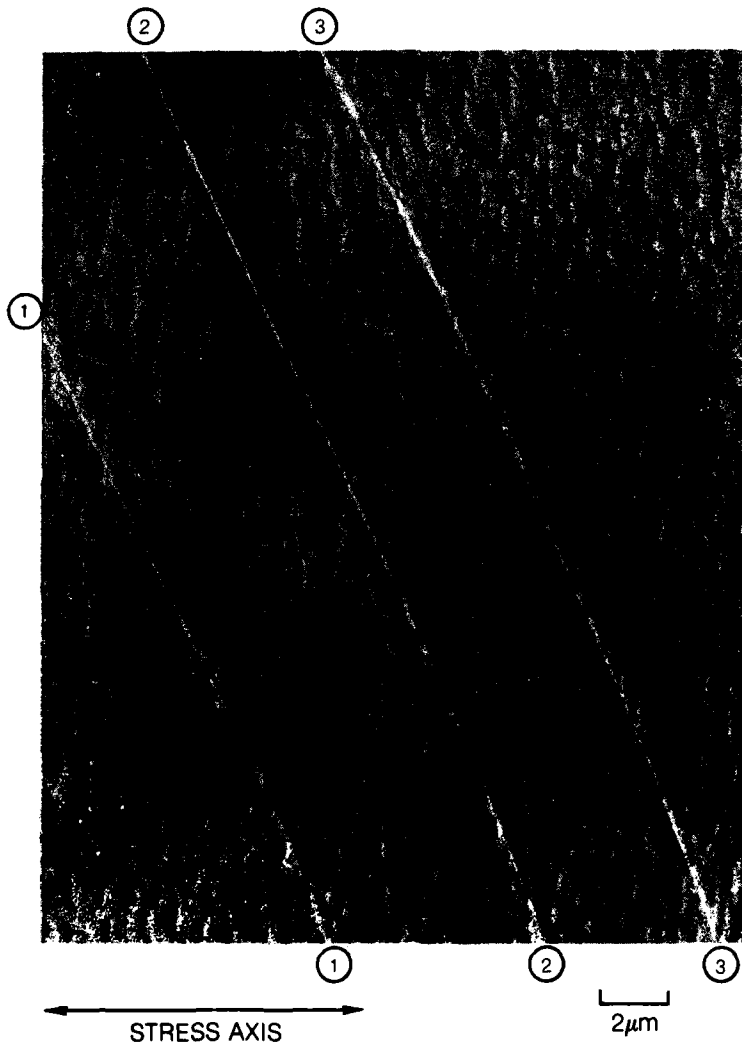


(a)

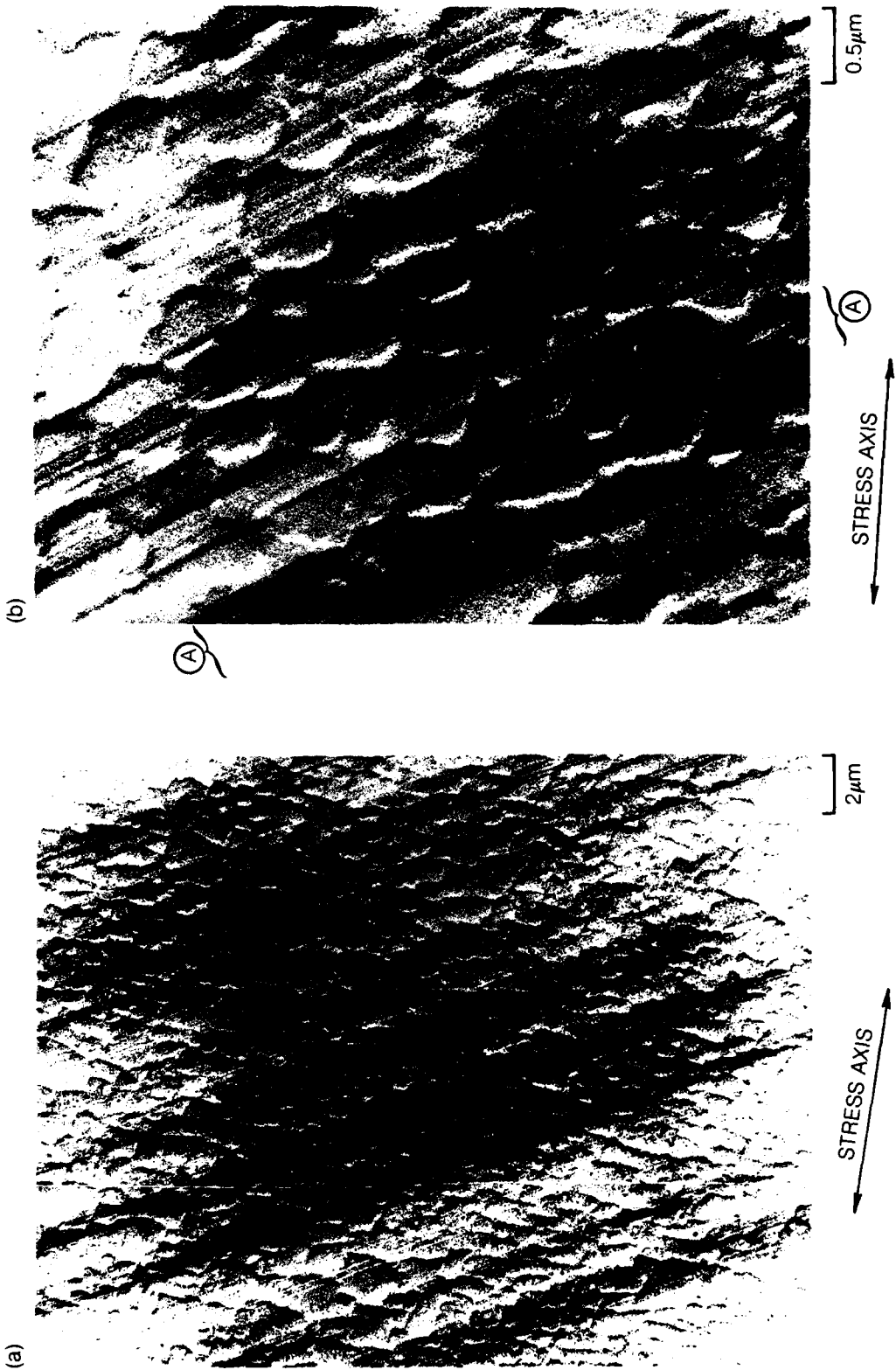


(b)

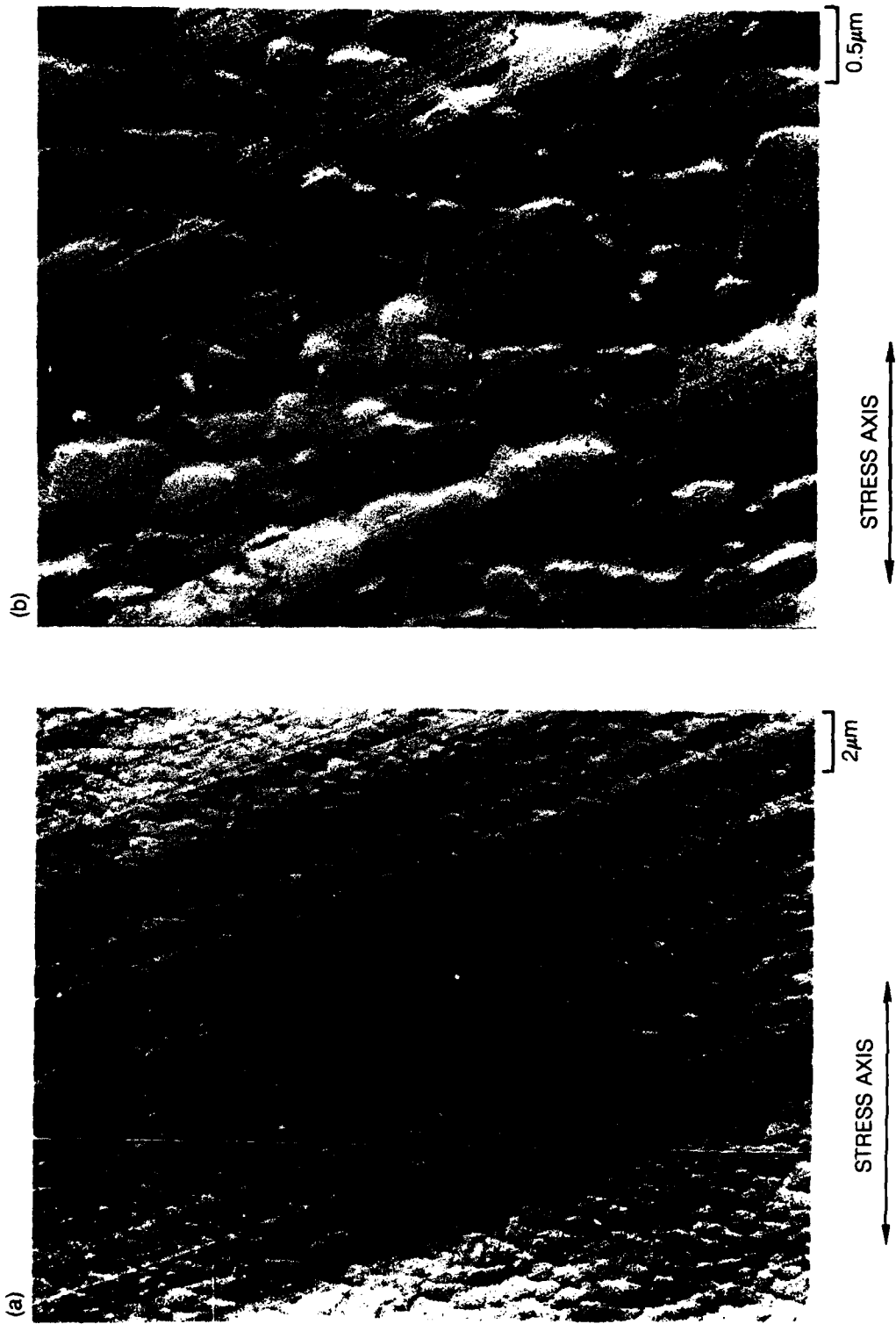
SURFACE REPLICA OF S/C 143 AFTER 1 CYCLE AT $\frac{\Delta\epsilon_T}{2} = 0.7\%$



SURFACE REPLICA OF S/C 143 AFTER 50 CYCLES AT $\frac{\Delta\epsilon_T}{2} = 0.7\%$ REVEALING SPREADING OF SLIP LINES DURING REPEATED REVERSED STRAINING



SURFACE REPLICA OF S/C 143 AFTER 200 CYCLES AT $\frac{\Delta\epsilon_T}{2} = 0.7\%$



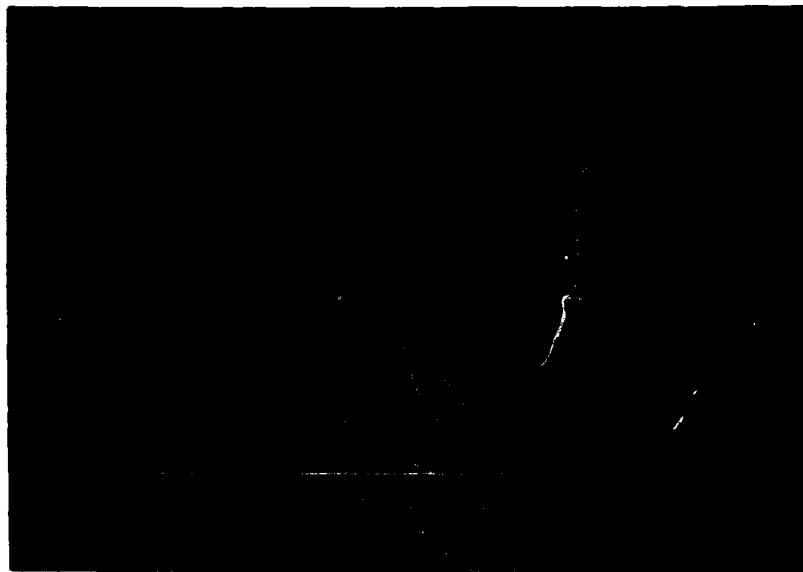
**FRACTURE SURFACE OF S/C 143 AFTER 1593 CYCLES AT $\frac{\Delta\epsilon_T}{2} = 0.7\%$
REVEALING SURFACE INITIATED FATIGUE FAILURE EMANATING
FROM PRONOUNCED SURFACE SLIP**

(a)



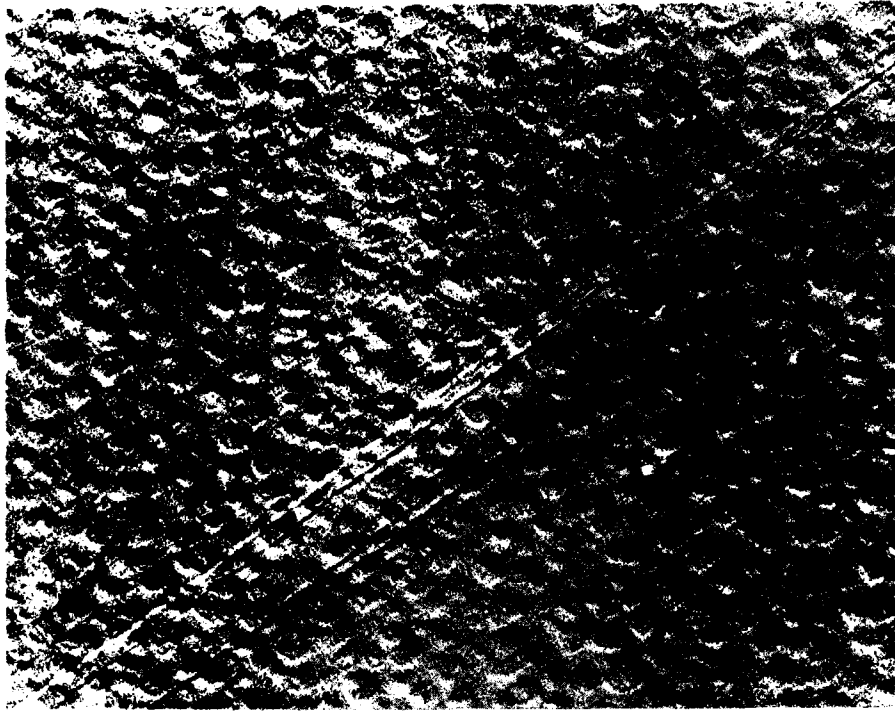
0.6 mm

(b)

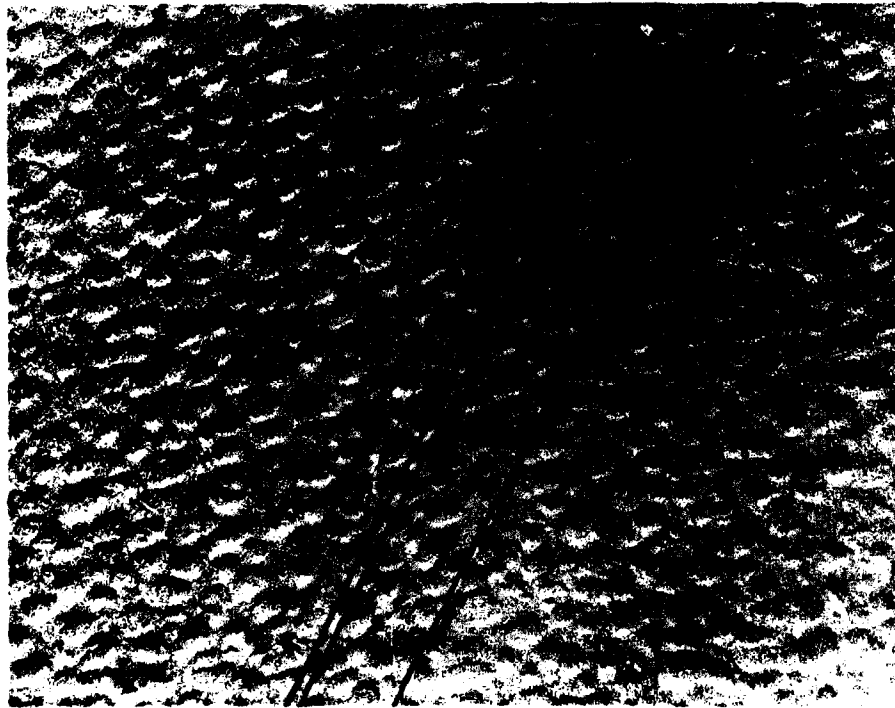


0.1 mm

SURFACE REPLICA OF U-700 AFTER 10 CYCLES AT $\Delta \epsilon_T = 0.14\%$



(b)



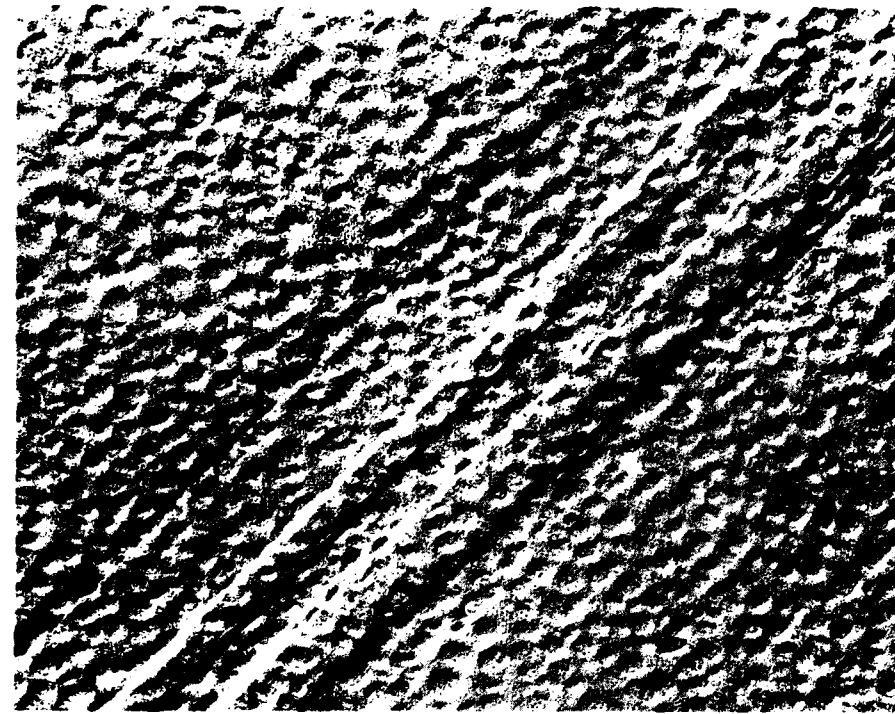
(a)

SURFACE REPLICA OF U-700 AFTER 50 CYCLES AT $\Delta \epsilon_T = 0.14\%$

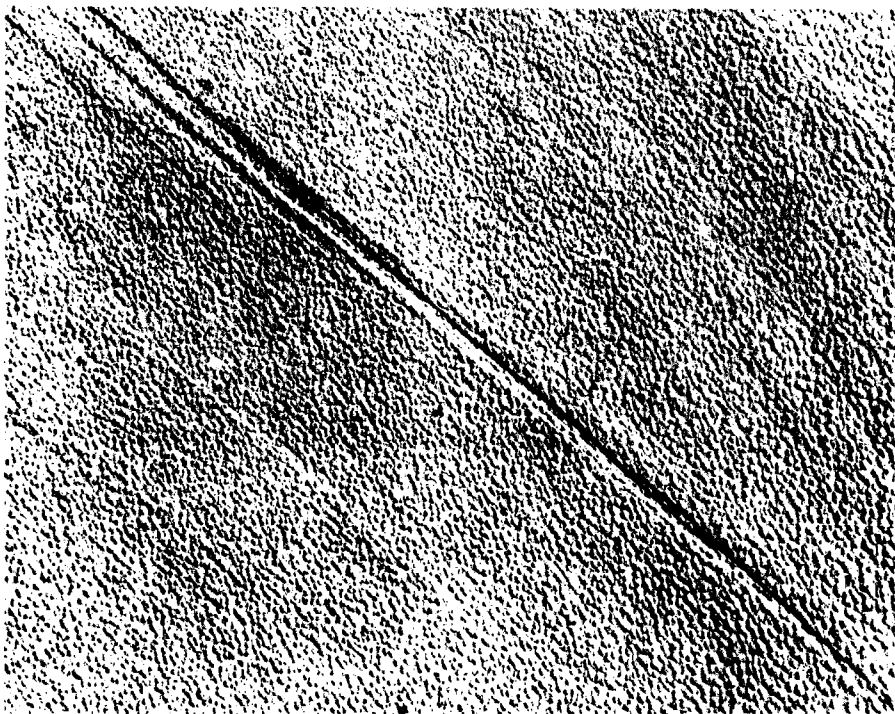


0.4 μ m

SURFACE REPLICA OF U-700 AFTER 100 CYCLES AT $\Delta \epsilon_T = 0.14\%$

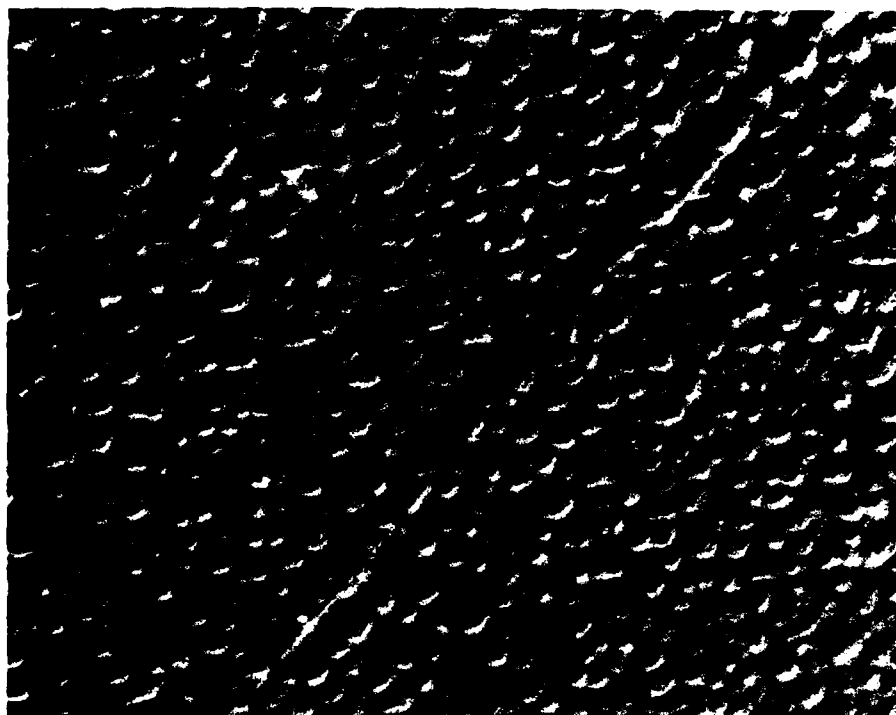


(b)

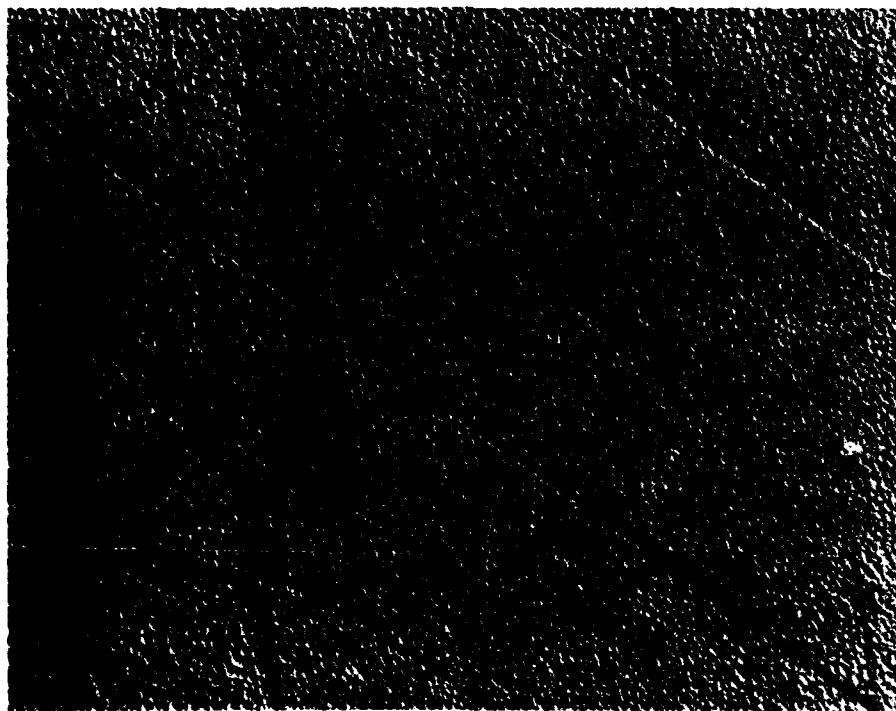


(a)

SURFACE REPLICA OF U-700 AFTER 305 CYCLES AT $\Delta \epsilon_T = 0.14\%$

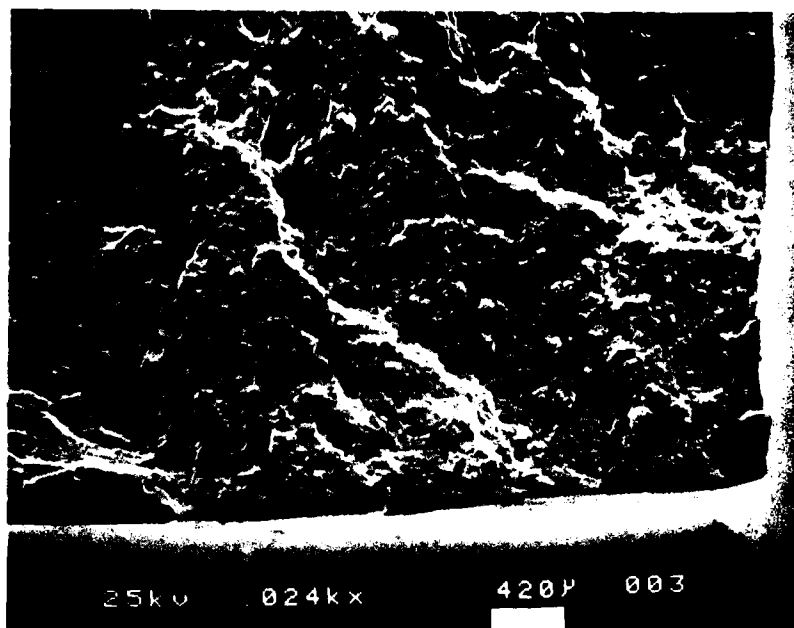


(b)



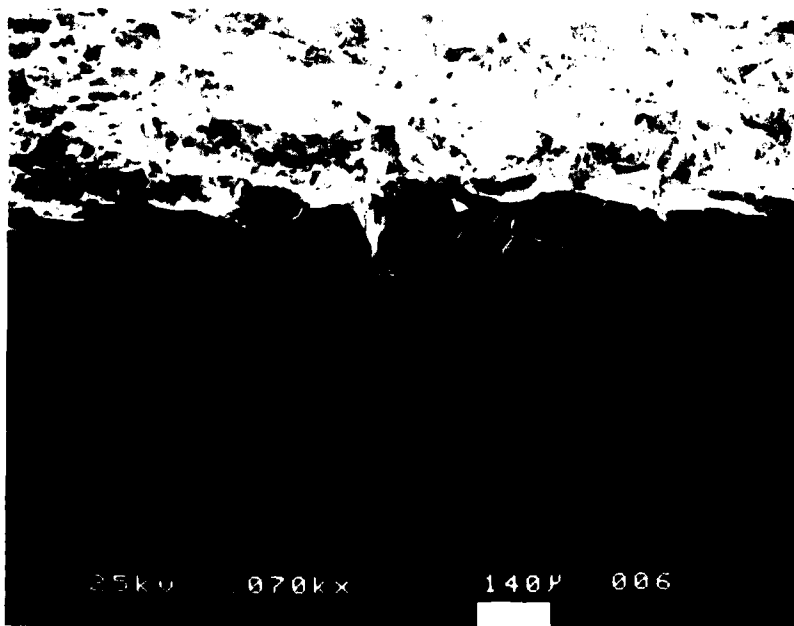
(a)

FATIGUE FAILURE INITIATION SITE IN SINGLE CRYSTAL U-700



(a)

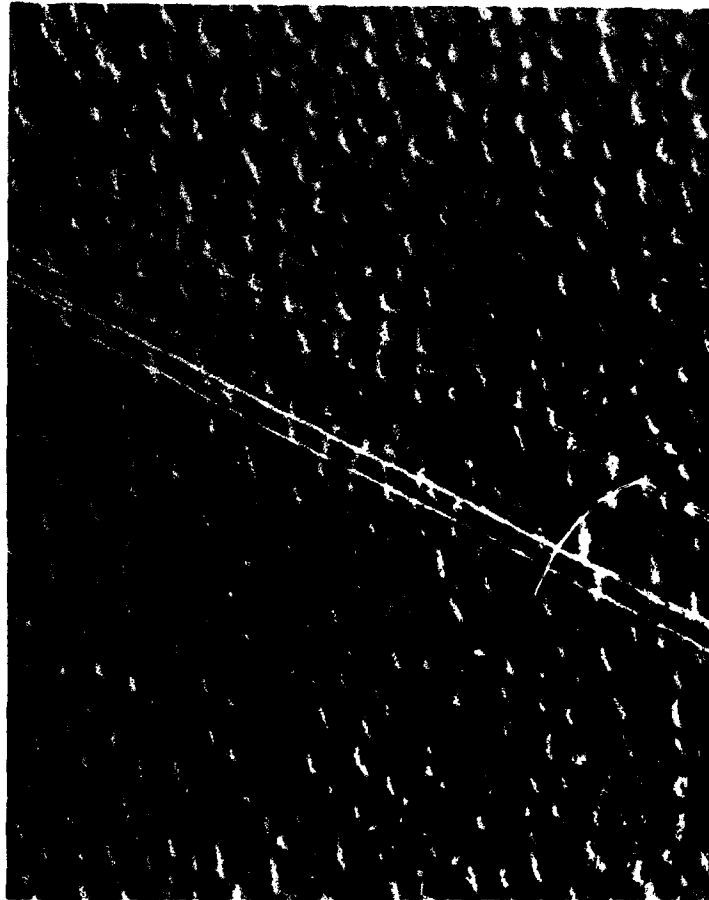
420µm



(b)

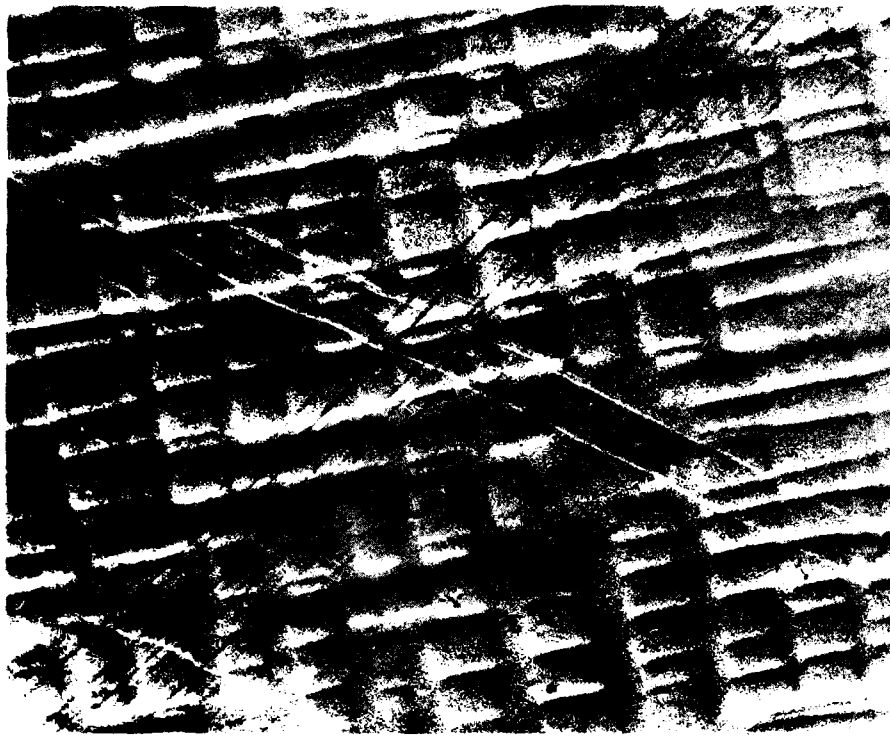
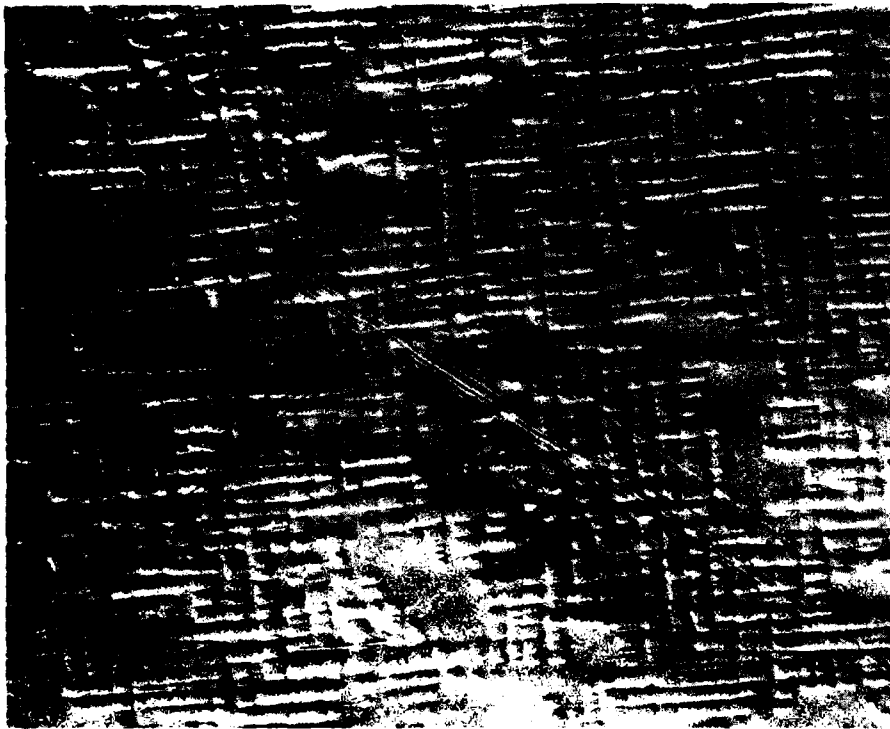
140µm

SURFACE REPLICA OF U-700 AFTER FATIGUE FAILURE

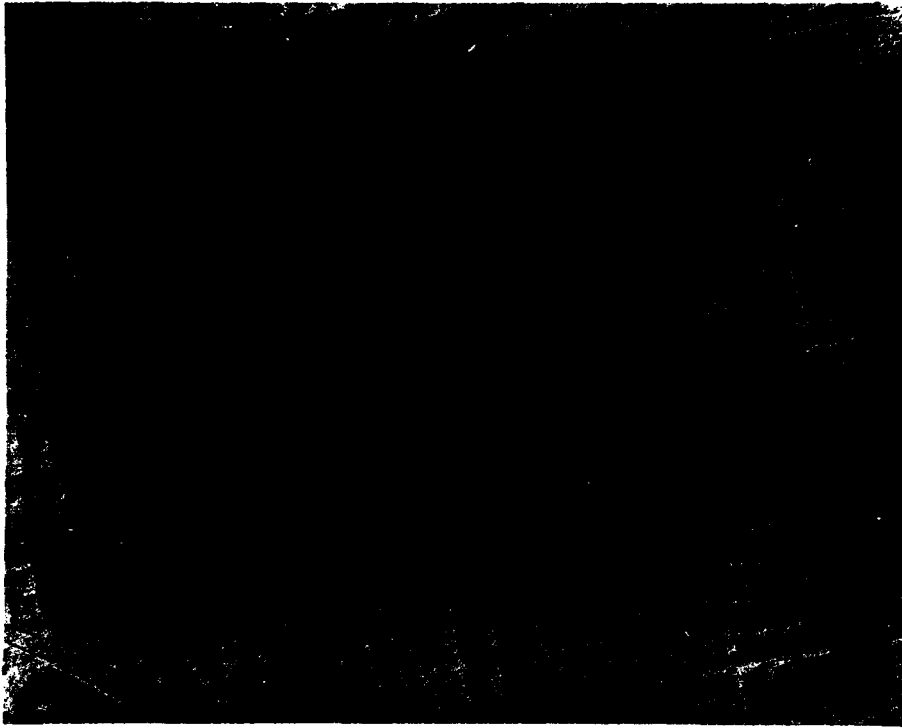


0.4 μ m

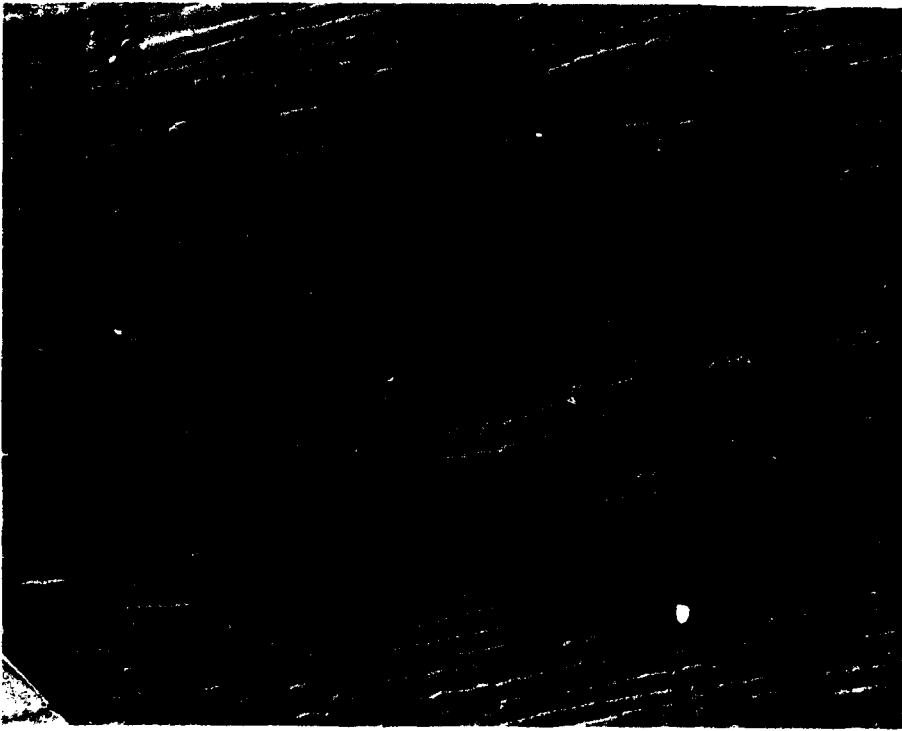
SURFACE REPLICA OF 143L AFTER 1 CYCLE AT $\Delta \epsilon_T = 0.14\%$



SURFACE REPLICA OF 143L AFTER 10 CYCLES AT $\Delta \epsilon_T = 0.14\%$



(b)



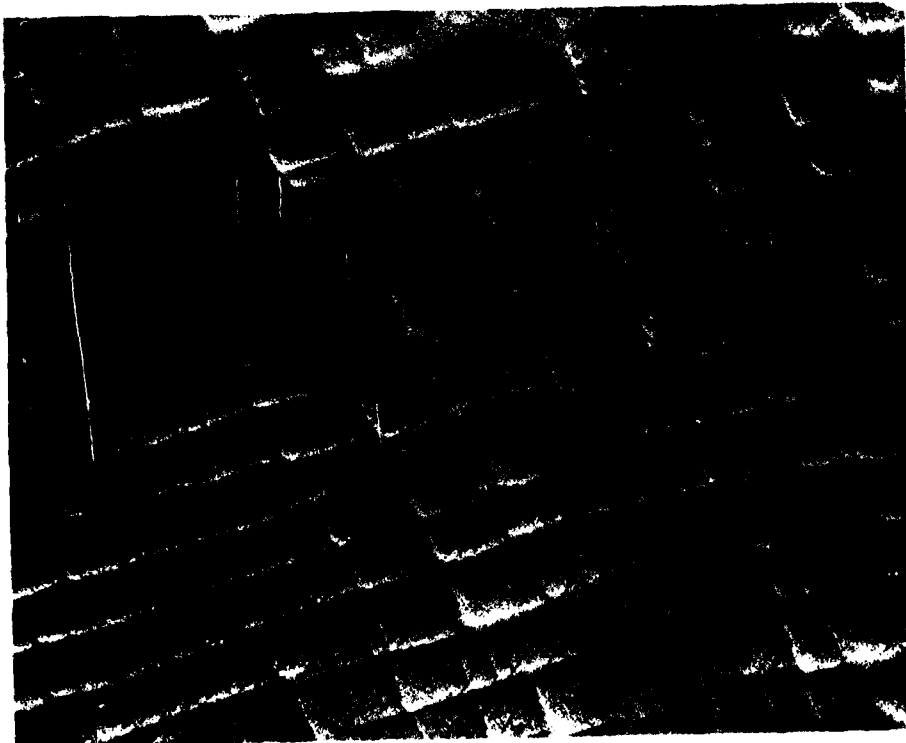
(a)

1.5μm

SURFACE REPLICA OF 143L AFTER CYCLING AT $\Delta \epsilon_T = 0.14\%$



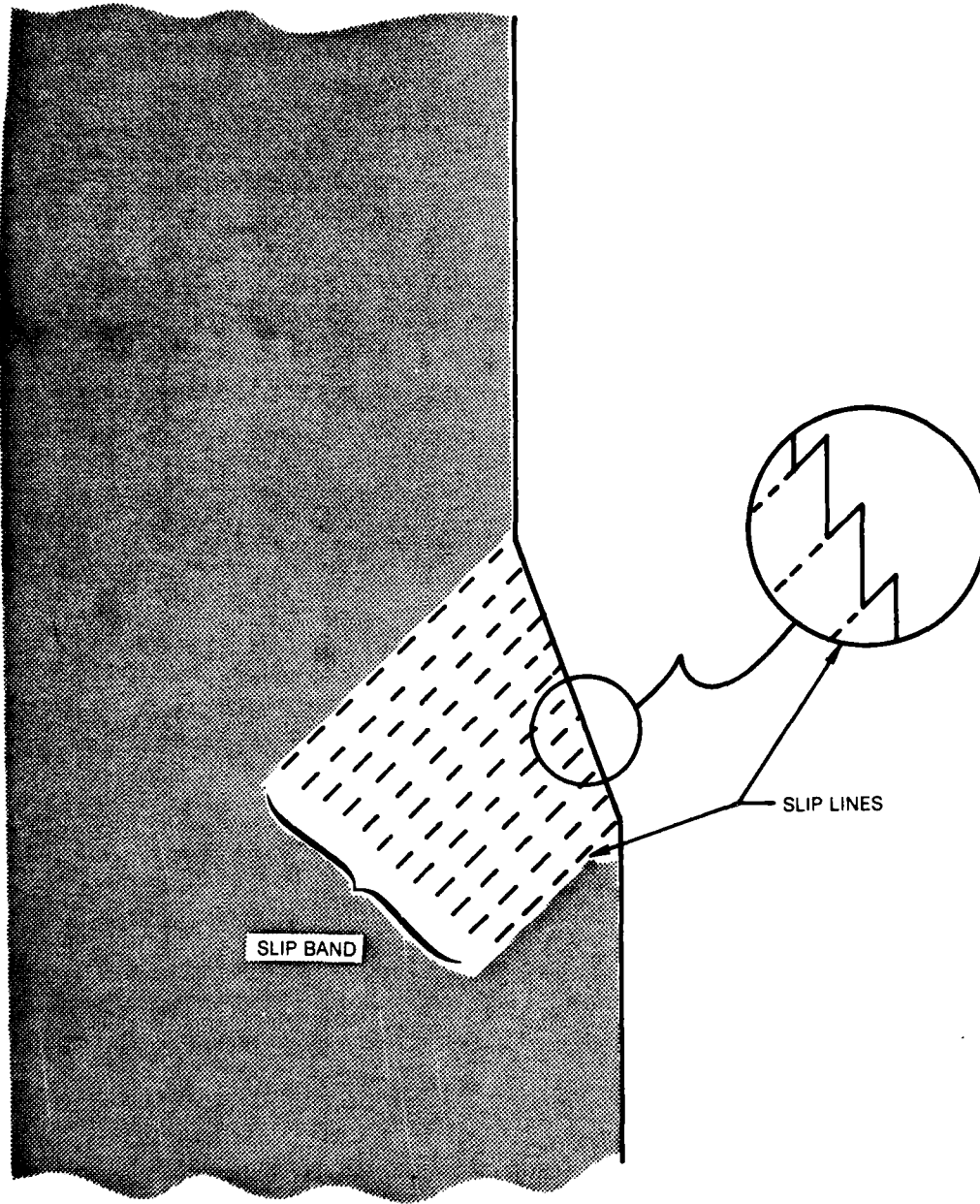
(b) 1000 CYCLES



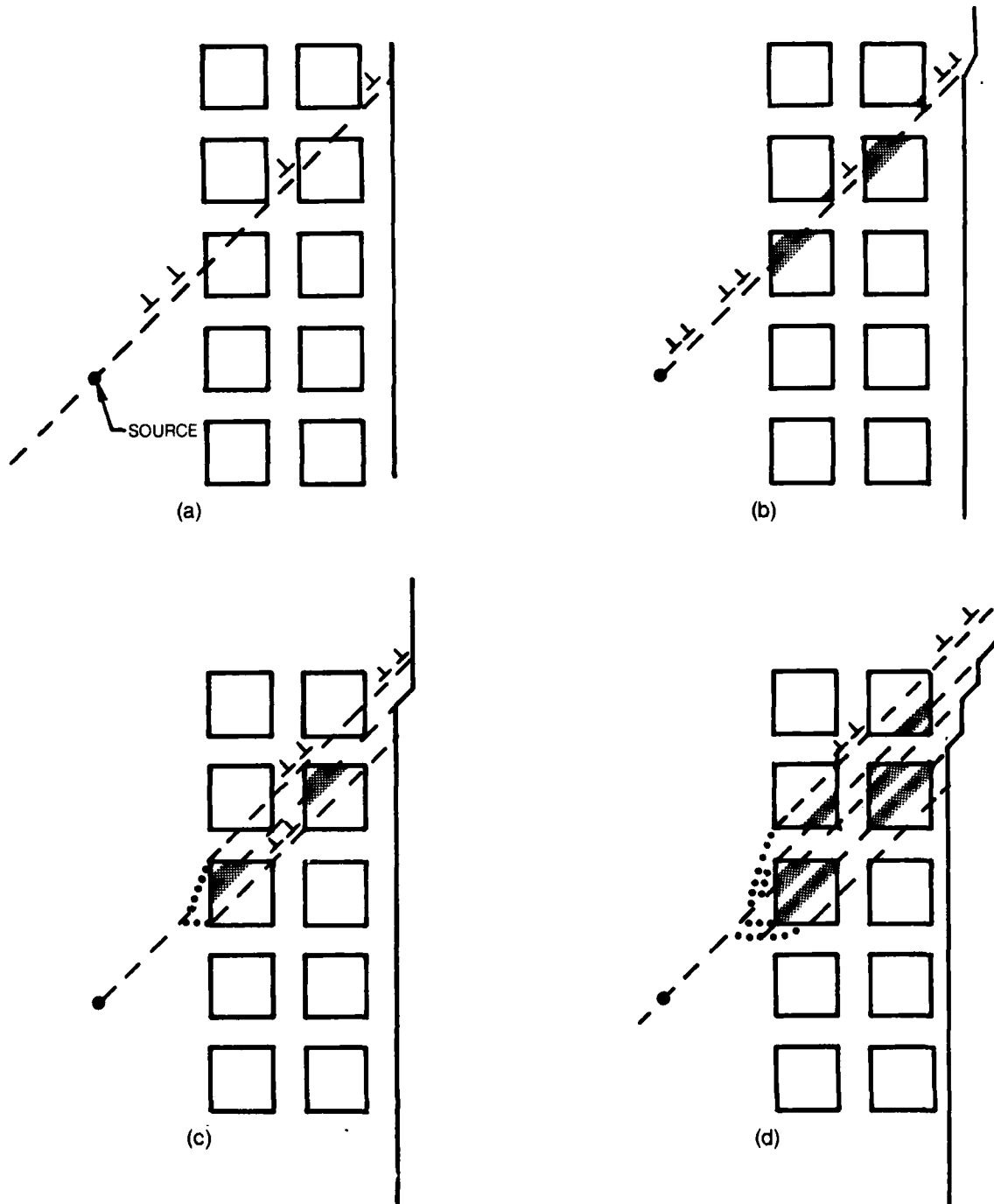
0.5 μ m

(a) 50 CYCLES

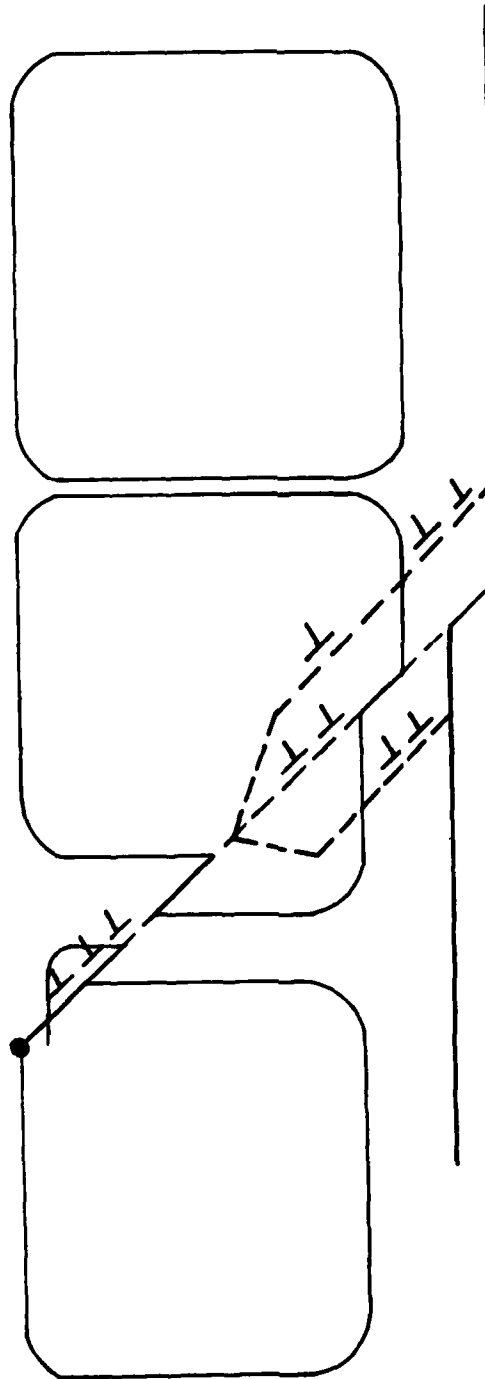
PROFILE OF SPECIMEN SURFACE SHOWING HOW SLIP LINES EMERGING AT SURFACE WILL PRODUCE MACROSCOPIC SLIP BANDS



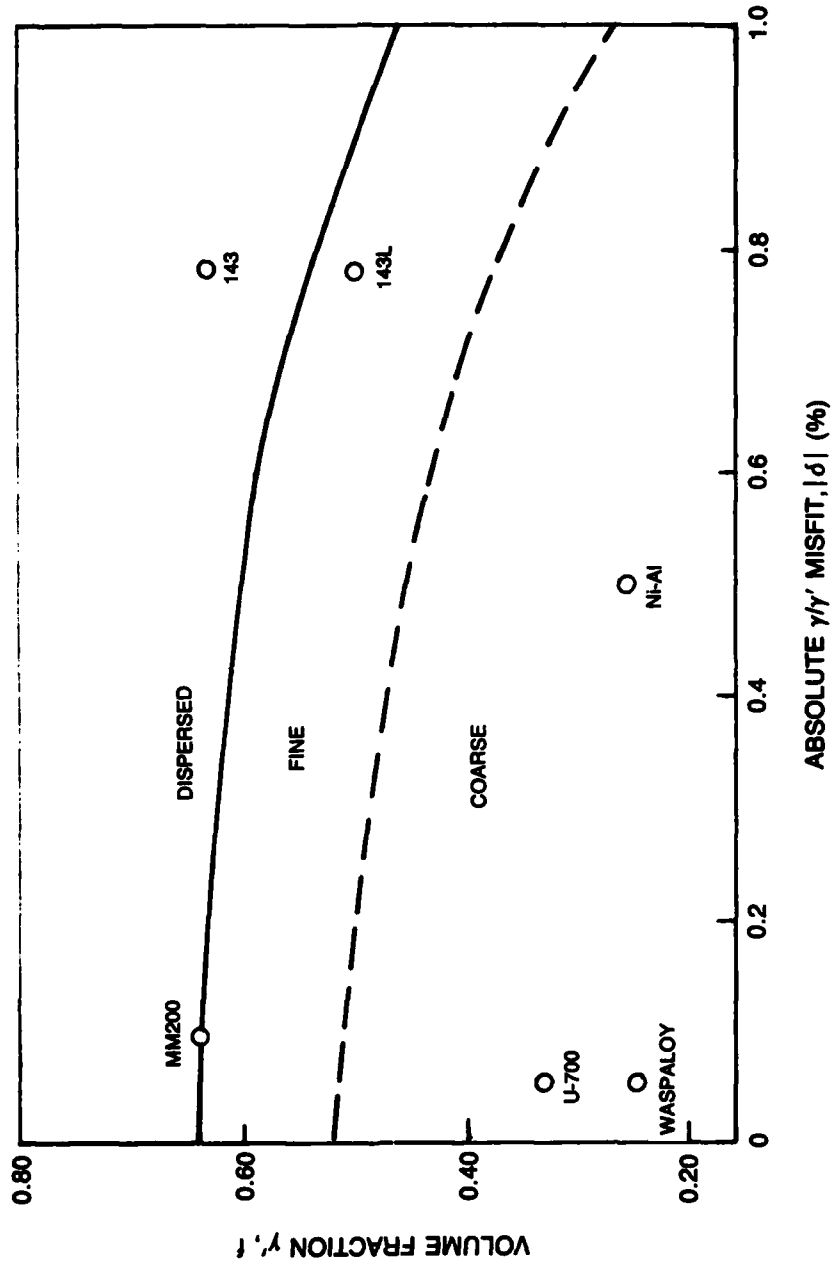
FORMATION OF A SLIP BAND, BY A SLIP PLANE HARDENING AND γ CROSS-SLIP MECHANISM, ACTIVATED BY A SINGLE DISLOCATION SOURCE



FORMATION OF A SLIP BAND, BY A SLIP PLANE HARDENING AND γ' CROSS SLIP MECHANISM, ACTIVATED BY A SINGLE SOURCE

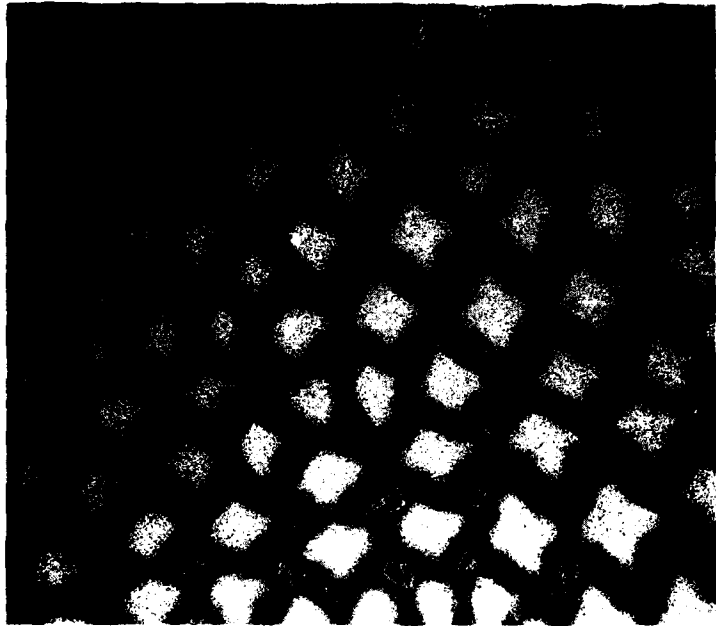


LOCAL PLASTIC STRAIN MAP FOR VARIOUS SUPERALLOYS



AS CAST MICROSTRUCTURE OF SINGLE CRYSTAL ALLOY 143 GROWN AT 1.27 cph

(a) TRANSVERSE



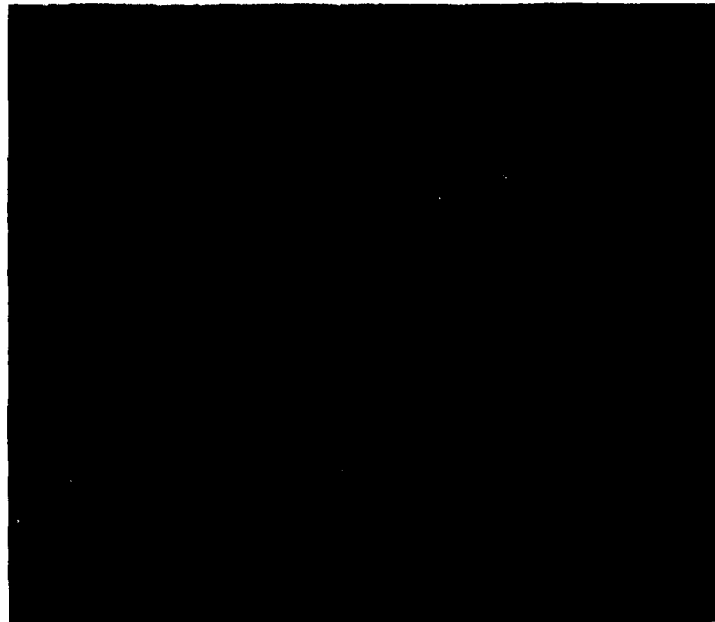
0.2 mm

(b) LONGITUDINAL



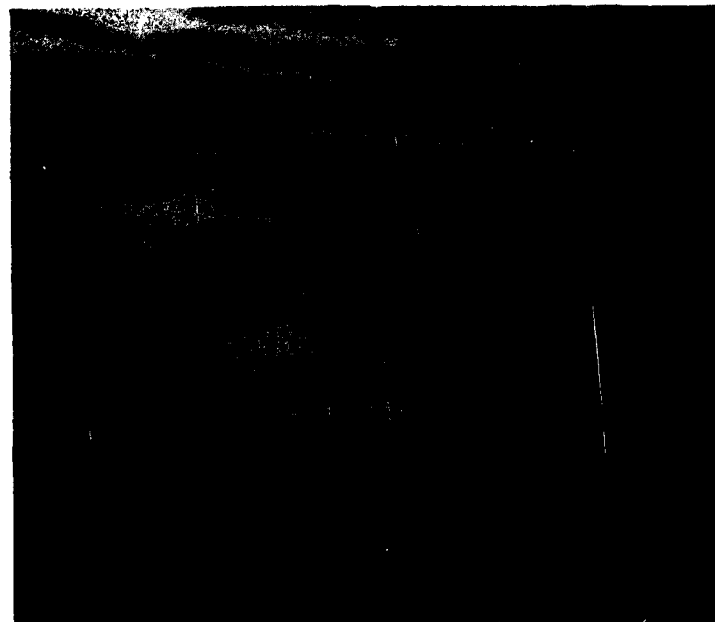
AS CAST MICROSTRUCTURE OF SINGLE CRYSTAL ALLOY 143 GROWN AT 2.54 cph

(a) TRANSVERSE



0.2 mm

(b) LONGITUDINAL



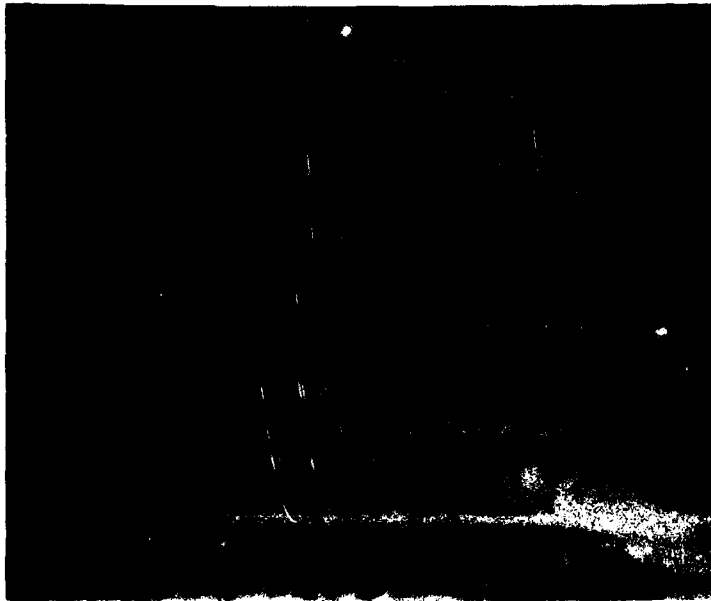
AS CAST MICROSTRUCTURE OF SINGLE CRYSTAL ALLOY 143 GROWN AT 12.7 cph

(a) TRANSVERSE



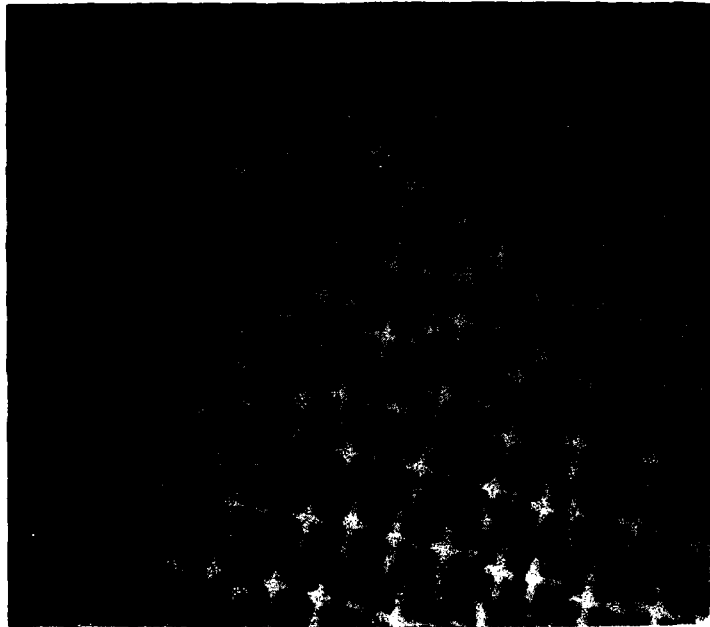
0.2 mm

(b) LONGITUDINAL

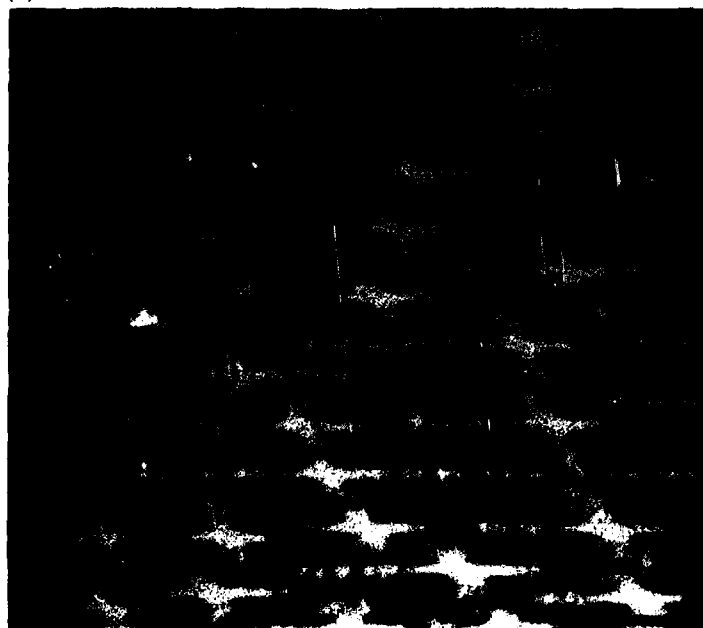


AS CAST MICROSTRUCTURE OF SINGLE CRYSTAL ALLOY 143 GROWN AT 25.4 cph

(a) TRANSVERSE

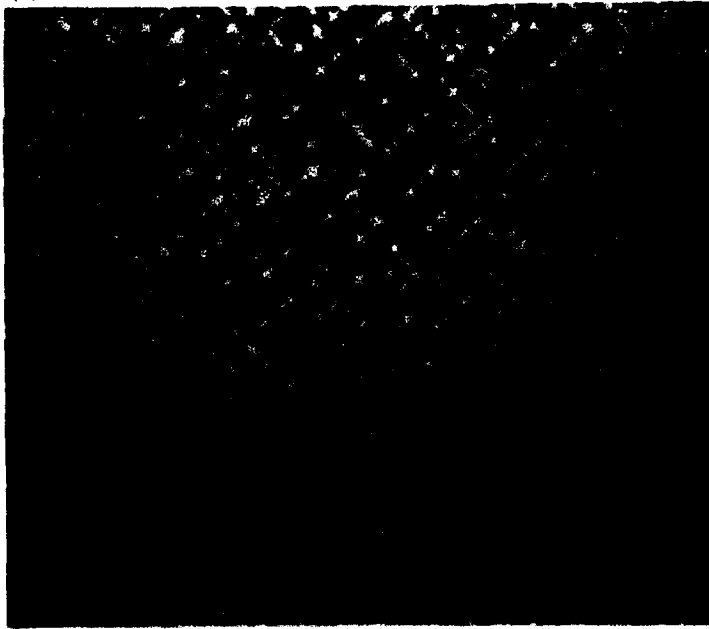


(b) LONGITUDINAL



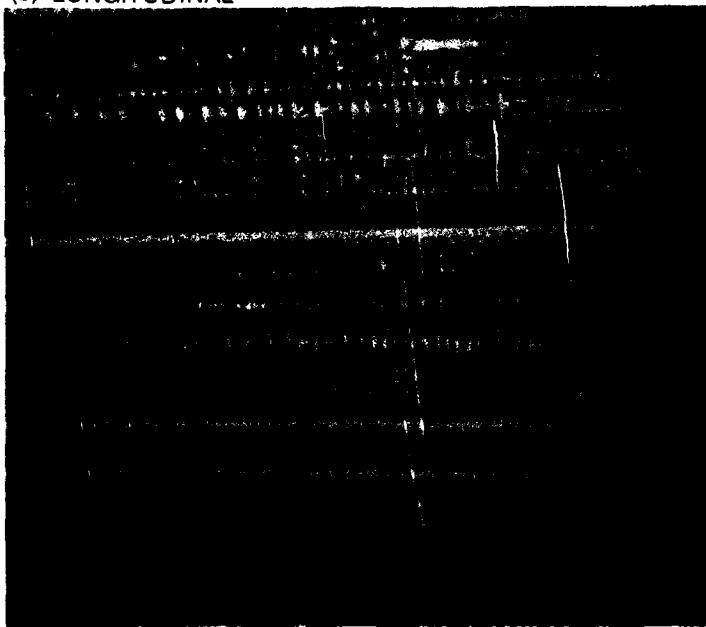
AS CAST MICROSTRUCTURE OF SINGLE CRYSTAL ALLOY 143 GROWN AT 127 cph

(a) TRANSVERSE



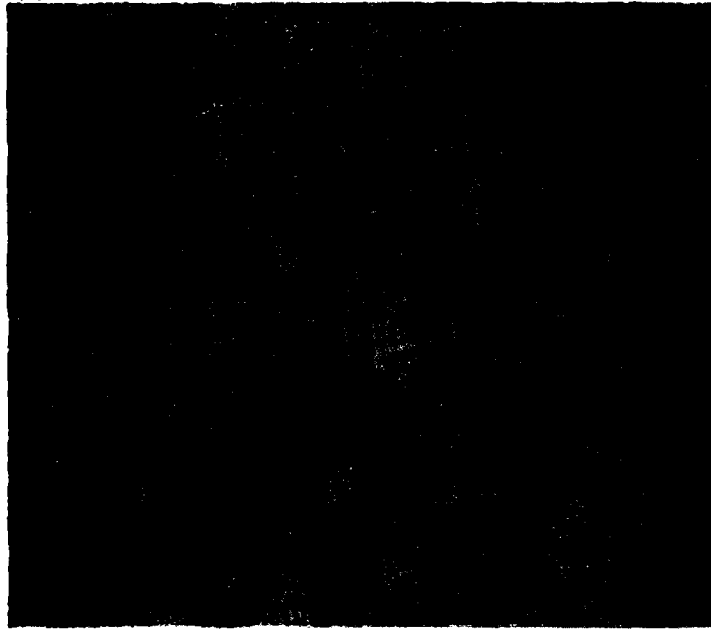
0.2 mm

(b) LONGITUDINAL



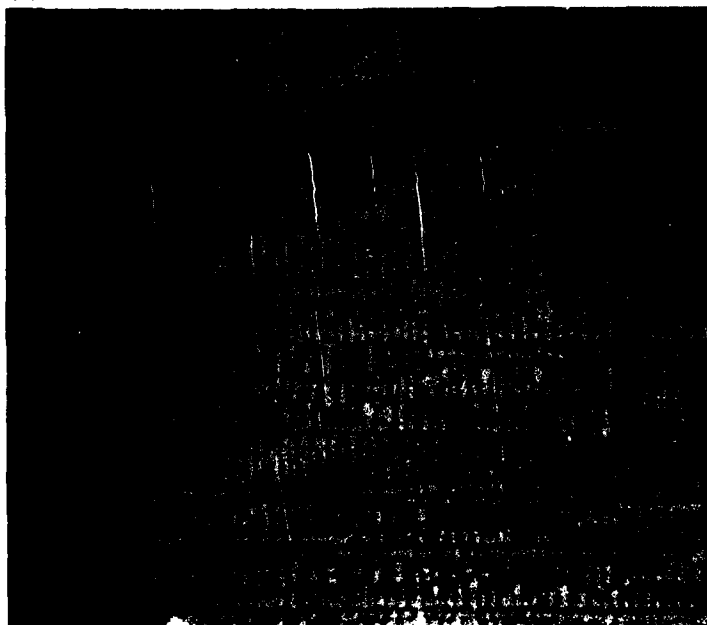
AS CAST MICROSTRUCTURE OF SINGLE CRYSTAL ALLOY 143 GROWN AT 254 cph

(a) TRANSVERSE



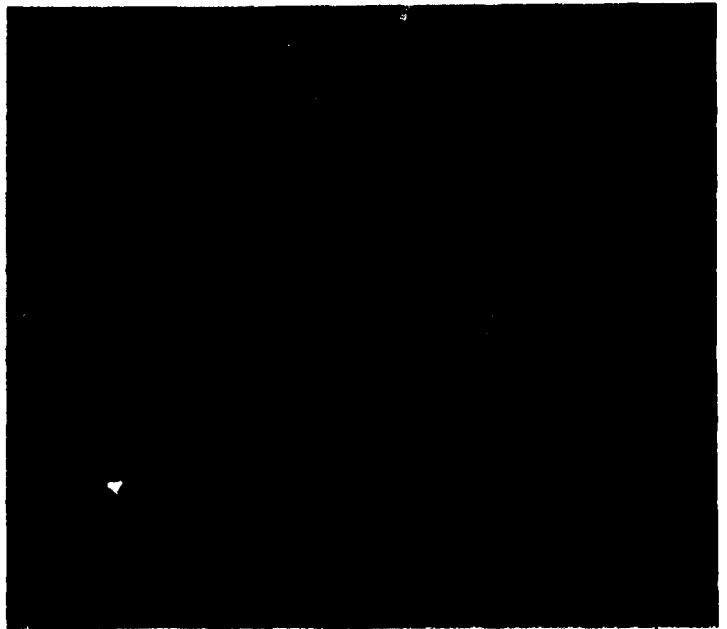
0.2 mm

(b) LONGITUDINAL



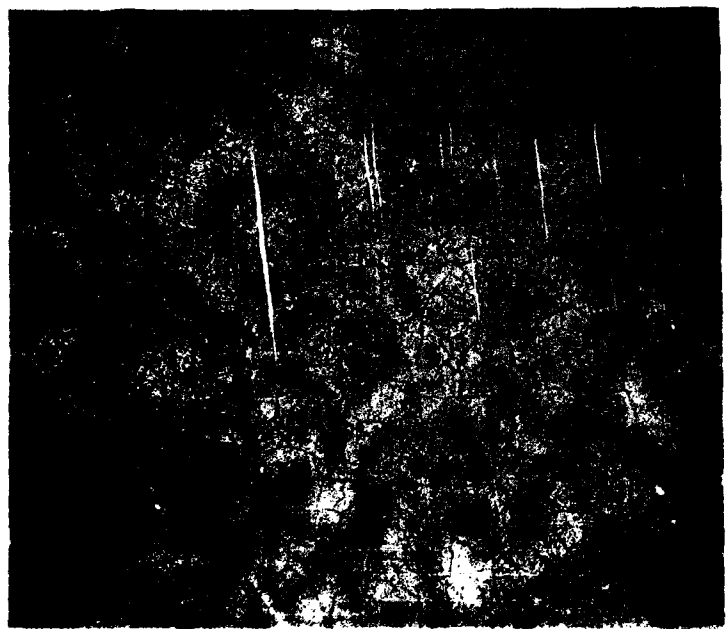
**TRANSVERSE MICROSTRUCTURE OF SINGLE CRYSTAL ALLOY 143
AFTER HOMOGENIZATION AT 1327°C FOR 16 hr**

(a) $R = 127$ cph

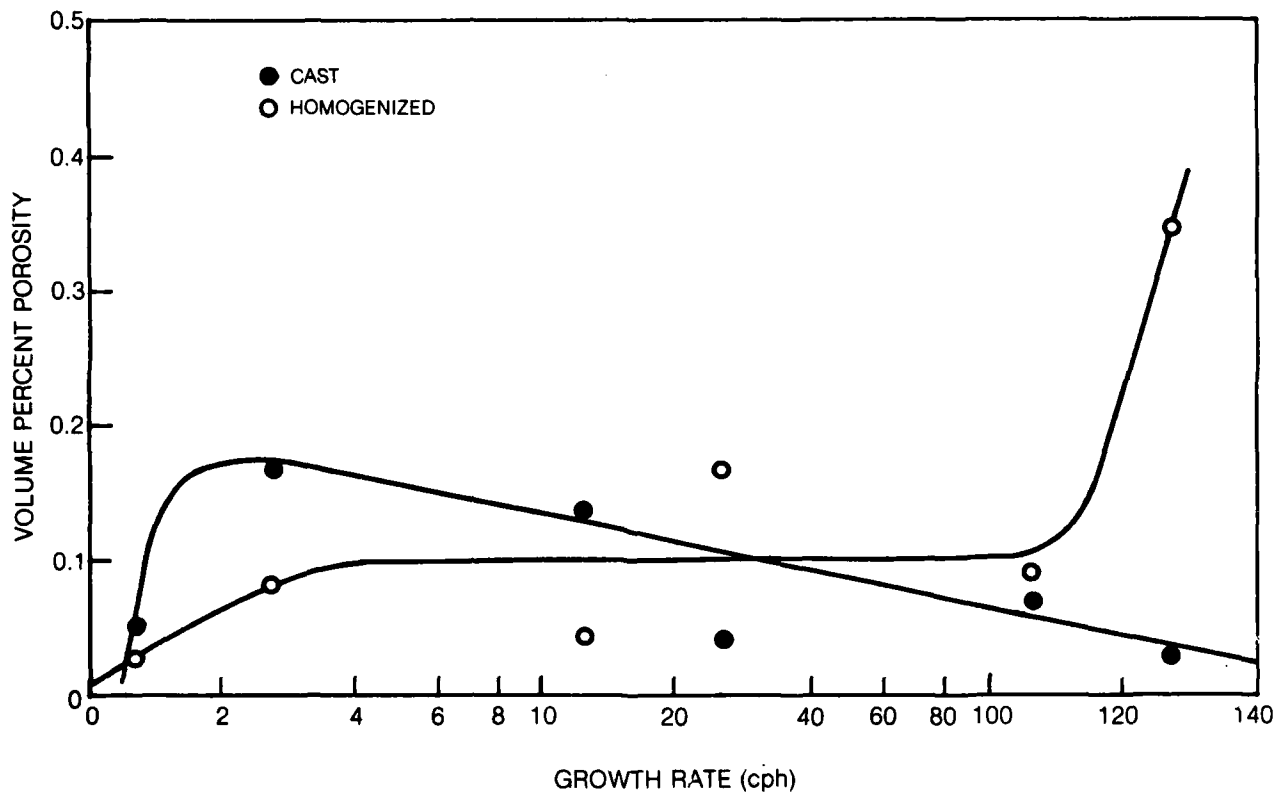


0.2 mm

(b) $R = 1.27$ cph



CHANGE IN VOLUME PER CENT POROSITY WITH GROWTH VELOCITY



AD-A173 187

PLASTIC STRAIN LOCALIZATION IN SUPERALLOY SINGLE
CRYSTALS(U) UNITED TECHNOLOGIES RESEARCH CENTER EAST
HARTFORD CT D L ANTON ET AL. 31 JUL 86

2/2

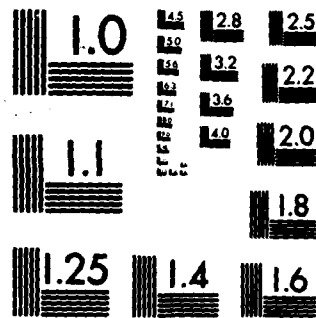
UNCLASSIFIED

UTRC/R86-916534-3 AFOSR-TR-86-0821

F/G 20/11

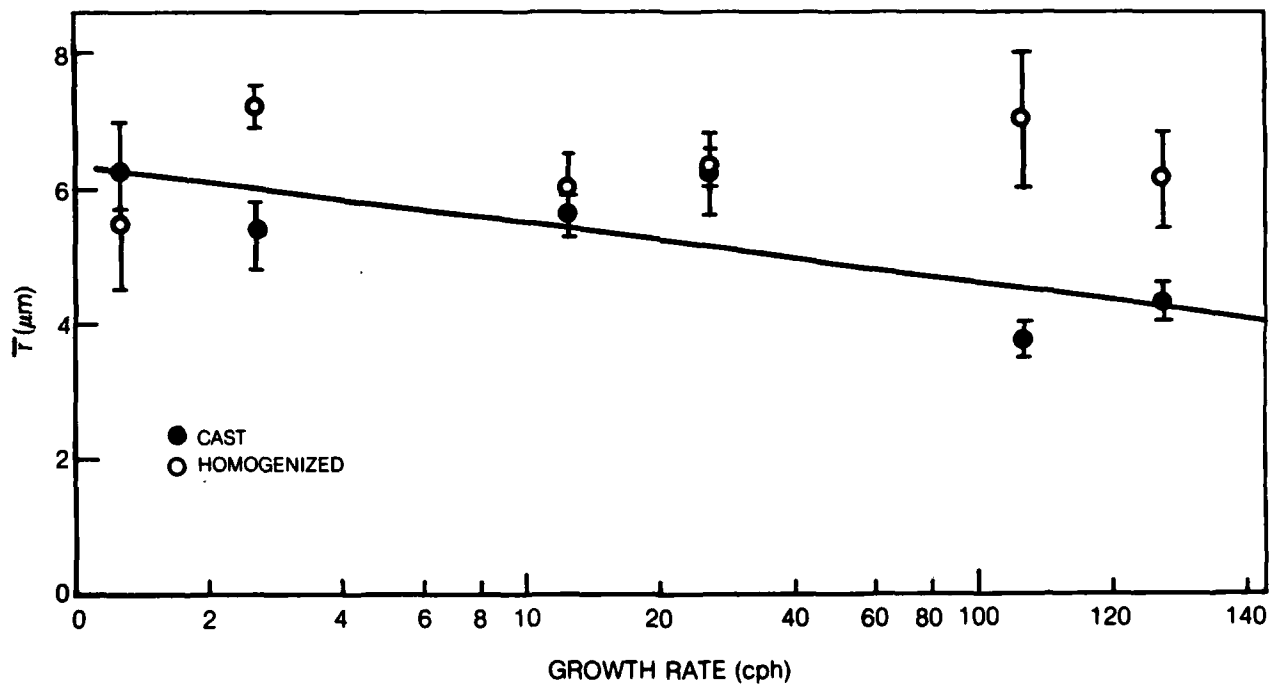
NL





MICROCOPY RESOLUTION TEST CHART
NATIONAL BUREAU OF STANDARDS-1963-A

CHANGE IN MEAN PORE DIAMETER WITH GROWTH VELOCITY



**FRACTURE SURFACE ILLUSTRATING POROSITY INITIATED
FATIGUE FAILURE**



┌
└ 285μm

**FRACTURE SURFACE ILLUSTRATING SURFACE SLIP INITIATED
FATIGUE FAILURES**



(a)

670µm



(b)

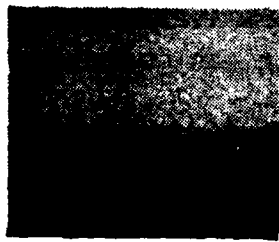
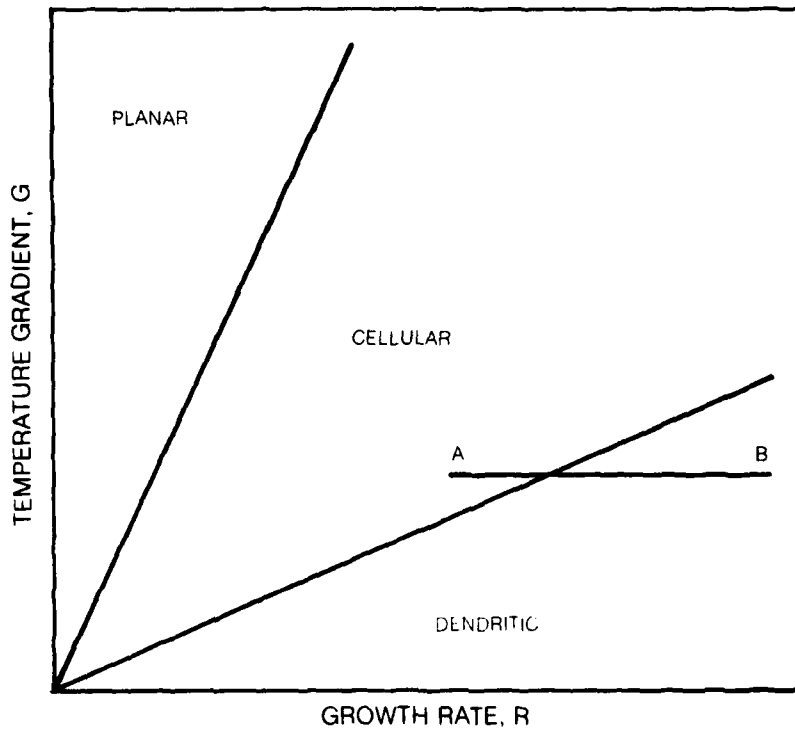
200µm

**FRACTURE SURFACE ILLUSTRATING SUB-GRAIN BOUNDARY INITIATED
FATIGUE FAILURES**

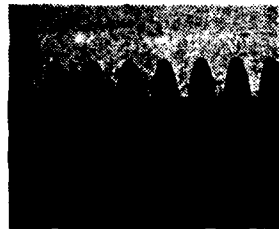


┌───┐
670μm

MODE OF SOLIDIFICATION AS A FUNCTION OF TEMPERATURE GRADIENT AND GROWTH RATE



PLANAR
INTERFACE

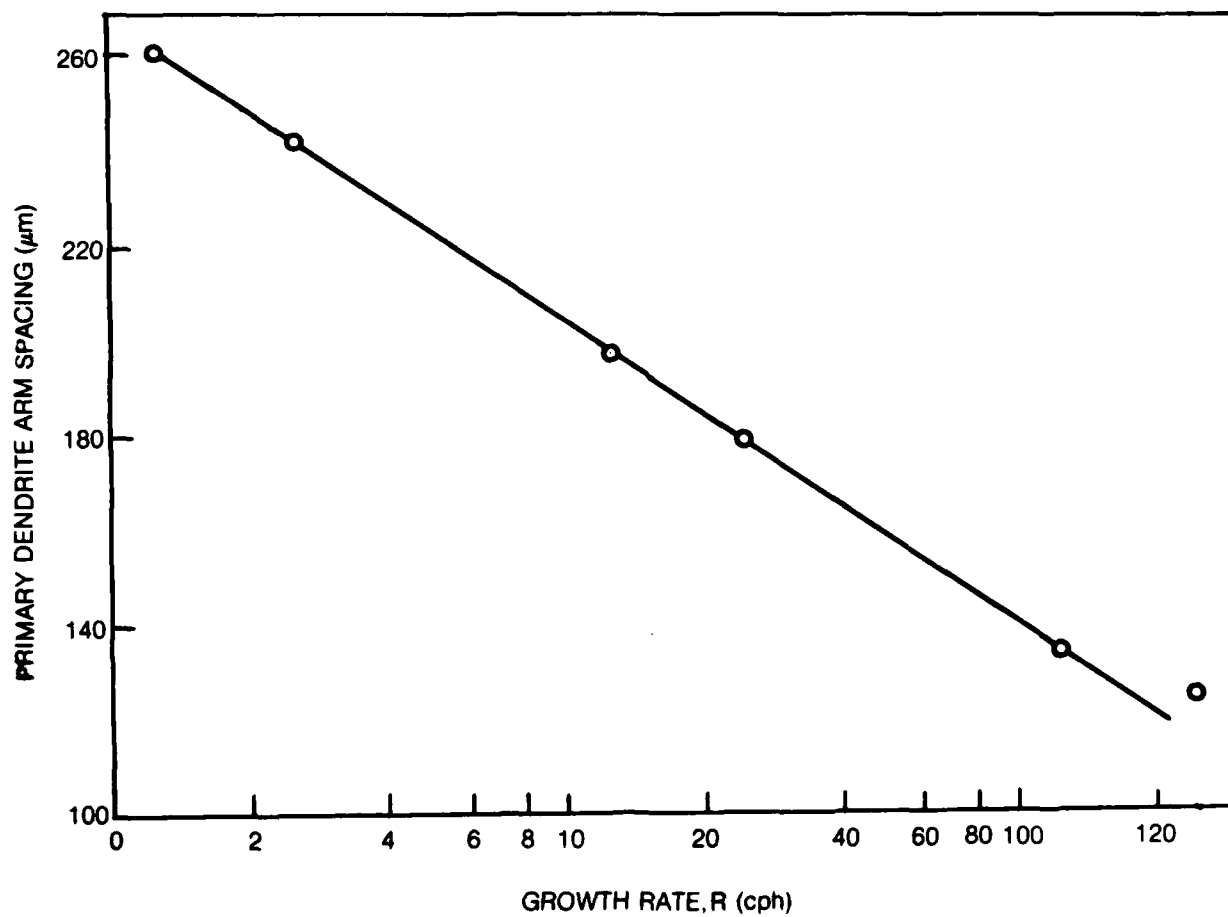


CELLULAR
INTERFACE



DENDRITIC
INTERFACE

THE VARIATION IN PRIMARY DENDRITE ARM SPACING WITH GROWTH RATE



END

12-86

DTIC